TÉCNICO LISBOA

Autonomous Orbit Control of LEO Satellites

Luís Miguel da Luz Bessa Ferreira

Thesis to obtain the Master of Science Degree in

Aerospace Engineering

Supervisors: Prof. Pedro Tiago Martins Batista

Dr. Sérgio Daniel Gonçalves Gante Brás

Examination Committee

Chairperson:	Prof. Afzal Suleman
Supervisor:	Dr. Sérgio Daniel Gonçalves Gante Brás
Member of the Committee:	Prof. João Pedro Castilho Pereira Santos Gomes

November 2021

Declaration

I declare that this document is an original work of my own authorship and that it fulfills all the requirements of the Code of Conduct and Good Practices of the Universidade de Lisboa.

Acknowledgments

I would like to start by thanking my thesis supervisors, Dr. Sérgio Brás, from the European Space Agency, and Prof. Pedro Batista, from Instituto Superior Técnico, for the guidance and support during all the phases of the development of this thesis. It would have been impossible to achieve this goal without their constant availability to clarify my questions, help in reviewing all the work, and motivation to not stop trying, even when the light at the end of the tunnel was too far to see.

I also would like to thank my mother, my father, and my sister for all the love and support, not only during the development of this thesis but throughout all my life. Thank you for the patience in the good and bad moments and for always being there for me and pushing me to follow my ambitions. Gostava de fazer um agradecimento especial, em português, às minhas avós por todo o carinho que me deram desde o meu primeiro dia. Gostava também de deixar uma lembrança aos meus avôs, os quais guardo num lugar especial dentro de mim. Obrigado!

To Joana, who unpredictably entered my life in the most needed moment. It would have been impossible without you by my side. Thank you for always comforting and encouraging me to keep on working and not giving up. Obrigado por estes meses e por todos os que sei que estão para vir!

Finally, I wish to leave a message to my future self to keep on trying even in the darkest moments. The process to achieve the greatest goals is always hard, but the reward makes it all worth it.
Le vent se lève! . . . il faut tenter de vivre!

Luís Miguel Ferreira

27/10/2021

Resumo

Os inúmeros benefícios da tecnologia espacial, bem como as suas aplicações, levaram a um aumento significativo do número de satélites lançados para o espaço ao longo dos anos. Estes satélites são projetados para realizar uma grande variedade de missões e, para tal, é necessário que os satélites sejam operados a partir de uma determinada órbita nominal. Contudo, os erros de injeção e as perturbações orbitais provocam um desvio da órbita do satélite relativamente à órbita nominal. Os desenvolvimentos recentes no desempenho computacional a bordo permitem realizar o processo de correção da órbita através de algoritmos de controlo orbital autónomo. Neste contexto, o objetivo desta tese consiste no desenvolvimento de um algoritmo autónomo para correção e manutenção da órbita de um satélite LEO (low Earth orbit na literatura Inglesa), utilizando soluções inovadoras de propulsão elétrica. Para alcançar o objetivo proposto, são exploradas duas diferentes metodologias de controlo: regulador linear quadrático e modelo de controlo preditivo. A solução de controlo final é baseada numa combinação destes dois métodos. O modelo de controlo preditivo é utilizado para corrigir erros iniciais elevados resultantes da injeção orbital, enquanto o regulador linear quadrático assegura a convergência final e a manutenção da órbita, compensando o efeito das perturbações orbitais. A missão TerraSAR-X foi selecionada para avaliar o desempenho do algoritmo desenvolvido. Os resultados obtidos nas simulações revelam que a estratégia de controlo proposta corrige eficazmente os erros de injeção em diferences elementos de Kepler. Para além disso, o algoritmo demonstra um bom desempenho na manutenção da órbita, corrigindo o efeito das perturbações orbitais de forma a satisfazer os requisitos da missão TerraSAR-X, mesmo quando se considera sensores e atuadores reais.

Palavras-chave: Controlo de órbita autónomo, satélite LEO, propulsão elétrica, modelo de controlo preditivo, regulador linear quadrático.

Abstract

Countless benefits and applications of space technology led to a significant rise in the number of satellites being launched into space over the years to perform a wide range of missions. To satisfy the mission objectives, the satellites need to be operated at a certain nominal orbit. However, orbital injection errors and environmental perturbations cause the orbit to deviate from the nominal one. Recent improvements in on-board computational performance allow transferring the orbit correction process to on-board autonomous orbit control (AOC) algorithms. On that matter, this thesis focuses on the development of an autonomous algorithm to perform orbit correction and maintenance of a LEO satellite using novel electric propulsion solutions. Two different control methodologies are explored to achieve the proposed objective: linear quadratic regulator (LQR) and model predictive control (MPC). A control solution based on a combination of these methods is proposed. The MPC is used to correct large initial errors that result from the orbital injection, whereas the LQR assures the final convergence and orbit maintenance by counteracting the effect of orbital perturbations. The TerraSAR-X mission was selected as a test-bed to evaluate the algorithm performance. Simulation results show that the proposed AOC strategy effectively corrects orbit injection errors in different Keplerian elements. Moreover, the AOC algorithm demonstrates good performance for orbit maintenance activities, correcting the effect of orbital perturbations and maintaining the orbital error within the TerraSAR-X mission requirements, even when considering realistic sensors and actuators.

Keywords: Autonomous orbit control, LEO satellite, electric propulsion, model predictive control, linear quadratic regulator.

Contents

List of Tables

List of Figures

List of Symbols

The next list describes the symbols that will be later used within the body of the document. Vectors and matrices are written in a boldface type. Matrices, however, are displayed in uppercase, while vectors are usually displayed in lowercase. Scalars are shown in a lightface type and can be either lowercase or uppercase. Roman and Greek symbols bear no special distinction.

Reference frames

$\mathcal{I} = \{\mathbf{i_1}, \mathbf{i_2}, \mathbf{i_3}\}$	True of Date reference frame.
$\mathcal{O} = \{\mathbf{o_1}, \mathbf{o_2}, \mathbf{o_3}\}$	Local Orbit reference frame.

Functions and Operators

$\boldsymbol{\nabla}(.)$	Gradient Operator.
$(.)^T$	Matrix transpose.
$(.)^{-1}$	Matrix inverse.
$\text{diag}(.)$	Diagonal matrix.
$[\mathbf{a} \times \mathbf{b}]$	Cross product between vector **a** and vector **b**.
$J(.)$	Cost function.
$\dot{\mathbf{a}}$	Time derivative of vector **a**.
$\ddot{\mathbf{a}}$	Second time derivative of vector **a**.
$\|\|(.)\|\|$	Norm operator.

Greek symbols

$\boldsymbol{\epsilon}$	Orbital error vector in Cartesian coordinates, expressed in the $\mathcal{I}$-frame.
θ	True anomaly.
$\dot{\boldsymbol{\theta}}$	Angular velocity of the Earth in the $\mathcal{I}$-frame.
μ	Standard gravitational parameter.
ρ	Local atmospheric density.
σ	Standard deviation.
Ω	Right ascension of the ascending node.
ω	Argument of periapsis.

Roman symbols

a	Semi-major axis.
$\mathbf{A}$	State matrix.
A_S	Cross-sectional area of the spacecraft exposed to the radiation.
$\mathbf{B}$	Input matrix.
c	Speed of light.
C_D	Drag coefficient.
C_R	Spacecraft reflectivity.
d_{Moon}	Distance between the spacecraft and the Moon.
d_{TBG_i}	Distance between the spacecraft and the celestial body.
D_{ap}	Number of days from when the Earth is at aphelion.
e	Orbit eccentricity.
$\mathbf{e_S}$	Unit vector from the spacecraft to the Sun.
E	Eccentric anomaly.
${}^{I}\mathbf{f}_c$	Control acceleration in the $\mathcal{I}$-frame .
${}^{O}\mathbf{f}_c$	Control acceleration in the $\mathcal{O}$-frame .
${}^{I}\mathbf{f}$	Perturbing acceleration in the $\mathcal{I}$-frame .
${}^{O}\mathbf{f}$	Resulting acceleration vector in the local orbit frame.
${}^{O}f_1, {}^{O}f_2, {}^{O}f_3$	Components of the acceleration vector in the local orbit frame.
${}^{I}\mathbf{f}_{aero}$	Atmospheric drag acceleration.
${}^{I}\mathbf{f}_{SRP}$	Solar radiation pressure acceleration.
${}^{I}\mathbf{f}_{TBG}$	Third-body attraction acceleration.
${}^{I}\mathbf{f}_{TBG_{Moon}}$	Lunar attraction acceleration.
${}^{I}\mathbf{f}_{TBG_{Sun}}$	Solar attraction acceleration.
${}^{I}\mathbf{f}_{\oplus}$	Gravity field perturbative acceleration.
g_0	Earth's standard gravitational acceleration at sea level.
G	Newton's universal gravitational constant.
h	Angular momentum.
$\bar{h}$	Altitude of the spacecraft above the surface of the Earth.
H	Density scale height.
i	Orbit inclination.
I_{sp}	Specific impulse.
I_S	Energy flux.
${}^{I}\mathbf{k}$	State representation of the spacecraft orbit using Keplerian elements.
$\mathbf{K}$	Kalman gain.
m	MPC control horizon.
M	Spacecraft total mass.
M_0	Mean anomaly.
n	Mean motion.

p	Semi-latus rectum.
p_h	MPC prediction horizon.
$\mathbf{r}$	Position of the spacecraft in the $\mathcal{I}$-frame.
$\mathbf{r}_{Moon}$	Position of the Moon in the $\mathcal{I}$-frame
$\mathbf{r}_r$	Reference position of the spacecraft in the $\mathcal{I}$-frame.
r_a	Apogee distance to the central body.
r_p	Perigee distance to the central body.
$\mathbf{R}^{\mathcal{I}}_{\mathcal{O}}$	Rotation matrix from $\mathcal{O}$-frame to the $\mathcal{I}$-frame.
$R_\oplus$	Mean equatorial Earth radius.
S/C	Spacecraft.
S	Spacecraft area projected along the direction of motion.
T	Orbital period.
T_t	Thrust produced by the spacecraft's thrusters.
T_r	Ground track repeatability error.
Ts	MPC sample time.
u	Argument of latitude.
U	Perturbing potential.
$U_\oplus$	Gravitational potential.
$\mathbf{v}$	Velocity of the spacecraft in the $\mathcal{I}$-frame.
$\mathbf{v}_r$	Reference velocity of the spacecraft in the $\mathcal{I}$-frame.
$\mathbf{v}_{rel}$	Relative velocity of the spacecraft with respect to the atmosphere in the $\mathcal{I}$-frame.
ΔV	Impulse per unit of spacecraft mass.
${}^I\mathbf{x}$	Contains the position and the velocity vectors of the satellite expressed in the $\mathcal{I}$-frame.
${}^I\mathbf{x}_k$	Contains the set of Keplerian elements of the satellite expressed in the $\mathcal{I}$-frame.

Subscripts

$\oplus$	Earth.
$aero$	Aerodynamic.
c	Control.
$\boldsymbol{\epsilon}$	Orbital error vector in Cartesian coordinates, expressed in the $\mathcal{I}$-frame.
LQR	Linear quadratic regulator.
r	Reference.
SRP	Solar radiation pressure.
TBG	Third-body gravitational attraction.

Superscripts

I	Expressed in the True of Date reference frame.
O	Expressed in the Local Orbit reference frame.

List of Acronyms

AOC	Autonomous orbit control.
GMAT	General Mission Analysis Tool.
GNSS	Global Navigation Satellite System.
GPS	Global Positioning System.
GVEs	Gauss' Variational Equations.
LEO	Low Earth orbit.
LOF	Local orbit reference frame.
LQR	Linear quadratic regulator.
LTAN	Local time of ascending node.
MPC	Model predictive controller.
OCK	Orbit control kit.
POD	Precise Orbit Determination.
SAR	Synthetic-aperture radar.
SRP	Solar radiation pressure.
TBG	Third-body gravitational attraction.
TDRSS	Tracking Data Relay Satellite System.
TLE	Two-line element.
ToD	True of date reference frame.

Chapter 1

Introduction

1.1 Context

Over 2500 active satellites are orbiting the Earth, of which more than 1900 are in low Earth orbit (LEO) [1]. The significant increase in the number of satellites being sent into space is strictly related to the role played by space technologies in various development sectors, such as agriculture, security, climate, rural development, public management, telecommunications, urban development, and disaster management [2]. Over the next decade, it is expected that the number of orbiting satellites will significantly increase due to the growing dependence of the industry on satellite-based solutions [3].

The rapid increase in the number of active satellites motivates the need for enhanced autonomous strategies to reduce the workload of ground-based teams. This thesis, for instance, focuses on novel on-board orbit control algorithms that allow to perform orbital correction maneuvers without ground-segment intervention.

1.2 Motivation

LEO satellites are used to fulfil a variety of missions, from Earth and space observation to communications and military applications. Most of the man-made objects orbiting the Earth are in LEO as they require less energy for orbit placement and, therefore, less associated cost. To satisfy the mission objectives, the orbit of these satellites is designed to fulfil certain requirements. However, launch injection errors and the effect of orbit perturbations (e.g. gravity influence of other celestial bodies, non-uniform Earth gravity field, and the atmospheric drag) cause the orbit to deviate from the one originally projected. For instance, long-duration missions at low altitudes will face an orbital decay with time due to the effect of the atmospheric drag. This is normally not acceptable and, therefore, orbital maneuvers are performed to correct the orbital deviation. Usually, this process is completely managed by the ground-segment in a time-consuming and inefficient process that requires visibility of the satellite to download data to compute the correction maneuvers and, subsequently, upload the maneuver plan to the satellite [4].

The increase of on-board computational resources created a new opportunity for the implementation

of on-board algorithms to control the spacecraft orbit automatically without ground intervention. In this context, on-board autonomous orbit control (AOC) arises as the answer to meet mission requirements and reduce the workload of operational teams. In fact, autonomous orbit control systems achieve better results in a more efficient and economical way since the correction maneuvers can be computed in real time and with a significant reduction of ground operations [5]. Simple control strategies, such as the linear quadratic regulator (LQR), have been used to develop autonomous orbit control algorithms (see [5]). The recent improvement in computational performance enables the use of more powerful control strategies, namely the model predictive control (MPC), to explore new AOC algorithms and enhance control performance. Moreover, the emergence of electric propulsion solutions, which allows for more precise and efficient orbit control, promotes increased on-board autonomy and the development of new AOC strategies.

1.3 Literature Review

Autonomous orbit control is a new topic that, in comparison to autonomous attitude control, has only been recently paid attention to. One of the first groups to work on autonomous orbit control was Microcosm that tested their orbit control kit (OCK) on-board the UoSAT-12 satellite, launched in April 1999 [6]. The success of that mission validated the use of autonomous orbit control to correct deviations from the reference orbit and maintain a satellite's long-term orbit parameters. Following that, new experiments and missions emerged to validate different strategies for autonomous orbit control implementation.

CNES DEMETER satellite, launched in 2004, demonstrated the feasibility of in-track autonomous control as a routine feature [5]. In 2011, the PRISMA mission validated the autonomous orbit keeping algorithm to maintain the longitude of the ascending node of the MANGO spacecraft, within a certain tolerance [7]. Regarding the PRISMA mission, Sergio De Florio and Simone D'Amico developed an orbit control strategy based on the relative motion of two satellites. They approached the orbit control problem as a formation fly between a real satellite, affected by the orbital perturbations, and a virtual satellite that fulfils the orbit requirements imposed by the mission. A standard LQR controller was implemented to compute the control actions and perform orbit corrections to maintain the position error between the real and the virtual satellite below 250 m (root-mean-square). PRISMA mission was used as a test-bed to validate the control algorithms [5].

The strategy proposed in [4] uses a proportional-derivative controller to compute in-track and cross-track corrections based on the relative position of the satellite's orbit parameters, provided by the navigation system, and the reference orbit. To ensure an optimal maneuver, control actions are determined taking into account AOC maneuver slots available along the orbit. Simulations demonstrated that an in-track error window of ± 2000 m and a cross-track error window of ± 1000 m was achieved.

A more powerful, but more computationally demanding, control strategy was proposed by Tavakoli and Assadian. They investigated the use of MPC for autonomous orbit control of LEO satellites by applying a similar strategy as Florio and D'Amico. The orbit control problem was converted into a relative orbit control problem in which an MPC controller computes the finite horizon optimal firing times of the satellite

thrusters, in order to drive the satellite to the reference orbit, not affected by undesirable perturbations. It was proven that the MPC method can compensate for the disturbances that affect a satellite orbit while minimising fuel consumption and, therefore, increasing the satellite lifetime when compared to an LQR based strategy [6].

The majority of autonomous orbit control solutions use chemical propulsion to perform corrective maneuvers. The strategy proposed in [8], for instance, uses tangential impulses produced by chemical thrusters to correct the effect of the atmospheric drag on the orbit of the LightSAR. The LightSAR mission requires the orbit to be maintained within a 125 m radius tube centered on a reference orbit over the lifetime of the mission. The strategy developed to meet the orbit maintenance requirement maximises the length of time between thruster firings using tangential impulses. The simulations demonstrated that the orbit maintenance strategy was able to successfully maintain the LightSAR orbit within the requirements for an entire repeat cycle of 8 days using a total of 5 maneuvers.

The emergence of electric propulsion systems, such as Hall and ion thrusters, enabled new control strategies. Mirko Leomanni, Andrea Garulli, and Antonio Giannitrapani developed a solution, for a spacecraft driven by electric propulsion, to maintain a repeat ground track orbit [9]. The control approach proposed uses a hysteresis controller that provides a pulse-width modulated command to the thruster. Simulation results showed that the resulting control scheme was able to acquire and maintain consistently in-orbit the desired repeat ground track pattern, in a fully autonomous manner.

Based on the literature review, it is concluded that autonomous orbit control strategies are mainly based on the assumption that the orbit injection process is precise. In fact, the control solutions previously mentioned are directed to counteract the effect of orbital perturbations and maintain the satellite in its desired orbit, neglecting initial errors originated by the orbital injection. However, navigation errors of the launcher and thrust inaccuracies originate an error between the targeted orbit and the actual injection orbit. The continuous improvements in computational performance and control techniques, together with the recent advance in the electric propulsion topic, promote the emergence of novel autonomous orbit control strategies to overcome this problem.

1.4 Objectives

The objective of this thesis is the development of an algorithm to perform autonomous orbit control of a LEO satellite using electric propulsion that can cope with a wide range of initial error conditions. This algorithm computes the required control actions to correct initial orbit injection errors and maintain the orbital parameters of the satellite close to the reference, counteracting the effect of orbital perturbations. Two different control solutions are used to achieve this objective: LQR and MPC. Due to its demanding orbit control requirements, the TerraSAR-X mission was selected as a test-bed to evaluate the algorithm performance. One of the main requirements of this mission is the maintenance of a ground track repeatability of $\pm\ 500$ m per revisit orbit [10].

The goals for this master thesis are summarised as follows:

- Identify and model the dynamics of the orbit of a satellite;

- Investigate and study the different types of propulsion systems;
- Analyse and compare the LQR and the MPC performance for the AOC problem;
- Design of a control algorithm to perform AOC activities;
- Demonstrate that the designed AOC algorithm can meet the TerraSAR-X mission requirements, particularly the maintenance of the ground track repeatability.

1.5 Contributions

From the literature review, it is noticeable a clear lack of AOC strategies that account for large initial errors due to the orbital injection process. In this thesis, a solution to overcome these injection errors and drive the initial orbit to the desired one is proposed. This solution is based on an advanced control strategy, namely the MPC. Despite the increased computational effort, this more powerful control technique offers enhanced capabilities to the control system (e.g. the possibility of introducing actuator saturation and of using directly a nonlinear system model), which are not present in the solutions usually proposed in the literature. The control strategy was developed based on the use of electric thrusters as the actuators to correct the satellite orbit, which is an emergent solution in the field of autonomous orbit correction and maintenance.

1.6 Thesis Outline

This thesis is organised as follows:

- **Chapter 2** includes a summary of the background concepts required for the research presented in this document, such as the definition of the reference frames used throughout the work, the orbital motion models and the perturbation forces that affect this motion, the different control strategies implemented, and a discussion between the available types of sensors and actuators.
- **Chapter 3** introduces the problem of the autonomous orbit control applied to a particular mission – TerraSAR-X. A description of the mission and its requirements is provided in this chapter.
- **Chapter 4** provides an overview of the proposed control strategy and the corresponding implementation. The process used in the design of the LQR and the MPC controllers is also described.
- **Chapter 5** provides a description of the simulation setup including the parameters used in the MATLAB script.
- **Chapter 6** presents and analyses the simulation results for different types of orbital errors.
- **Chapter 7** summarises and discusses the results obtained in this thesis and presents some suggestions for future work.

Chapter 2

Theoretical Background

This chapter provides a summary of the background concepts required for the work presented in this document. Section 2.1 introduces the two reference frames considered in this research. Following, Section 2.2 provides a description of the orbital motion laws expressed in Cartesian coordinates and Keplerian elements. The most relevant perturbation forces that affect a spacecraft motion are presented in Section 2.3. It then follows, in Section 2.4, with the validation of the orbital motion laws and the perturbative forces models introduced in the previous sections. Lastly, Section 2.5 introduces the control methodologies considered in this thesis and Section 2.6 provides a description of the relevant sensors and actuators to perform orbital control.

2.1 Reference Frames Definition

There are several reference frames relevant to describe the orbit of a spacecraft about the Earth. To provide a better understanding of the reference frames used in this thesis, this section introduces two distinct frames: the True of Date (ToD) coordinate frame and the Local Orbit (LOF) coordinate frame (see [11], [12], and [13]).

2.1.1 True of Date Frame

The equations that describe the orbital motion are more straightforward when described in an inertial reference frame ratter than when described in an accelerated or rotating frame, which simplifies the design of automatic orbit controllers. The ToD coordinate frame (see Fig. 2.1) has its origin coincident with the center of mass of the Earth and is approximately an inertial reference frame, even though its origin suffers an acceleration caused by other celestial bodies, mainly the Sun. This acceleration can be neglected for the accuracy required for the applications considered in this thesis given its small magnitude when compared with the magnitude of the gravitational acceleration caused by the Earth.

Throughout this thesis, the ToD frame is represented by the basis $\mathcal{I} = \{\mathbf{i_1}, \mathbf{i_2}, \mathbf{i_3}\}$, with the following orientation:

- The $\mathbf{i_1}$ axis points from the center of mass of the Earth to the vernal equinox, at the current epoch, which is the intersection between the ecliptic plane and the equatorial plane, where the Sun crosses the equator from the Southern Hemisphere to the Northern Hemisphere;
- The $\mathbf{i_3}$ axis is along the axis of the Earth's rotation at the current epoch and pointing towards the North Pole;
- Finally, the $\mathbf{i_2}$ axis completes the right-handed orthogonal reference frame.

Due to the precession of the Earth's rotation axis, the direction of the coordinate system axes varies with time. Therefore, the direction of these axes is defined relative to the current epoch of the analysis. This is advantageous when compared to inertial frames defined at a specific date, such as the J2000 inertial frame, defined on 1 January 2000, since these frames do not consider the constant precession of the Earth's rotational axis during the analysis period. This way, the Earth gravity field perturbations presented in Section 2.3.4, which are Earth-fixed reference frame, can be directly used in the orbit dynamics expressed in the ToD coordinate frame.

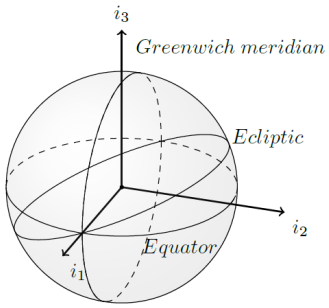

Figure 2.1: ToD coordinate frame [12].

2.1.2 Local Orbit Frame

The Local Orbit frame is defined with respect to the orbit of the spacecraft and is represented by the basis $\mathcal{O} = \{\mathbf{o_1}, \mathbf{o_2}, \mathbf{o_3}\}$. The $\mathbf{o_3}$ axis points from the center of the Earth to the spacecraft, whereas the $\mathbf{o_2}$ axis points in the direction of the spacecraft's orbital angular velocity. The $\mathbf{o_1}$ axis completes the right-handed orthogonal reference frame, pointing in the direction of the motion for a circular orbit. This coordinate frame has its origin in the spacecraft's center of mass. An illustration of the Local Orbit frame is shown in Fig. 2.2.

The representation of these vectors in the ToD frame is given by

$$\mathbf{o_3} = \frac{\mathbf{r}}{\|\mathbf{r}\|},$$

$$\mathbf{o_2} = \frac{(\mathbf{r} \times \mathbf{v})}{\|\mathbf{r} \times \mathbf{v}\|},$$

$$\mathbf{o_1} = \mathbf{o_2} \times \mathbf{o_3},$$

where **r** and **v** are, respectively, the position and the velocity of the spacecraft expressed in the ToD coordinate frame, $\mathcal{I}$. The rotation matrix $\mathbf{R}_{\mathcal{O}}^{\mathcal{I}}$ that maps vectors expressed in the $\mathcal{O}$-frame to the $\mathcal{I}$-frame is given by

$$\mathbf{R}_{\mathcal{O}}^{\mathcal{I}} = [\mathbf{o_1} \quad \mathbf{o_2} \quad \mathbf{o_3}].$$

To fully map a point expressed in the $\mathcal{O}$-frame to the $\mathcal{I}$-frame, it is also necessary to translate the origin of the reference frame.

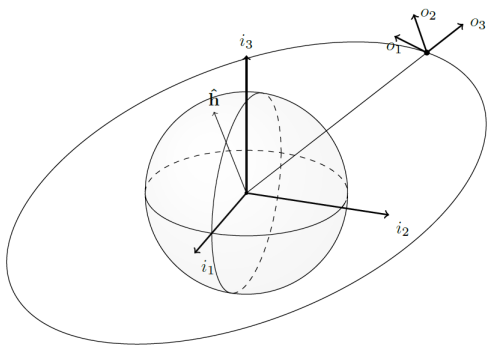

Figure 2.2: Local Orbit coordinate frame [12].

2.2 Orbital Motion

Orbital motion is considered as the movement of a body about a planet, due to the gravity effect. This thesis introduces two different orbital motion models to describe the motion of a satellite in its orbit about the Earth.

2.2.1 Cartesian Coordinates Representation

If the motion of a satellite is described relative to the ToD frame and perturbations are taken into account, then the equation of motion can be written in the form (see [14])

$$\ddot{\mathbf{r}} + \frac{\mu}{||\mathbf{r}||^3}\mathbf{r} = -\nabla U(\mathbf{r}, \mathbf{v}) + {}^{I}\mathbf{f}(\mathbf{r}, \mathbf{v}), \tag{2.1}$$

where $U(\mathbf{r}, \mathbf{v})$ stands for the perturbing or disturbing potential and describes all perturbing forces that can be expressed by a potential function, ${}^{I}\mathbf{f}(\mathbf{r}, \mathbf{v})$ accounts for all perturbing accelerations that cannot be written as the gradient of a scalar function of the satellite's coordinates, and μ is the standard gravitational parameter. The term $\frac{\mu}{||\mathbf{r}||^3}\mathbf{r}$ is related to the central body acceleration, assuming that the mass of the primary body is much greater than the mass of the spacecraft, so the center of mass of the system is

coincident with that of the primary body. From (2.1), the set of first-order differential equations of the position and the velocity of a satellite, expressed in the ToD reference frame, is given by

$$\begin{cases} \dot{\mathbf{r}} & = \mathbf{v} \\ \dot{\mathbf{v}} & = -\frac{\mu}{||\mathbf{r}||^3}\mathbf{r} - \boldsymbol{\nabla} U(\mathbf{r}, \mathbf{v}) + {}^{I}\mathbf{f}(\mathbf{r}, \mathbf{v}) \end{cases}. \tag{2.2}$$

The set of equations (2.2) is a simple model to compute the position and the velocity of a spacecraft by means of numerical integration and when one pretends to work with Cartesian coordinates.

2.2.2 Keplerian Elements Representation

Keplerian elements are parameters used to represent the spacecraft position in its orbit about the Earth, which provide immediate insight about the orientation and geometry of the orbit. In fact, the Cartesian position and velocity of the spacecraft may be useful for some computational applications but provide little insight into important aspects of the orbital motion [5], [15].

It is then necessary to choose a set of orbital elements for the absolute state representation of the spacecraft orbit, given by (see [16])

$${}^{I}\mathbf{k} = \begin{pmatrix} a \\ e \\ i \\ \Omega \\ \omega \\ M_0 \end{pmatrix},$$

where

- a (semi-major axis) is related to the size of the orbit and it is given by the sum of the perigee and apogee distances (r_p and r_a respectively) divided by two, $a = \frac{r_a + r_p}{2}$;
- e (eccentricity) defines the shape of the ellipse, describing how much it is elongated compared to a circle, and it is given by $e = \frac{r_a - r_p}{r_a + r_p}$;
- i (inclination) stands for the angle between the orbital plane and the equator plane;
- Ω (longitude of the ascending node) is the angle between the $\mathbf{i_1}$ axis and the intersection of the orbit with the equator plane, where the spacecraft crosses from the Southern Hemisphere to the Northern Hemisphere;
- ω (argument of perigee) is the angle formed between the intersection of the orbit with the equator plane, where the spacecraft crosses from the Southern Hemisphere to the Northern Hemisphere, and the perigee, on the orbital plane;

- M_0 (mean anomaly) defines the position of the spacecraft in its orbit. It is the only element that varies with time in an unperturbed orbit (ignoring non-spherical components of Earth's gravity field and the non-gravitational forces), as given by

$$M_0 = n(t - t_0),$$

where n is the mean motion, given by $n = \frac{2\pi}{T}$, where T stands for the orbital period and $(t-t_0)$ denotes the time since the spacecraft was at the periapsis. The set of orbital elements fully describe the spacecraft orbital position and velocity, as illustrated in Fig. 2.3.

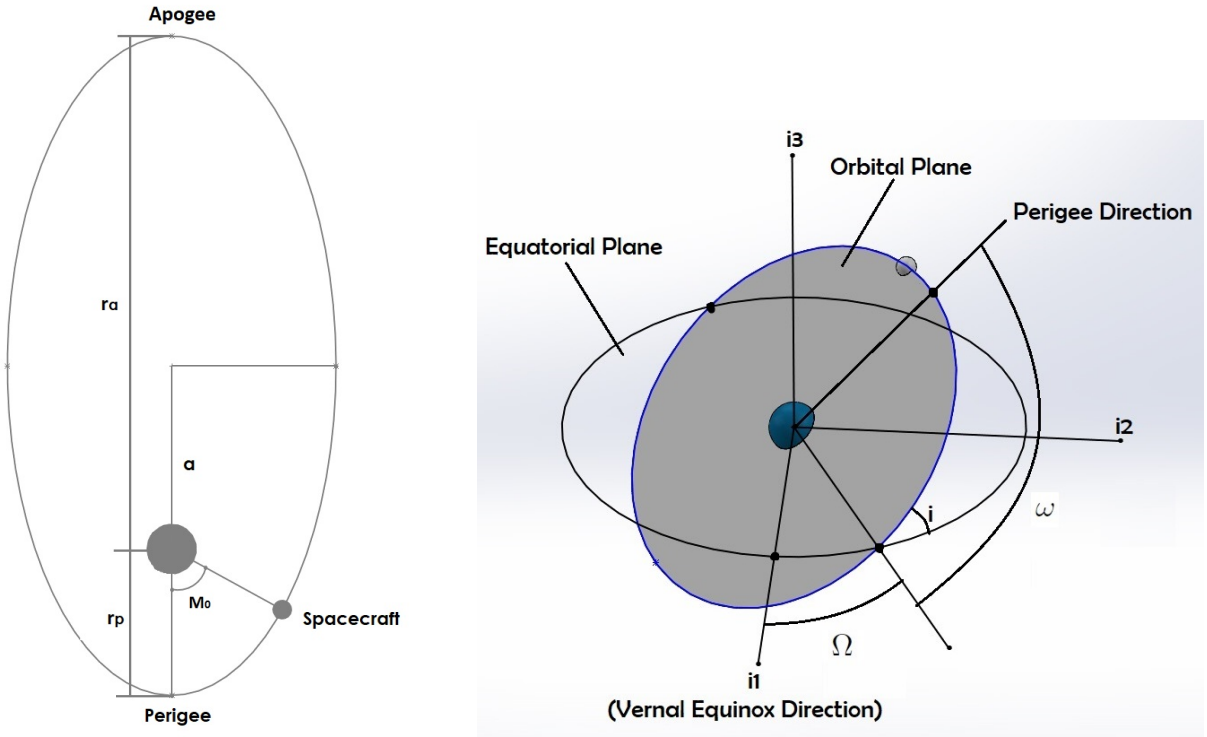

Figure 2.3: Representation of the orbital elements used for the absolute state representation of the spacecraft orbit $(a, e, i, \Omega, \omega, M_0)$.

Several methods were developed to compute the orbital motion using Keplerian elements. The values of these orbital elements can be obtained, at any moment of time, by integrating a set of first-order differential equations. One type of this first-order differential equations often used to deal with spacecraft formation control, and, therefore, with autonomous orbit control, are the Gauss' Variational Equations (GVEs). This set of equations are obtained mathematically from the Lagrange's planetary equations. However, contrasting with Lagrange's equations, they also take into account perturbing forces that cannot be described by a perturbing potential. These perturbing forces are described in the form of accelerations on the spacecraft and are represented on the Local Orbit frame (see Section 2.1.2). It is assumed that the perturbing force is small when compared to the central body force [17]. The so-called Gauss' Variational Equations of Motion (GVEs) are given by

$$\dot{a} = 2\frac{a^2}{\sqrt{\mu p}}\left[{}^{O}f_3 e \sin\theta + {}^{O}f_1 \frac{p}{||\mathbf{r}||}\right], \tag{2.3a}$$

$$\dot{e} = \sqrt{\frac{p}{\mu}}\left[{}^{O}f_3 \sin\theta + {}^{O}f_1(\cos E + \cos\theta)\right], \tag{2.3b}$$

$$\dot{i} = {}^{O}f_2 \frac{||\mathbf{r}||}{\sqrt{\mu p}} \cos u, \tag{2.3c}$$

$$\dot{\Omega} = {}^{O}f_2 \frac{||\mathbf{r}||}{\sqrt{\mu p}\sin i} \sin u, \tag{2.3d}$$

$$\dot{\omega} = -\sqrt{\frac{p}{\mu}}\left[{}^{O}f_2 \frac{||\mathbf{r}||}{p}\cot i \sin u + \frac{1}{e}\left({}^{O}f_3 \cos\theta - {}^{O}f_1\left[1 + \frac{||\mathbf{r}||}{p}\right]\sin\theta\right)\right], \tag{2.3e}$$

$$\dot{M}_0 = n - {}^{O}f_3\left[\frac{2||\mathbf{r}||}{\sqrt{\mu a}} - \frac{1-e^2}{e}\sqrt{\frac{a}{\mu}}\cos\theta\right] - {}^{O}f_1 \frac{1-e^2}{e}\sqrt{\frac{a}{\mu}}\left[1 + \frac{||\mathbf{r}||}{p}\right]\sin\theta, \tag{2.3f}$$

where ${}^{O}f_1$, ${}^{O}f_2$, and ${}^{O}f_3$ are the components of the acceleration vector felt by the spacecraft expressed in the Local Orbit frame and include all the perturbative accelerations, whether they might be expressed by a potential function or not, p is the semi-latus rectum ($p = a(1-e^2)$), E is the eccentric anomaly, θ is the true anomaly, and u is the argument of latitude, which is the angular position of the satellite along its orbit relative to the ascending node [14]. The eccentric anomaly, E, can be obtained by drawing the auxiliary circle of an ellipse with center O and focus F, and drawing a line perpendicular to the semi-major axis and intersecting it at A, see Fig. 2.4, where the point P is the position of the spacecraft. The angle E is then defined as illustrated in Fig. 2.4. The true anomaly, θ, is the angle between the direction of periapsis and the current position of the body, as seen from the main focus of the ellipse, as presented in Fig. 2.4.

Figure 2.4: Representation of eccentric and true anomaly [18].

The GVEs provide a convenient and computationally simple method to assess the effect of a perturbing acceleration on the Keplerian elements, whether it is caused, for example, by the atmospheric drag or by a control acceleration vector [5].

Notice that, for small values of the eccentricity (e), (2.3) suffers from singularities. That makes sense since, for circular orbits, the perigee is not defined and, therefore, the parameters ω and M_0 are inappropriate for describing the satellite's position. The time derivative of the eccentricity, e, should then be

replaced for the eccentricity vector, given by $\mathbf{e} = [e_x \; e_y]^T$, where $e_x = e\cos\omega$ and $e_y = e\sin\omega$. The eccentricity vector is a dimensionless vector in the orbital plane with direction pointing from apogee to perigee of the orbit and with magnitude equal to the orbit's scalar eccentricity. The time derivatives of this vector take the form

$$\dot{e}_x = \sqrt{\frac{p}{\mu}}\left[{}^{O}f_3 \sin\theta + {}^{O}f_1(\cos E + \cos\theta)\right],$$
$$\dot{e}_y = \sqrt{\frac{p}{\mu}}\left[-{}^{O}f_3 \cos\theta + {}^{O}f_1(\sin E + \sin\theta)\right],$$

and (2.3e) and (2.3f) should be replaced by (see [14])

$$\dot{u} \simeq n - \sqrt{\frac{a}{\mu}}(2\,{}^{O}f_3 + {}^{O}f_2 \cot i \sin u). \tag{2.4}$$

As discussed previously, the orbital elements provide a much clearer picture of the geometric properties of the orbit perturbations than the variation of the Cartesian position and velocity. Moreover, the variation of the osculating orbital elements with time is smoother than the variation of the corresponding Cartesian components, which allows for larger integration steps and therefore a faster computation process. On the other hand, the use of Keplerian elements leads to a more complex dynamic system and linearization process, which may make the use of some control strategies more involved.

2.3 Perturbation Forces

Perturbation forces cause a time-variation of the Keplerian elements, causing the orbit to deviate from the unperturbed Keplerian model. In this section, the most significant forces that affect the spacecraft are described.

By Newton's Second Law, these forces cause a perturbative acceleration on the spacecraft. In Fig. 2.5 it is possible to compare the resulting acceleration caused by several different perturbation forces, as a function of the spacecraft altitude.

As illustrated in Fig. 2.5, the most significant perturbative accelerations in low Earth orbits are atmospheric drag (${}^{I}\mathbf{f}_{aero}$), solar radiation pressure (${}^{I}\mathbf{f}_{SRP}$), third-body gravitational attraction (${}^{I}\mathbf{f}_{TBG}$), and non-spherical Earth gravity field (${}^{I}\mathbf{f}_{\oplus}$). Tidal perturbation, caused by the ocean and Earth's crust tides due to the perturbing effects of the Sun and Moon, is not considered given its small magnitude when compared to other perturbative accelerations.

In the following subsections, the different perturbative accelerations are described. For the sake of clarity, these accelerations are expressed in the ToD reference frame. Therefore, a rotation to the Local Orbit frame (as shown in Section 2.1.2) is necessary in order to use them in the GVEs. Also, the perturbation forces are represented in these equations by its resulting acceleration on the spacecraft. Thus, all the forces in this section are mathematically modeled as accelerations, whether they might be expressed by a potential function or not.

The resulting perturbative acceleration (${}^{O}\mathbf{f} = [{}^{O}f_1 \; {}^{O}f_2 \; {}^{O}f_3]^T$), in the O-frame, is given by

$$^{O}\mathbf{f} = {}^{O}\mathbf{f}_{aero} + {}^{O}\mathbf{f}_{SRP} + {}^{O}\mathbf{f}_{TBG} + {}^{O}\mathbf{f}_{\oplus},$$

where all the accelerations are expressed in the Local Orbit frame [5].

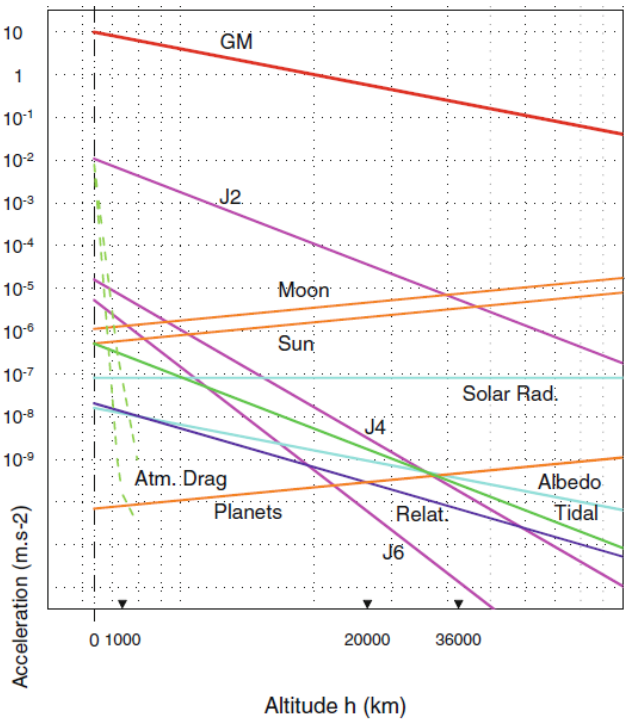

Figure 2.5: Central acceleration (GM) and perturbative accelerations as a function of the spacecraft altitude, shown on a logarithmic scale [19].

2.3.1 Atmospheric Drag

Spacecrafts in low orbits experience a significant effect caused by the collision with particles of the upper atmosphere. This interaction is manifested as an aerodynamic drag force that opposes the spacecraft velocity vector. The acceleration caused by the atmospheric drag force is approximated by

$$^{I}\mathbf{f}_{aero} = -\frac{1}{2}\frac{\rho C_D S}{M} \|\mathbf{v}_{rel}\| \mathbf{v}_{rel}, \tag{2.5}$$

where ρ is the local atmospheric density, C_D is a dimensionless drag coefficient, S is the spacecraft area projected along the direction of motion, M is the spacecraft total mass, and $\mathbf{v}_{rel}$ is the relative velocity of the spacecraft with respect to the atmosphere [11].

The relative velocity, $\mathbf{v}_{rel}$, is different from the spacecraft orbital velocity in the ToD frame since the Earth's atmosphere is not stationary. Then, a simple approximation can be done in order to obtain the relative velocity. If it is assumed that the atmosphere rotates with the same angular velocity as the Earth, then

$$\mathbf{v}_{rel} = \mathbf{v} - \dot{\boldsymbol{\theta}} \times \mathbf{r},$$

where **v** is the velocity vector of the spacecraft expressed on the ToD frame and $\dot{\boldsymbol{\theta}}$ is the angular velocity vector of the Earth on the ToD frame, given by $\dot{\boldsymbol{\theta}} = \dot{\theta}\,[0\ 0\ 1]^T$, see [20].

The drag coefficient, C_D, quantifies how the spacecraft interacts with the surrounding medium and it is often determined via experimental or finite element analysis. As to the atmospheric density, ρ, the most simple model assumes that it decays exponentially with increasing height. This model is fully static, in the sense that the densities are independent of time, and it also assumes an axially symmetric atmosphere about the polar axis. The exponential model is given by

$$\rho = \rho_0\, exp[-(\bar{h} - \bar{h}_0)/H],$$

where ρ_0 is the atmospheric density at reference altitude $\bar{h}_0$, H is a scaling factor that is called the density scale height, and $\bar{h}$ is the altitude of the satellite above the surface of the Earth [11].

The NRLMSISE-00 is a more accurate model to obtain ρ. This empirical atmospheric model computes the neutral temperature and densities in Earth's atmosphere from ground to thermospheric heights (up to 1000 km). The NRLMSISE-00 was released in 2001 by the United States Naval Research Laboratory as an upgrade of the MSISE-90 atmospheric model, updated with actual satellite data obtained using mass spectrometry and incoherent scatter radar techniques. To obtain the local atmospheric density, the geodetic latitude, longitude, and altitude of the spacecraft, as well as the local time, are required [21].

2.3.2 Solar Radiation Pressure

The mechanism by which the solar radiation pressure (SRP) affects the orbit of a spacecraft is related to the momentum exchange between the photons emitted by the Sun and the spacecraft [11]. Unlike the atmospheric drag perturbation, the SRP does not act throughout the entire orbit, since it only contributes when the spacecraft is not in the shadow of the Earth.

The acceleration caused by the SRP is given by

$$^{I}\mathbf{f}_{SRP} = -\,C_R \frac{I_S\, A_S}{M\, c}\mathbf{e_S}, \tag{2.6}$$

where C_R is the spacecraft's reflectivity, I_S is the energy flux of the incoming radiation, A_S is the cross-sectional area of the spacecraft exposed to the radiation, c is the speed of light, and $\mathbf{e_S}$ is the unit vector from the spacecraft to the Sun [14]. The value of I_S fluctuates during a year due to the Earth's varying distance from the Sun. This variation can be modeled by

$$I_S = \frac{1361}{1 + 0.0334\ \mathsf{cos}(2\pi D_{ap}/365)}\ W/m^2,$$

where D_{ap} is the number of days from when the Earth is at aphelion [14].

2.3.3 Third-Body Gravitational Attraction

Nearby celestial bodies also cause a perturbative force that affects the spacecraft orbit about the Earth. The gravitational force caused by several celestial bodies induces an acceleration on the spacecraft, given by

$$ {}^{I}\mathbf{f}_{TBG} = -\sum_{i=1}^{N}\left[\mu_{TBG_i}\left(\frac{\mathbf{r}-\mathbf{r}_{TBG_i}}{d_{TBG_i}^3}-\frac{\mathbf{r}_{TBG_{I_i}}}{\|\mathbf{r}_{TBG_i}\|^3}\right)\right], \tag{2.7} $$

where N is the number of celestial bodies that have a perturbative effect on the spacecraft, μ_{TBG_i} is the standard gravitational parameter of the celestial body, d_{TBG_i} is the distance between the spacecraft and the body, and $\mathbf{r}_{TBG_i}$ is the celestial body position expressed in the ToD frame [14].

In order to compute the third-body perturbative acceleration, the positions of the spacecraft and the celestial body should be determined relative to the ToD reference frame. A closer inspection of (2.7) shows that the perturbative acceleration is given by the difference between the celestial body gravity acting on the spacecraft and the celestial body gravity acting on the Earth [20]. As it was presented in the introductory part of this section, the two bodies with the greatest influence in low Earth orbits are the Moon and the Sun. Therefore, neglecting the influence of other celestial bodies, the third-body acceleration is given by

$$ {}^{I}\mathbf{f}_{TBG} = {}^{I}\mathbf{f}_{TBG_{Moon}} + {}^{I}\mathbf{f}_{TBG_{Sun}}. $$

2.3.4 Earth Gravity Field

Since the Earth is not a perfect sphere and its mass is not uniformly distributed throughout the Earth, and having in consideration that gravity depends directly on mass, it follows that the gravity field is not uniform.

One approach to deal with the non-uniformity of the gravitational field is to divide the Earth into a large number, N, of portions of mass, m_i, located at point $\mathbf{r}_i$. With that in mind, it is possible to obtain the gravitational potential at a point $\mathbf{r}$ as

$$ U_{\oplus}(\mathbf{r}) = \sum_{i=1}^{N}\frac{G\,m_i}{\|\mathbf{r}-\mathbf{r}_i\|}, $$

where G is Newton's universal gravitational constant [11]. Alternatively, the gravitational potential can be written as a spherical harmonics expansion, as given by

$$ U_{\oplus}(r,\lambda,\phi) = \frac{\mu}{r}\left[1+\sum_{n=1}^{\infty}\left(\frac{R_{\oplus}}{r}\right)^n\sum_{m=0}^{n}P_n^m(\sin\lambda)[C_n^m\cos(m\phi)+S_n^m\sin(m\phi)]\right], \tag{2.8} $$

where $\{r,\lambda,\phi\}$ are the spherical coordinates of the point that is considered, relative to the geocentric rotating reference frame (r is the distance from the mass center of the Earth, λ is the geocentric latitude, and ϕ is the geographic longitude), $R_{\oplus}$ is the mean equatorial Earth radius, C_n^m and S_n^m are model

parameters, and P_n^m are associated Legendre functions of degree *n* and order *m*, see [14]. The spherical harmonics fall into three classes: zonal harmonics for $m = 0$, tesseral harmonics for $0 < m < n$, and sectoral harmonics for $m = n$, as shown in Fig. 2.6.

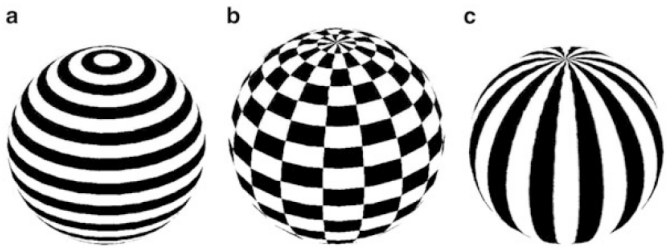

Figure 2.6: Types of spherical harmonics: (a) Zonal. (b) Tesseral. (c) Sectoral [11].

Zonal harmonics are of particular interest since they are symmetrical about the polar axis, which means that there is no dependence on the longitude or the Greenwich hour angle. Also, the strongest perturbations due to the Earth shape arises from these harmonics [11]. A specific notation, $J_n = -C_n^0$, is used for these coefficients. The even zonal harmonics, those of degree 2,4,6..., are symmetric about the equator, contrasting with the odd zonal harmonics, those of degree 3,5,7,..., that are anti-symmetric about the equator, causing near-sinusoidal oscillations in several orbital elements [22]. The values for the first six zonal coefficients are presented in Table 2.1. Note that the J_2 coefficient is about 400 times larger than the next largest aspherical coefficient, and is, therefore, the strongest perturbation due to the Earth's shape.

Table 2.1: Zonal coefficients [11].

i	J_i	$\times 10$
2	1.08262668355	-3
3	-2.53265648533	-6
4	-1.61962159137	-6
5	-2.27296082869	-7
6	5.40681239107	-7

The perturbative acceleration due to zonal harmonics can be obtained by the gradient of the potential given by (2.8), considering $m = 0$. Also, note that the first term μ/r of (2.8) is already considered in the left-hand side of (2.1). Moreover, since the equatorial plane of True of Date reference frame is (nearly) aligned with the Earth equator, the values of J_i can be directly used to compute the associated accelerations expressed in the ToD reference frame. Then, considering the six zonal coefficients presented in Table 2.1, the perturbative acceleration due to the Earth gravity field, in the ToD frame, is given by (see [11])

$$ {}^{I}\mathbf{f}_{\oplus} = \sum_{i=2}^{6} {}^{I}\mathbf{f}_{J_i}, $$

where the individual ${}^{I}\mathbf{f}_{J_i}$ terms are given by

$$
{}^{I}\mathbf{f}_{J_2} = -\frac{3}{2} J_2 \frac{\mu}{||\mathbf{r}||^2} \left(\frac{R_\oplus}{||\mathbf{r}||} \right)^2 \begin{bmatrix} \left(1 - 5 \left(\frac{\mathbf{r}.\mathbf{i_3}}{||\mathbf{r}||} \right)^2 \right) \frac{\mathbf{r}.\mathbf{i_1}}{||\mathbf{r}||} \\ \left(1 - 5 \left(\frac{\mathbf{r}.\mathbf{i_3}}{||\mathbf{r}||} \right)^2 \right) \frac{\mathbf{r}.\mathbf{i_2}}{||\mathbf{r}||} \\ \left(3 - 5 \left(\frac{\mathbf{r}.\mathbf{i_3}}{||\mathbf{r}||} \right)^2 \right) \frac{\mathbf{r}.\mathbf{i_3}}{||\mathbf{r}||} \end{bmatrix},
$$

$$
{}^{I}\mathbf{f}_{J_3} = -\frac{1}{2} J_3 \frac{\mu}{||\mathbf{r}||^2} \left(\frac{R_\oplus}{||\mathbf{r}||} \right)^3 \begin{bmatrix} 5 \left(7 \left(\frac{\mathbf{r}.\mathbf{i_3}}{||\mathbf{r}||} \right)^3 - 3 \left(\frac{\mathbf{r}.\mathbf{i_3}}{||\mathbf{r}||} \right) \right) \frac{\mathbf{r}.\mathbf{i_1}}{||\mathbf{r}||} \\ 5 \left(7 \left(\frac{\mathbf{r}.\mathbf{i_3}}{||\mathbf{r}||} \right)^3 - 3 \left(\frac{\mathbf{r}.\mathbf{i_3}}{||\mathbf{r}||} \right) \right) \frac{\mathbf{r}.\mathbf{i_2}}{||\mathbf{r}||} \\ 3 \left(10 \left(\frac{\mathbf{r}.\mathbf{i_3}}{||\mathbf{r}||} \right)^2 - \frac{35}{3} \left(\frac{\mathbf{r}.\mathbf{i_3}}{||\mathbf{r}||} \right)^4 - 1 \right) \end{bmatrix},
$$

$$
{}^{I}\mathbf{f}_{J_4} = -\frac{5}{8} J_4 \frac{\mu}{||\mathbf{r}||^2} \left(\frac{R_\oplus}{||\mathbf{r}||} \right)^4 \begin{bmatrix} \left(3 - 42 \left(\frac{\mathbf{r}.\mathbf{i_3}}{||\mathbf{r}||} \right)^2 + 63 \left(\frac{\mathbf{r}.\mathbf{i_3}}{||\mathbf{r}||} \right)^4 \right) \frac{\mathbf{r}.\mathbf{i_1}}{||\mathbf{r}||} \\ \left(3 - 42 \left(\frac{\mathbf{r}.\mathbf{i_3}}{||\mathbf{r}||} \right)^2 + 63 \left(\frac{\mathbf{r}.\mathbf{i_3}}{||\mathbf{r}||} \right)^4 \right) \frac{\mathbf{r}.\mathbf{i_2}}{||\mathbf{r}||} \\ -\left(15 - 70 \left(\frac{\mathbf{r}.\mathbf{i_3}}{||\mathbf{r}||} \right)^2 + 63 \left(\frac{\mathbf{r}.\mathbf{i_3}}{||\mathbf{r}||} \right)^4 \right) \frac{\mathbf{r}.\mathbf{i_3}}{||\mathbf{r}||} \end{bmatrix},
$$

$$
{}^{I}\mathbf{f}_{J_5} = -\frac{1}{8} J_5 \frac{\mu}{||\mathbf{r}||^2} \left(\frac{R_\oplus}{||\mathbf{r}||} \right)^5 \begin{bmatrix} 3 \left(35 \left(\frac{\mathbf{r}.\mathbf{i_3}}{||\mathbf{r}||} \right) - 210 \left(\frac{\mathbf{r}.\mathbf{i_3}}{||\mathbf{r}||} \right)^3 + 231 \left(\frac{\mathbf{r}.\mathbf{i_3}}{||\mathbf{r}||} \right)^5 \right) \frac{\mathbf{r}.\mathbf{i_1}}{||\mathbf{r}||} \\ 3 \left(35 \left(\frac{\mathbf{r}.\mathbf{i_3}}{||\mathbf{r}||} \right) - 210 \left(\frac{\mathbf{r}.\mathbf{i_3}}{||\mathbf{r}||} \right)^3 + 231 \left(\frac{\mathbf{r}.\mathbf{i_3}}{||\mathbf{r}||} \right)^5 \right) \frac{\mathbf{r}.\mathbf{i_2}}{||\mathbf{r}||} \\ \left(15 - 315 \left(\frac{\mathbf{r}.\mathbf{i_3}}{||\mathbf{r}||} \right)^2 + 945 \left(\frac{\mathbf{r}.\mathbf{i_3}}{||\mathbf{r}||} \right)^4 - 693 \left(\frac{\mathbf{r}.\mathbf{i_3}}{||\mathbf{r}||} \right)^6 \right) \end{bmatrix},
$$

$$
{}^{I}\mathbf{f}_{J_6} = \frac{1}{16} J_6 \frac{\mu}{||\mathbf{r}||^2} \left(\frac{R_\oplus}{||\mathbf{r}||} \right)^6 \begin{bmatrix} \left(35 - 945 \left(\frac{\mathbf{r}.\mathbf{i_3}}{||\mathbf{r}||} \right)^2 + 3465 \left(\frac{\mathbf{r}.\mathbf{i_3}}{||\mathbf{r}||} \right)^4 - 3003 \left(\frac{\mathbf{r}.\mathbf{i_3}}{||\mathbf{r}||} \right)^6 \right) \frac{\mathbf{r}.\mathbf{i_1}}{||\mathbf{r}||} \\ \left(35 - 945 \left(\frac{\mathbf{r}.\mathbf{i_3}}{||\mathbf{r}||} \right)^2 + 3465 \left(\frac{\mathbf{r}.\mathbf{i_3}}{||\mathbf{r}||} \right)^4 - 3003 \left(\frac{\mathbf{r}.\mathbf{i_3}}{||\mathbf{r}||} \right)^6 \right) \frac{\mathbf{r}.\mathbf{i_2}}{||\mathbf{r}||} \\ \left(2205 \left(\frac{\mathbf{r}.\mathbf{i_3}}{||\mathbf{r}||} \right)^2 - 4851 \left(\frac{\mathbf{r}.\mathbf{i_3}}{||\mathbf{r}||} \right)^4 + 3003 \left(\frac{\mathbf{r}.\mathbf{i_3}}{||\mathbf{r}||} \right)^6 - 315 \right) \frac{\mathbf{r}.\mathbf{i_3}}{||\mathbf{r}||} \end{bmatrix}.
$$

2.4 Validation of the Orbital Motion Models

In order to verify the validity of the orbital motion models proposed in Section 2.2, a Simulink model was developed. In it, the two forms of the equations of motion that were presented, in Cartesian coordinates (2.2) and Keplerian elements (2.3), are implemented, together with the models that describe the different types of perturbation forces that affect a satellite in orbit about the Earth, as introduced in Section 2.3.

Several simulations are carried out to evaluate the accuracy of the models and, in this section, the most relevant results are presented. To perform the simulations, a spacecraft with the physical characteristics and orbit as described in Table 2.2 is used. The parameters are arbitrary and describe a generic spacecraft in LEO orbit.

Table 2.2: Test spacecraft physical characteristics and orbit parameters.

Test spacecraft	
Physical Parameters	Keplerian Elements
Mass = 100 kg	$a = 7000$ km
Reflectivity Coefficient = 1.4	$e = 0.01$
Drag Coefficient = 2.2	$i = 5$ deg
Cross-Sectional Area = 1 m^2	$\Omega = 60$ deg
	$\omega = 10$ deg
	$M_0 = 0$ deg

Initially, a comparison between the two orbital motion models (Cartesian coordinates orbital motion model (2.2) and GVEs (2.3)) is made by computing the difference in the position of the spacecraft expressed in the ToD frame when propagated using the two models. The Runge-Kutta 4th order method, with a time step of 1 s, is used for the propagation of this spacecraft. The magnitude of the position difference is depicted in Fig. 2.7, for a simulation of 4 four complete orbits around the Earth (approximately 23300 s). In this simulation, the perturbative accelerations caused by the atmospheric drag, the SRP, the third-body gravitational attraction, and the Earth gravity field affect the spacecraft orbit. The position difference between the two orbital motion models derives from both numerical errors related to the Runge-Kutta 4th order method and the different strategies of each orbital motion model.

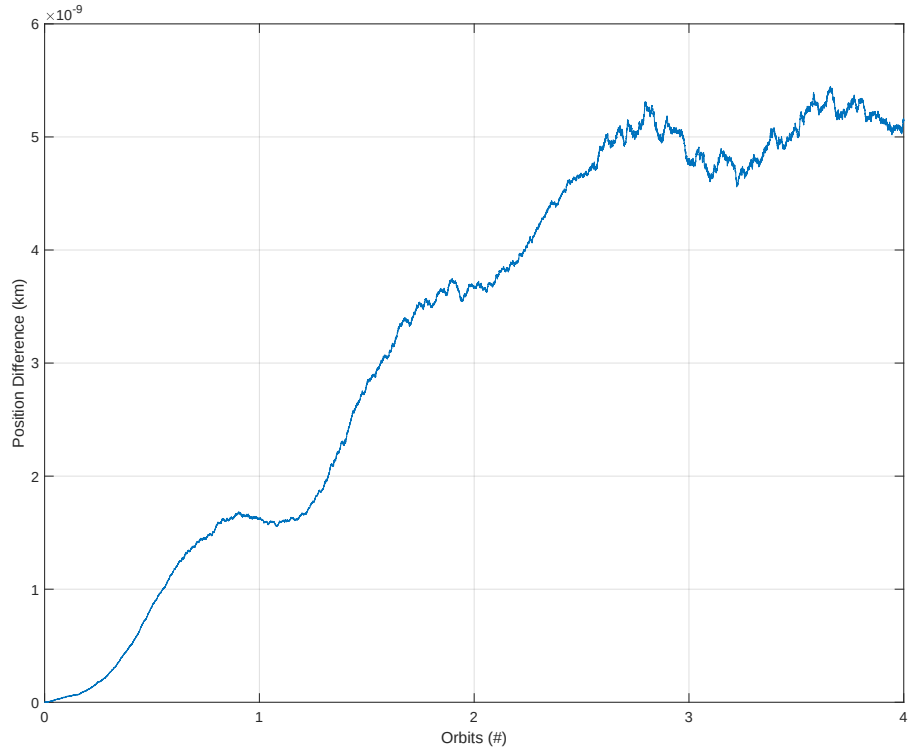

Figure 2.7: Modulus of the difference in the position of the Test spacecraft propagated using the Cartesian coordinates orbital motion model and GVEs.

In order to validate both the orbital motion and perturbations models, a simulation is performed using NASA's General Mission Analysis Tool (GMAT). The same spacecraft and orbit described in Table 2.2 are used and the perturbation forces described in Section 2.3 are selected in the GMAT propagation model. The simulator outputs the position and the velocity, at each time step, which are then used to define a Local Orbit reference frame (see Section 2.1.2), centered at the spacecraft's center of mass propagated in the GMAT environment. After that, the position of the test spacecraft propagated using GVEs in the Simulink model is expressed in the GMAT Local Orbit reference frame, so the difference in position between the two environments could be compared in this reference frame. In this simulation, the Forward Euler method, with a time step of 1 s, is used for the propagation of the spacecraft. This method is interesting for some applications since it is computationally more efficient than the Runge-Kutta 4th order method, so its accuracy is assessed in this simulation. The Forward Euler method is not used to propagate the spacecraft when working with Cartesian coordinates since the position and the velocity vectors present significant variations over time when compared to the Keplerian elements, which leads to inaccurate results due to the simplicity of the propagation method. Therefore, a comparison between the propagation of the test spacecraft using GMAT and the Cartesian coordinates orbital motion model is not presented since a more accurate propagation method, such as the Runge-Kutta 4th order method, is needed. In this case, the difference in position between the propagation using GVEs and the Cartesian coordinates orbital motion model is negligible, as shown in Fig. 2.7, so the results of comparing both models with the propagation using GMAT are similar.

The results of comparing the position obtained using GMAT with the position obtained using GVEs are presented in Fig. 2.8. At the end of the simulation, the magnitude of the difference between the positions is 1.86 km. It is possible to notice a secular variation in the o_1 axis (along-track) that is the major responsible for the difference in the position of the spacecraft when propagated in the two different environments.

An analysis is carried out in order to understand the cause of this variation and evaluate the accuracy of the model. For that, an initial analysis is made by comparing the position of the spacecraft, propagated using both the GMAT and the Simulink models, in an environment where no perturbation forces are present. The result is presented in Fig. 2.9a, where it is possible to observe that the difference between the two environments presents a maximum value of 1.25×10^{-3} km when propagated during four complete orbits around the Earth, which can be assumed to be caused by numerical errors of the propagation methods.

After, the SRP and the third-body gravitational attraction, with contributions from the Sun and the Moon, are added to both GMAT and the Simulink model. The difference in position, when each of these perturbation forces is added to the models, is presented in Fig. 2.9b and Fig. 2.9c. It is possible to notice that the difference has increased due to the addition of these perturbation forces, being more significant, between the two, in the case of the solar radiation pressure, although it still presents a small value when compared to the plot of Fig. 2.8. It is possible to assume that this increase in the position difference is derived from a different implementation of solar radiation pressure and third-body gravitational attraction perturbations models in the two different environments. Also, regarding the solar radiation pressure, it

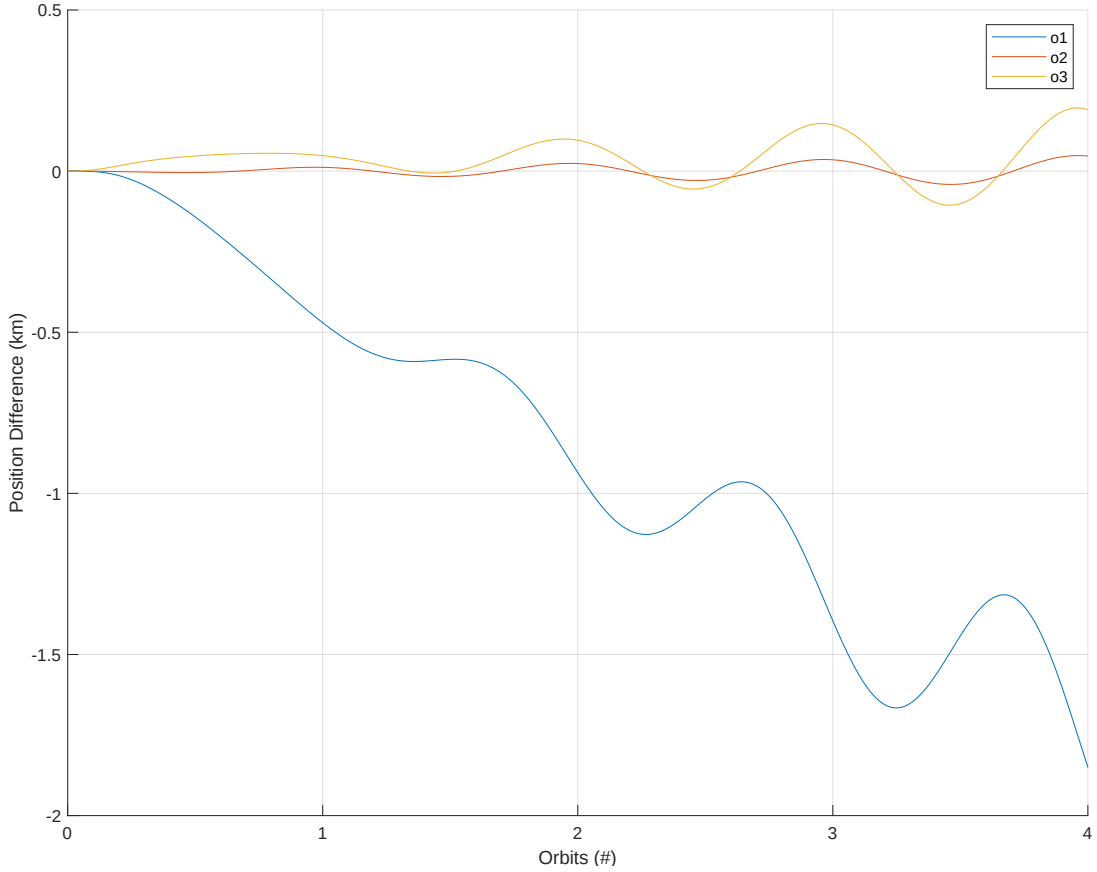

Figure 2.8: Position of the spacecraft, propagated using GVEs, expressed in a Local Orbit frame centered at the spacecraft center of mass propagated using GMAT.

must be taken into account that eclipse events are not considered in the Simulink model.

The atmospheric drag perturbation is then added to the two environments. As presented in Fig. 2.9d, the addition of this perturbation results in an increase of the error between the two models, which is mainly derived from the different atmospheric models used in the two environments (MSISE90 in GMAT and NRLMSISE-00 in the Simulink model). Since the drag force is proportional to the atmospheric density and different atmospheric models may present differences for the total densities in the same orbital location, the atmospheric drag perturbation force presents different values in the two environments, which is responsible for the error presented. It is expected that this error increase when the altitude of the orbit is reduced since, in this case, the perturbation due to the atmospheric drag is stronger.

It is when the non-uniform gravity field of the Earth is added to the models that the position difference presented in Fig. 2.8 arises. The difference presented in Fig. 2.9e is related to different Earth gravity models used in the two environments since GMAT uses a more accurate geopotential model – EGM96. This Earth gravitational model was published in 1996 and uses more harmonic coefficients to provide a precise model of the Earth's gravity field. Therefore, the error presented can be reduced if a more precise gravity field model is used in the Simulink model. Moreover, numerical errors related to the Forward Euler propagation method are also responsible for the position error presented in the simulations.

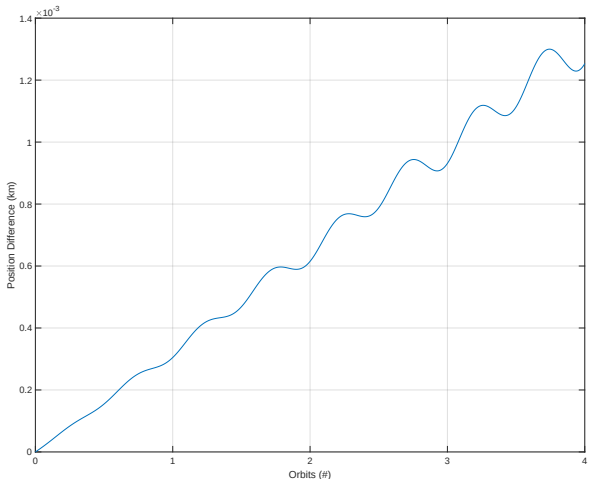

(a) Without perturbations.

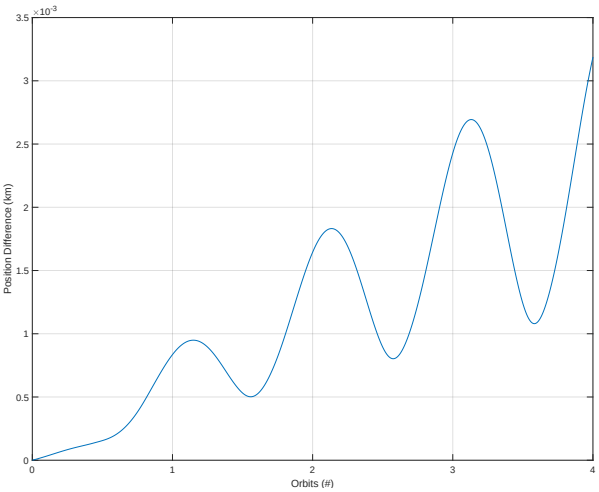

(b) Solar Radiation Pressure.

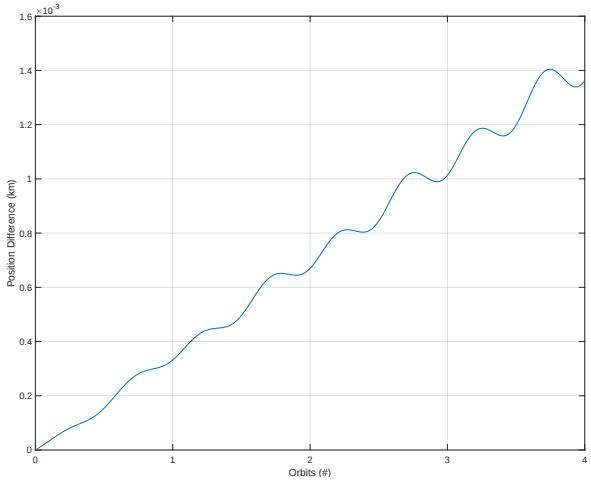

(c) Third-Body Gravitational Attraction.

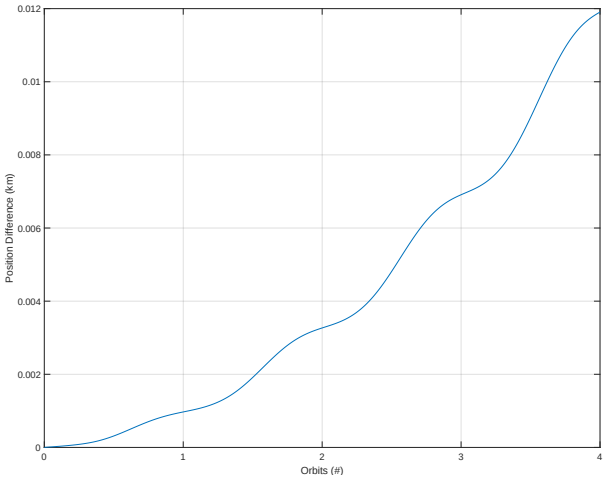

(d) Atmospheric Drag.

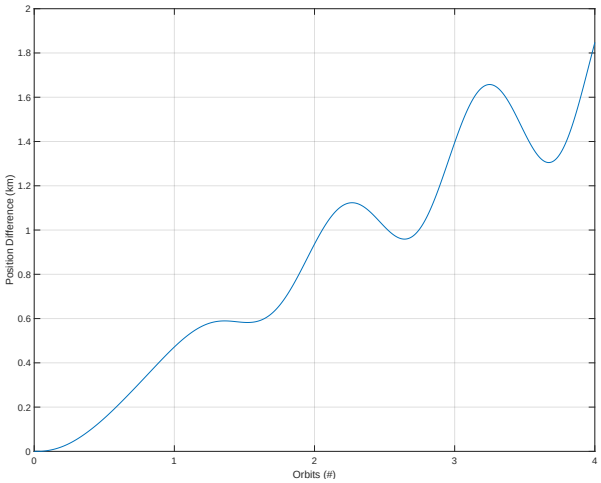

(e) Earth Gravity Field.

Figure 2.9: Modulus of the difference in the position of the Test spacecraft propagated using GMAT and the Simulink model when different perturbation forces are acting on the spacecraft.

Using the developed Simulink model, it is possible to evaluate the effect that the perturbation forces, described in Section 2.3, have on the position of the Test spacecraft in its orbit. Utilising the parameters

described in Table 2.2, a simulation is carried out during 20 complete orbits around the Earth, where the spacecraft position is propagated in an environment where no perturbation forces are present. This position with time, of the unperturbed orbit, is used to define a Local Orbit reference frame, centered on the spacecraft center of mass. After that, the perturbed spacecraft position is propagated and expressed in the obtained unperturbed Local Orbit frame, at each time step. The results are presented in Fig. 2.10. It is possible to notice that the perturbation forces have a major impact on the spacecraft position, leading to a significant difference in position between a perturbed and an unperturbed spacecraft with time. In some cases, this position difference may not be compliant with the mission requirements, which motivates the need for orbit control systems to reduce this error.

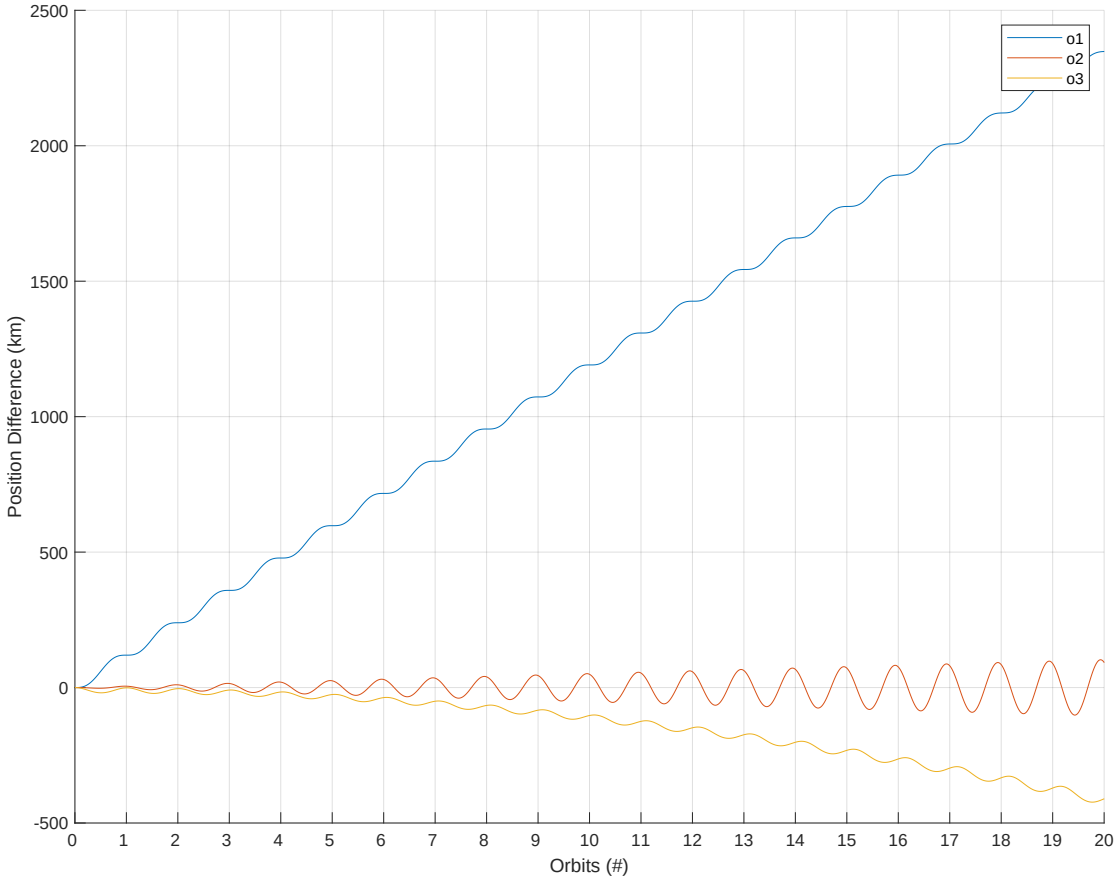

Figure 2.10: Position of the perturbed spacecraft in a Local Orbit frame centered at the unperturbed spacecraft center of mass.

2.5 Control Methodology

Two different control strategies are considered in this thesis: linear quadratic regulator (LQR) and model predictive control (MPC). In this section, a brief description of these two methodologies is presented, as well as a comparison between the two.

2.5.1 Linear Quadratic Regulator (LQR)

An LQR controller is obtained as a solution of an optimisation process, subjected, in this case, to the linear time-invariant system dynamics $\dot{\mathbf{x}} = \mathbf{A}\mathbf{x} + \mathbf{B}\mathbf{u}$, which is a mathematical representation of the system behaviour over time, where $\mathbf{x}$ is the system state, $\mathbf{u}$ is the control input, $\mathbf{A}$ is the state matrix, and $\mathbf{B}$ is the input matrix. The LQR minimises a cost function expressed as the integral of a quadratic form of the error between the state and the reference plus a second quadratic form of the input. Considering the control window as infinite, the cost function of the LQR is given by

$$J = \frac{1}{2}\int_0^\infty \mathbf{x}^T\mathbf{Q}\mathbf{x} + \mathbf{u}^T\mathbf{R}\mathbf{u}\, dt, \tag{2.9}$$

where $\mathbf{Q} \succeq 0$ is a symmetric, positive semi-definite matrix that weighs the state error and $\mathbf{R} \succ 0$ is a symmetric, positive definite matrix that weighs the input [23]. In other words, $\mathbf{x}^T\mathbf{Q}\mathbf{x}$ represents a penalty on the state error and $\mathbf{u}^T\mathbf{R}\mathbf{u}$ a penalty on the control input, in order to minimise the fuel consumption and eventually prevent saturation of the actuators. The correct tuning of these matrices is crucial to obtain an efficient and effective controller, in a trade-off between control action cost and control accuracy [5].

The optimisation process consists of determining the control action $\mathbf{u}$ that minimises J. This can be achieved if $\mathbf{A}$ and $\mathbf{B}$ are stabilisable, by finding the symmetric matrix $\mathbf{P} \succeq 0$ that is the solution of the algebraic Riccati equation (see [23])

$$\mathbf{A}^T\mathbf{P} + \mathbf{P}\mathbf{A} - \mathbf{P}\mathbf{B}\mathbf{R}^{-1}\mathbf{B}^T\mathbf{P} + \mathbf{Q} = \mathbf{0}.$$

The LQR state-feedback gain, or Kalman gain, $\mathbf{K}$, is given by

$$\mathbf{K} = \mathbf{R}^{-1}\mathbf{B}^T\mathbf{P},$$

which in turn yields the linear control law that minimises the cost function (2.9)

$$\mathbf{u} = -\mathbf{K}\mathbf{x}. \tag{2.10}$$

The Kalman gain can be computed offline. Then, the optimal control action, $\mathbf{u}$, is computed using (2.10) during the control loop and applied to the plant [23].

2.5.2 Model Predictive Controller (MPC)

Model predictive control is a control strategy that uses predictions of the behaviour of the plant, which corresponds to the system model, over time in a defined time horizon, to find the optimum control strategy. In other words, the controller evaluates the evolution of the state during that time horizon, using a system model and the current state of the plant as the initial state, for different input strategies to find the minimum of a cost function.

The proper tuning of the MPC parameters (see Fig. 2.11) is of extreme importance to obtain an efficient controller that drives the system to the reference without an excessive computational cost [24]. The parameters that characterise an MPC are:

- Sample time, Ts - The plant model used by the MPC to predict the system behaviour is a discrete-time model. Therefore, the sample time is used in this discrete model to propagate the prediction of the system. In general, a large sample time will reduce the accuracy of the propagation model, but will increase the prediction time, for the same number of prediction steps;

- Prediction horizon, p_h - The number of steps that the MPC uses to predict the model behaviour. The product of the prediction horizon and the sample time is the prediction time, that is, how far the controller looks into the future. The bigger the prediction horizon, the further the controller will look into the future to find the best actuation strategy, despite causing an increase in the computational effort;

- Control horizon, m - The number of control actions computed by the MPC. Each control move is obtained by the optimiser, at each prediction step, until the end of the control horizon. A smaller control horizon will decrease the computational effort but may lead to a less accurate prediction since the controller holds constant its output computed in the last step of the control horizon for the remaining prediction horizon steps. The control horizon must verify $m \leq p_h$.

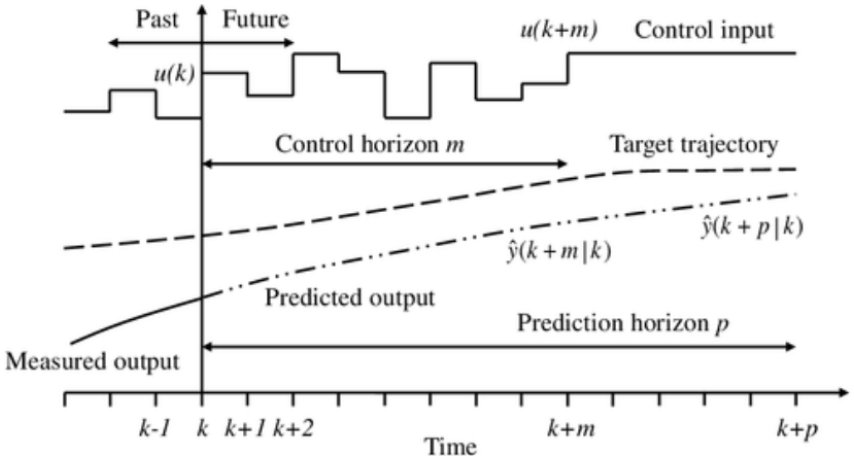

Figure 2.11: Principle of MPC parameters [24].

The control inputs to be applied to the plant until the next control interval are obtained by solving an optimisation problem, that includes the following features (see [25]):

- Cost function - a scalar measure of the controller performance to be minimised. The cost function used in the controller developed for this thesis is the sum of two terms, both of them including weights to balance competing objectives,

$$J(\mathbf{z_k}) = J_{\mathbf{y}}(\mathbf{z_k}) + J_{\mathbf{u}}(\mathbf{z_k}),$$

  where $\mathbf{z_k} = [\mathbf{u}(k)^T\ \mathbf{u}(k+1)^T\ ...\ \mathbf{u}(k+p_h)^T]$ is the control input vector to be used during the prediction horizon.

– Reference tracking – this term is related to the difference between the plant output and the reference, and is given by

$$J_{\mathbf{y}}(\mathbf{z_k}) = \sum_{j=1}^{n_{\mathbf{y}}} \sum_{i=1}^{p_h} \left[w_{i,j}^{\mathbf{y}} (\mathbf{r}_j(k+i) - \mathbf{y}_j(k+i)) \right]^2, \tag{2.11}$$

where k is the current simulation step, $n_{\mathbf{y}}$ is the number of plant output variables, $\mathbf{r}_j(k+i)$ is the reference value for j-th plant output at i-th prediction horizon step, in engineering units, $\mathbf{y}_j(k+i)$ is the predicted value of j-th plant output at i-th prediction horizon step, in engineering units, and $w_{i,j}^{\mathbf{y}}$ is the tuning weight for j-th plant output at i-th prediction horizon step (dimensionless).

– Manipulated variable cost – this term penalises the control actions to be taken in order to prevent the saturation of the actuators and reduce the use of energy by the system, and is given by

$$J_{\mathbf{u}}(\mathbf{z_k}) = \sum_{j=1}^{n_{\mathbf{u}}} \sum_{i=0}^{p_h-1} \left[w_{i,j}^{\mathbf{u}} \mathbf{u}_j(k+i) \right]^2, \tag{2.12}$$

where $n_{\mathbf{u}}$ is the number of control input variables, $w_{i,j}^{\mathbf{u}}$ is the tuning weight for j-th control input variable at i-th prediction horizon step (dimensionless), and $\mathbf{u}_j(k+i)$ is the predicted value for j-th control input variable at i-th prediction horizon step, in engineering units.

- Constraints - conditions that the solution must satisfy, such as bounds on the control inputs due to actuators saturation. These constraints might be hard if the optimiser does not consider solutions that violate these constraints, or soft if their violation is allowed but with a penalty considered in the cost function. In the controller developed in this thesis, only hard constraints were considered. If soft constraints were added to the problem, a new term should be included in the cost function to quantify the worst-case constraint violation.

Nonlinear Model Predictive Controller

In the case of a nonlinear system, which can not be easily approximated by a linear model, it is possible to use nonlinear MPC. This method allows a more accurate representation of the system as the state function since it uses the original nonlinear plant model, improving the prediction results and, therefore, leading to better control actions. This method also allows the use of nonlinear constraints and cost function.

However, the use of nonlinear models might lead to a non-convex optimisation process. In that case, the cost function has several local optimums and, in order to find the global optimum, a more complex computation process is needed [26].

2.5.3 Comparison between LQR and MPC

One of the main advantages of the nonlinear MPC over the LQR controller is that the MPC handles constraints in the optimisation process. Therefore, the controller finds a solution for the minimisation

problem without exceeding the imposed limits. The use of an LQR controller might lead to the computation of control inputs that will be saturated by the actuators, worsening the controller performance.

Furthermore, unlike the LQR, the MPC is able to utilise the nonlinear system dynamics, without a previous linearization process, as explained before, using a more accurate representation of the plant. In the case of the LQR, it is expected that its performance will decrease for any operating points different from the one used for the linearization.

Besides that, the MPC uses a prediction of the model behaviour to find the best long-term solution for the optimisation problem, whereas the LQR uses only the current state of the system. On the other hand, the MPC requires a much higher computational load and, for that reason, its use might not be feasible in some applications.

2.6 Sensors and Actuators

In this section, a description of the relevant sensors and actuators to perform orbital control is presented. The study is based on several existing missions and an evaluation of the most efficient hardware to use is also discussed. Since the goal of this thesis does not encompass attitude determination and control of the spacecraft, this section will only focus on the sensors and actuators that are related to aspects of spacecraft's translational motion.

2.6.1 Sensors

Accurate and frequent information about the position and the velocity of the spacecraft are key for autonomous orbital control. The position and velocity errors are used by the orbit controller to assess if corrections on the trajectory are needed. The requirements of the mission also determines the necessary accuracy for the position and velocity data and, therefore, which sensors to use.

Commonly, three different strategies are used to obtain the spacecraft's position and velocity: space-based tracking, ground-station tracking, and autonomous navigation systems. Space-based tracking systems are generally able to provide high accuracy navigation data at any desired update rate. They require a specific type of transponder on-board of the spacecraft, which has an impact on the cost of the mission, comprising both the acquisition costs and the indirect costs related to mass and power usage [27]. One example is the Tracking Data Relay Satellite System (TDRSS) launched by NASA in the early 1980s. The TDRSS space segment is currently composed of eight operational geosynchronous satellites, providing position determination with a 3σ accuracy of about 50 m [27]. On the other hand, ground-station tracking is only available when the spacecraft is visible to the ground tracking station. Even if a geographically distributed ground-station network is used, such as the space Surveillance Network, resource sharing and allocation constraints might limit the rate at which navigation data is obtained. This latter strategy also requires a transponder and telemetry equipment on-board the spacecraft. Finally, autonomous navigation systems utilise sensors on-board the spacecraft to determine its position and velocity in real-time. These sensors may require data transmitted from other satellites or ground-

stations (semi-autonomous), or be fully autonomous if no transmitted signals are needed.

A different approach, that does not require any on-board equipment and has no costs associated, consists of using the publicly available data from the US space Surveillance Network, which is provided in the form of two-line element (TLE) sets. However, this data is updated only twice a day and the accuracy is smaller than the obtained by transponder signals [27]. In fact, with the referred update rate, position accuracy is also dependent on the spacecraft's propagator accuracy. According to [28] and [29], for an orbit with an altitude of approximately 400 km and using TLEs and an accurate propagator such as SPG4, the cumulative position error after one day is around 1 km. This error magnitude might present some difficulties to specific missions that require higher position accuracy. In the case of orbit maintenance activities, adding to the problem the uncertainty associated with the propulsion system itself and its resulting acceleration on the satellite, the position error that arises might not satisfy the mission requirements. However, this error could still be acceptable for missions that do not require a high position accuracy to satisfy its requirements, reducing, that way, the complexity and the cost of the spacecraft. Therefore, the requirements of the mission must be well defined and an analysis should be performed to evaluate which strategy is the most suitable to achieve the objectives, considering a balance between the needed navigation data accuracy and update rate, as well as the cost and complexity of the system to be implemented.

A study through several missions related to this topic revealed that navigation data is usually obtained using autonomous navigation systems. One example is the Prisma mission, a formation flying mission that requires an accuracy of few tenths of meters. The two spacecraft of the formation were equipped with Phoenix GPS receivers for position and velocity measurements [30]. The US Navstar Global Positioning System, most commonly known as GPS, is a type of Global Navigation Satellite System (GNSS) consisting of 24 satellites (plus spares), in 6 orbital planes, with an orbital period of 12 hours. These GNSS constellations provide global coverage for LEO orbits and use signals from four or more satellites to compute the receiver's position vector [27]. Other GNSS constellations are the Russian GLONASS and the civilian-operated European Galileo. A different mission, of a larger satellite, is the TacSat-2. This satellite is equipped with an AZ IGOR Integrated GPS receiver, with an accuracy of few centimeters after ground-base post processing, to perform autonomous station-keeping activities [31].

In some specific cases, high accuracy for the orbit determination is required in order to achieve the mission objectives. For that, a Precise Orbit Determination (POD) method is used, which combines the data obtained by the GNSS measurements with ground-based data to achieve the required accuracy. This method was used in the TerraSAR-X mission, where the mission objectives required a position determination accuracy smaller than 5 cm.

In Table 2.3, five available GNSS receivers are presented, together with their main characteristics. Notice that a position accuracy of at least 10 m can be obtained and more accurate systems can achieve values as small as 1 m. However, if the mission requires higher accuracy, ground-based post processing can reduce these values to few centimeters. The refereed accuracy values correspond to 3σ of a Gaussian distribution.

Table 2.3: Commercial GNSS receivers and properties. The presented accuracy values correspond to 3σ of a Gaussian distribution.

Name	GNSS type	Mass	Pos. accuracy	Vel. accuracy	Power
Phoenix [32]	GPS	20 g	10 m	0.1 m/s	0.85 W
ISIS GNSS [33]	GPS+GALILEO	20 g	10 m	0.01 m/s	0.45 W
NGPS-03-422 [34]	GPS	130 g	10 m	0.05 m/s	1 W
NavSBR [35]	GPS	2300 g	1 m	0.02 m/s	12 W
PODRIX [36]	GPS+GALILEO	3000 g	1 m	0.002 m/s	15 W
AZ IGOR [37]	GPS	4600 g	1 m	0.012 m/s	16 W

2.6.2 Actuators

To perform orbital control activities, acceleration must be applied to the spacecraft center of mass in order to achieve a change on the velocity vector. A propulsion system is then needed to provide the spacecraft with the impulse per unit of spacecraft mass, denoted by Δv and measured in m/s. In this section, an introduction to space propulsion and the different types of thrusters is presented, as well as a discussion of the advantages and disadvantages of each type.

The Rocket Equation and Specific Impulse

Assuming a spacecraft in orbit and neglecting all forces acting on the vehicle but the trust provided by the thrusters, it is possible to write (see [20])

$$\dot{v} = \frac{g_0 I_{sp}}{M}\dot{M}, \tag{2.13}$$

where $\dot{v}$ is the spacecraft's acceleration, $g_0 = 9.80665$ m/s^2 is Earth's standard gravitational acceleration at sea level, $\dot{M}$ is the mass flow rate expelled by the nozzle, and I_{sp} is defined as the specific impulse, given by

$$I_{sp} = \frac{T_t}{\dot{M} g_0},$$

where T_t is the thrust produced by the spacecraft's thrusters. The specific impulse is computed as the ratio of the thrust produced to the weight flow of the propellants. In other words, it is the time duration, given in units of time, that a given quantity of propellant is able to generate a thrust equal to the propellant's initial weight [20].

With some algebraic manipulation, (2.13) can be integrated yielding

$$\Delta v = g_0 I_{sp} \ln \frac{M_0}{M_f}, \tag{2.14}$$

where M_0 and M_f are, respectively, the initial and final masses of the spacecraft before and after the propulsive burn. Equation (2.14) is commonly known as the Ideal Rocket Equation or Tsiolkovsky Equation [27] and it can be used to estimate the maximum velocity increment, Δv, that is possible to obtain for

a certain propellant mass burn $M_0 - M_f$, given an engine-propellant combination with a characteristic specific impulse, I_{sp}. A consequence of (2.14) is that, given a certain propellant mass, the propulsive velocity increment is maximised by using a thruster with the highest possible specific impulse. In other words, a thruster with a higher specific impulse will require less propellant mass to achieve a certain velocity increment. Therefore, specific impulse can be interpreted as an efficiency parameter to characterise a thruster [20].

Types of Thrusters

In this section, a brief description of the different types of thrusters is presented. The principal propulsion technologies are cold gas, chemical, and electrical.

Cold Gas Thrusters Cold gas thrusters are the simplest form of propulsion. These thrusters are based on a controlled and pressurised gas source expelled through a nozzle, without combustion. This type of propulsion is characterised by small specific impulses despite being cheaper and have a simpler implementation than the other alternatives [27].

Chemical Thrusters In this type of thrusters, the gases resulting from the combustion of the propellants are redirected through the nozzle. Three different types of chemical thrusters are available, depending on the initial state of the stored propellants, with important changes in the internal architecture of the thrusters (see [27]):

- Liquid propellant systems – These systems use liquid propellants that are fed to the combustion chamber using a pump or by gas pressurisation. Depending on the number of propellant components, these thrusters can be defined as monopropellant, if only one propellant is used, or bipropellant, if two propellants are used, usually a fuel and an oxidiser that chemically react in a combustion process. Monopropellant systems are simpler and, therefore, more reliable but, on the other hand, bi-propellant systems can provide higher specific impulses;
- Solid propellant systems – In this case, the propellant is stored in solid form. These thrusters have lower performance than liquid ones but they are simpler and require less storage room since they have a higher density. The main limitation of these thrusters is that, once combustion of the propellant is established, there is no mechanism to stop it. For this reason, they cannot be used in missions with multiple starts;
- Hybrid propellant systems – This type of system is not very common and, as the name indicates, they have the propellants in different states. Usually, the fuel is solid and the oxidiser is a liquid or a gas.

Electric Propulsion Electric propulsion makes use of electrical power to accelerate a propellant that is responsible for the creation of thrust once the fluid is expelled. It is, therefore, limited by the available electrical power on-board the spacecraft. Depending on the way that electrical power is used

to create this thrust, it is possible to establish three main classes of electric propulsion systems: electrothermal, if the propellant is electrically heated and then expanded through a nozzle; electrostatic, where electric fields are used to accelerate charged particles; and electromagnetic, if the force on the charged particles is produced by their interaction with the magnetic field generated electrically. The propellant used in these thrusters depends on its type and can be a rare gas, like xenon or argon, a liquid metal, or, in some cases, a conventional propellant [27].

Comparison between the different types of thrusters

An evaluation of the most suitable propulsion method and thrusters to use should consider mission requirements and the impact of this system on the rest of the spacecraft. For example, in terms of power consumption, it will be low unless the system used requires a heated propellant or it is an electric thruster. Also, it must be taken into consideration the impact that the propulsion system, including thrusters, storage tanks and propellants, have on the mass budget. Finally, from a thermal perspective, it will depend on the type of thruster used but, in principle, it is possible to admit that heaters may be required to prevent the propellant and the lines from freezing [27]. The propulsion methods addressed in Section 2.6.2 are summarised in Table 2.4, with typical specific impulses and possible usage.

Table 2.4: Principal options for spacecraft propulsion systems [27].

Propulsion technology	Orbit Control	Attitude Control	Typical $I_{sp}(s)$
Cold gas	X	X	30-70
Solid			280-300
Liquid: monopropellant	X	X	220-240
Liquid: bi-propellant	X	X	305-310
Hybrid	X		250-340
Electric	X	X	250-3000

Despite being less expensive and simpler to implement, cold gas propulsion systems present low performance due to a small typical specific impulse. Notice that the use of solid propulsion is almost limited to launchers and is not used neither for orbit control nor for attitude control since these propulsion systems can only be used once during the mission. A widely used type of spacecraft propulsion relies on monopropellant hydrazine since it is simple to implement and reliable, despite its lower efficiency when compared to other propulsion options [27]. A different monopropellant propulsion system was used on the Prisma formation flying mission, where High Performance Green Propulsion was used. This type of propulsion presents several advantages relatively to hydrazine, namely its higher specific impulse, higher propellant density and reduced cost [30]. Regarding electric propulsion systems, several advantages are mentioned in [38], namely higher specific impulse systems, capable of operating high variations of thrust, and also providing accurate compliance with the thrust required. On the other hand, since space power systems only put out small amounts of power, the amount of thrust electric engines produce is very small when compared to chemical engines. Therefore, electric propulsion is suitable

for low-thrust, long-duration applications on-board spacecraft [39]. Since orbit maintenance maneuvers typically require small amounts of thrust and are performed numerous times during mission lifetime [27], electric propulsion shall be taken into consideration as a viable strategy to perform these maneuvers. One example of this usage is the TacSat-2 mission, which used Hall effect thrusters, a type of electric propulsion system, to perform orbit maintenance activities [31]. Other examples of electric propulsion systems are presented in Table 2.5, along with several main parameters. It is possible to notice that, depending on the technology used, these different types of electric propulsion present major differences in the power requirements, specific impulse, efficiency, and thrust provided, so a meticulous evaluation shall be carried in order to choose the best propulsion system to fulfill the mission requirements [27].

Table 2.5: Main characteristics of electric propulsion systems [27].

Class	Technology	Power	Typical I_{sp}(s)	Efficiency	Thrust
Electrothermal	Resistojet	0.5-1.5 kW	250	80%	0.1-0.5 N
Electrothermal	Arcjet	0.3-100 kW	500-2000	35%	0.2-2 N
Electrostatic	Ion	0.5-2.5 kW	3000	60%-80%	10-200 mN
Electrostatic	Hall	1.5-5 kW	1500-2000	50%	80-200 mN
Electromagnetic	MPD	1-4000 kW	2000-5000	25%	1-200 N
Electromagnetic	VASIMR	1-10 MW	3000-30000	20%-60%	1-2 kN

In Table 2.6 some examples of cold gas, chemical, and electric thrusters are presented, together with their main characteristics. Notice the difference in nominal thrust and specific impulse between the different propulsion technologies.

Table 2.6: Commercial thrusters and properties.

Model	Propulsion Technology	Nominal Thrust	I_{sp}	Mass
Moog 058E142A [40]	Cold gas	120 mN	57 s	16 g
Moog 058-118 [40]	Cold gas	3.6 N	56 s	23 g
Ariane EM007 [41]	Monopropellant	1 N	220 s	290 g
MONARC-5 [42]	Monopropellant	4.5 N	226.1 s	490 g
Dawn bi-propellant [43]	Bi-propellant	0.5 N	285 s	170 g
Moog DST-12 [44]	Bi-propellant	22 N	302 s	640 g
BUSEK BIT-3 [45]	Ion	1.25 mN	2300 s	1.4 kg
Ariane Rit 10 EVO [46]	Ion	15 mN	3000 s	1.8 kg
Ariane Rit 2X [46]	Ion	215 mN	2750 s	10 kg
BUSEK Resistojet [47]	Resistojet	10 mN	150 s	1.25 kg
BUSEK BHT-200 [48]	Hall	13 mN	1390 s	980 g
BUSEK BHT-8000 [49]	Hall	450 mN	2210 s	25 kg

Chapter 3

Problem Statement

This thesis is focused on the development of an autonomous orbit controller for a low-Earth orbit spacecraft. The TerraSAR-X mission, which was operated in close formation with the Tandem-X mission at distances of a few hundred meters, is used in this thesis as a test-bed for the proposed controllers, given its demanding orbit control requirements.

3.1 TerraSAR-X Mission

TerraSAR-X is a German synthetic-aperture radar (SAR) satellite based on a public-private partnership agreement between the German Aerospace Center (DLR) and EADS Astrium GmbH, which was launched on 15^{th} June, 2007. The science objectives of the mission are to make multi-mode and high-resolution X-band SAR data available for a large variety of applications in scientific fields such as hydrology, geology, climatology, oceanography, environmental and disaster monitoring, and cartography, making use of interferometry and stereometry [50].

The spacecraft characteristics and orbit properties of the TerraSAR-X mission are presented in Table 3.1. The orbit of TerraSAR-X is LEO, sun-synchronous and has to fulfill the requirements presented in Table 3.2 to accomplish its mission.

Table 3.1: Spacecraft and orbit properties of the TerraSAR-X mission, where S/C stands for spacecraft [10].

TerraSAR-X characteristics	
S/C wet mass	1230 kg
S/C dimensions	5 m height $\times$ 2.4 m diameter
Semi-major axis	6892.944 km
Eccentricity	0.0014252
Inclination	97.4401 deg
Altitude	$505 - 533$ km
Nominal revisit period	11 days

Table 3.2: TerraSAR-X mission requirements [10].

TerraSAR-X requirements	
Local time of ascending node	$18:00$ hrs ($\pm$ 0.25 hrs)
Ground track repeatability	$\pm$ 500 m per revisit period

The local time of ascending node (LTAN) is used to describe sun-synchronous orbits. This type of orbits is often used by Earth observation missions, which require that their observations are obtained at the same local mean solar time. It is defined by the mean local time at which the spacecraft passes the Earth equator on the ascending branch of its orbit. LTAN values of 6:00 hrs and 18:00 hrs represent sunrise and sunset, respectively, and, in this case, the vector from the centre of the Earth to the ascending node is perpendicular to the projection of the vector that points from the Earth to the Sun on the equatorial plane. On the other hand, LTAN values of 00:00 hrs and 12:00 hrs represent midnight and noon, respectively, in which case the vector from the centre of the Earth to the ascending node is parallel to the projection of the vector that points from the Earth to the Sun on the equatorial plane.

The ground track repeatability defines with which accuracy the spacecraft should fly over a given path on the Earth's surface. The ground track repeatability is evaluated by the ground track repeatability error, which is the distance along the Earth surface between the satellite real position and its desired location. The controller designed shall actuate on the satellite in order to maintain this parameter within the allowed values (in this case $\pm$ 500 m per revisit period).

In this mission, the orbit perturbations due to the Earth gravity field are not corrected by the orbit control system, so that the orbital precession due to the oblateness of the Earth can be leveraged to keep the LTAN constant. For the LTAN to be constant, the drift rate of the longitude of the ascending node (orbital precession) needs to match the angular velocity of the Earth's orbit around the Sun. Other perturbations such as the atmospheric drag, the third-body gravity attraction, and the solar radiation pressure, that cause an error on the ground track repeatability, should be corrected.

3.2 Ground Track Repeatability Error

One of the main control objectives of the mission presented in Section 3.1, with particular emphasis in this thesis, is to maintain the projection of the real satellite on the Earth's surface within the allowed values during the entire mission. As stated in Section 1.3, this problem can be formulated as a two satellite formation problem, in which one of them is virtual and not affected by non-gravitational orbit perturbations. This virtual satellite is referred to as the reference satellite.

The ground track repeatability error (T_r), illustrated in Fig. 3.1, is a key mission requirement and it can be represented, at a given epoch, as the distance along the Earth surface between the real propagated satellite at point A and the reference satellite at point B. The reference satellite complies with the mission requirements, having an error of zero in the ground track repeatability at all times.

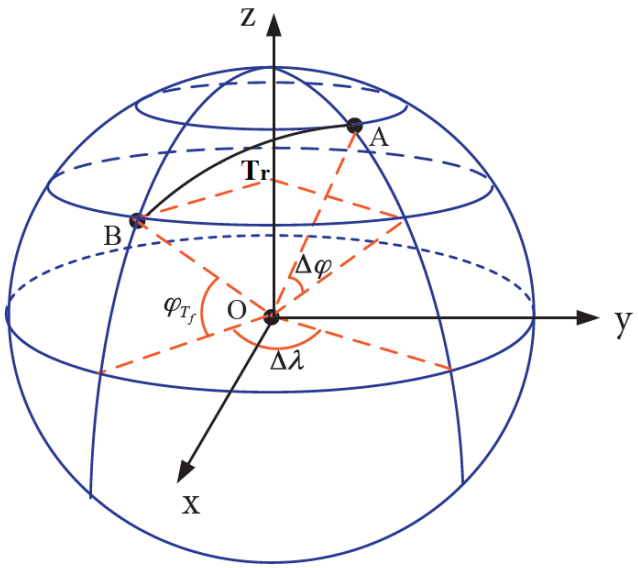

Figure 3.1: Ground track repeatability error schematic diagram [51].

The approximate formula for small values of T_r based on spherical geometry is given by (see [51])

$$T_r \approx R_{\oplus}\sqrt{\Delta\varphi^2 + (\cos\varphi_{T_f}\Delta\lambda)^2}, \tag{3.1}$$

where φ_{T_f} is the geocentric latitude of point B, and $\Delta\varphi$ and $\Delta\lambda$ are the geocentric latitude and longitude difference between points A and B, respectively.

Figure 3.2 presents the obtained ground track repeatability error for the TerraSAR-X satellite using this methodology and if no control actions are performed. Notice that, approximately after 3.8×10^4 s (approximately 7 complete orbits around the Earth), the ground track repeatability error exceeds the allowed value of 500 m, due to the influence of perturbation forces that affect the real satellite. Therefore, the controller is expected to perform control actions that prevent this value to be exceeded.

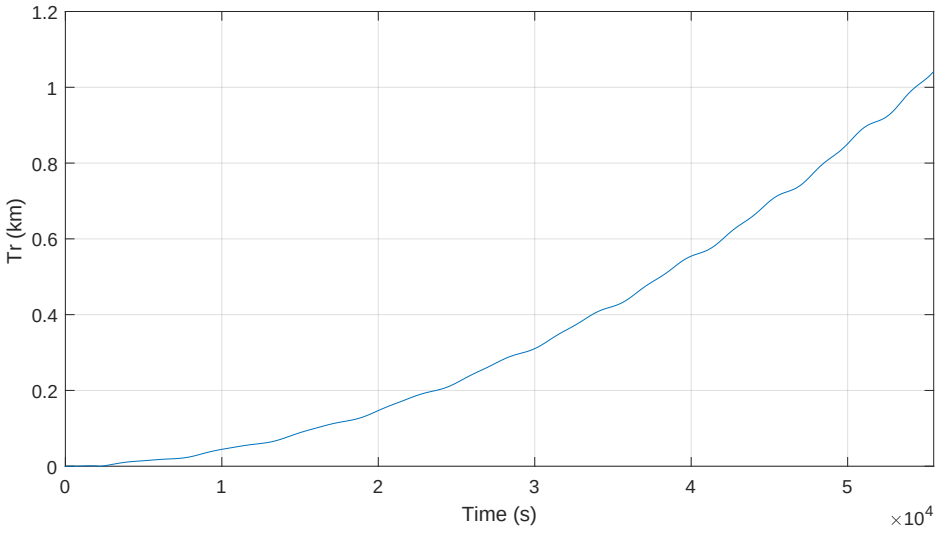

Figure 3.2: TerraSAR-X ground track repeatability error.

As mentioned in Section 3.1, the orbit precession due to the Earth gravity field should not be corrected by the orbit control system. For that reason, the reference orbit to be used should not be completely unperturbed. Actually, it should be affected by the aspherical terms of the Earth gravity field. However, other perturbation forces that affect the real orbit shall be corrected, namely the atmospheric drag, the solar radiation pressure, and the third-body gravitational attraction.

Chapter 4

Control Design

The control strategy is projected to maintain the orbit of the TerraSAR-X within the range of values specified by the mission requirements. This chapter presents the design of the control algorithm to achieve this objective and describes the strategy to implement the LQR (Section 4.2) and the MPC (Section 4.3). The final control solution, which combines 2 LQR and 2 MPC, is introduced in Section 4.4.

4.1 Overview

The mission described in Section 3 requires that the ground track repeatability error is maintained within a specific range of values to fulfill the mission objectives. Recalling (3.1), the ground track repeatability error is given by the position difference along the Earth surface between the real spacecraft and the reference. Therefore, the projection on the Earth surface of the position of the real satellite should be driven and maintained close to the projection on the Earth of the reference satellite, so the ground track repeatability error is small enough. This is possible if the orbital position of the real satellite is driven to the reference satellite orbital position, considering that the projection of the satellite is directly dependent on its orbital position. Furthermore, by correcting the orbital velocity of the real satellite, its orbit will converge to the reference satellite orbit. This strategy will also maintain the LTAN within the range of values specified by the requirements since this is a property of the reference orbit, which is designed in a way that all mission requirements are met.

To achieve this objective, two different control strategies are considered: LQR (see Section 2.5.1) and MPC (see Section 2.5.2). The motivation to use these two different strategies is to compare the performance of a simple control methodology, such as the LQR, with a more complex methodology, such as MPC. The LQR only uses the current state of the system to compute the next control action and does not take into account the existence of system and actuators constraints for that computation. On the other hand, the MPC uses the prediction of the system behaviour for an optimisation process that accounts for system and actuators constraints to compute a vector of control actions to guide the state of the system to the reference. The control design based on these two strategies is described in this chapter.

4.2 LQR Design

4.2.1 Dynamic Model

To design a linear quadratic regulator that maintains the ground track repeatability error within the allowed values, the dynamic model of the system must be expressed in the form $\dot{\mathbf{x}} = \mathbf{A}_{LQR}\mathbf{x} + \mathbf{B}_{LQR}\mathbf{u}$, as described in Section 2.5.1. Notice that this dynamic model must be linear, with $\mathbf{A}_{LQR}$ and $\mathbf{B}_{LQR}$ independent of $\mathbf{x}$. The Cartesian representation, in the ToD reference frame, of the error dynamics between the real satellite and the reference is a straightforward model that simplifies the controller implementation. This controller is designed to drive and maintain the difference between the orbital position and velocity of the real and the reference spacecraft close to zero.

Using the Cartesian coordinates representation for the orbital motion laws (see Section 2.2.1), it is possible to write

$$\begin{cases} \dot{\mathbf{r}} &= \mathbf{v} \\ \dot{\mathbf{v}} &= -\frac{\mu}{||\mathbf{r}||^3}\mathbf{r} + {}^{I}\mathbf{f}(\mathbf{r},\mathbf{v}) + {}^{I}\mathbf{f}_c \end{cases}, \tag{4.1}$$

where ${}^{I}\mathbf{f}(\mathbf{r},\mathbf{v})$ is a 3×1 vector that corresponds to an acceleration vector caused by orbital perturbations and ${}^{I}\mathbf{f}_c$ is a 3×1 vector that corresponds to a control acceleration, expressed in the ToD reference frame, used to control the satellite motion. Let ${}^{I}\mathbf{x} = [\mathbf{r}^T\ \mathbf{v}^T]^T$ be the vector that contains the position and the velocity of the real satellite expressed in the ToD reference frame. Recalling (4.1), the time derivative of vector ${}^{I}\mathbf{x}$ can be written as

$${}^{I}\dot{\mathbf{x}} = \mathbf{a}({}^{I}\mathbf{x}) + \mathbf{B}\ {}^{I}\mathbf{f}_c, \tag{4.2}$$

where

$$\mathbf{a}({}^{I}\mathbf{x}) = \begin{bmatrix} \mathbf{v} \\ -\frac{\mu}{||\mathbf{r}||^3}\mathbf{r} + {}^{I}\mathbf{f}(\mathbf{r},\mathbf{v}) \end{bmatrix}$$

and

$$\mathbf{B} = \begin{bmatrix} 0 & 0 & 0 \\ 0 & 0 & 0 \\ 0 & 0 & 0 \\ 1 & 0 & 0 \\ 0 & 1 & 0 \\ 0 & 0 & 1 \end{bmatrix},$$

where $\mathbf{a}({}^{I}\mathbf{x})$ is a 6×1 vector that includes the acceleration caused by the central body and perturbation forces acting on the system, and $\mathbf{B}$ is a 6×3 matrix that represents the influence of the control acceleration, ${}^{I}\mathbf{f}_c$, on the system. As mentioned in Section 3.1, it is intended that the orbit precession still

occurs in order to maintain the LTAN constant. Therefore, for the reference orbit, the only perturbative acceleration that is considered is the one caused by the Earth's gravity field and no input accelerations are considered. This orbit is modelled by

$$ {}^{I}\dot{\mathbf{x}}_r = \begin{bmatrix} \mathbf{v}_r \\ -\frac{\mu}{||\mathbf{r}_r||^3}\mathbf{r}_r + {}^{I}\mathbf{f}_r(\mathbf{r}_r, \mathbf{v}_r) \end{bmatrix}, \tag{4.3} $$

where ${}^{I}\mathbf{x}_r = [\mathbf{r}_r^T \ \mathbf{v}_r^T]^T$ is a vector that contains the position and the velocity of the reference satellite in the ToD reference frame and ${}^{I}\mathbf{f}_r(\mathbf{r}_r, \mathbf{v}_r)$ is a perturbative acceleration caused by the Earth's gravity field. To obtain a ground track error close to zero, the controller objective is to drive the difference of the position and the velocity between the real and the reference satellite to zero. In other words, the error $\boldsymbol{\epsilon} = {}^{I}\mathbf{x} - {}^{I}\mathbf{x}_r$ must converge to zero. Subtracting (4.3) from (4.2), the dynamic model in matrix form for the error between the real and the reference satellite is given by

$$ \dot{\boldsymbol{\epsilon}} = \begin{bmatrix} \mathbf{v} - \mathbf{v}_r \\ -\frac{\mu}{||\mathbf{r}||^3}\mathbf{r} + {}^{I}\mathbf{f}(\mathbf{r}, \mathbf{v}) + \frac{\mu}{||\mathbf{r}_r||^3}\mathbf{r}_r - {}^{I}\mathbf{f}_r(\mathbf{r}_r, \mathbf{v}_r) \end{bmatrix} + \mathbf{B}{}^{I}\mathbf{f}_c. \tag{4.4} $$

Defining $\Delta\mathbf{v} = \mathbf{v} - \mathbf{v}_r$ and $\Delta\mathbf{r} = \mathbf{r} - \mathbf{r}_r$, it is possible to rewrite (4.4) as

$$ \dot{\boldsymbol{\epsilon}} = \begin{bmatrix} \Delta\mathbf{v} \\ -\frac{\mu}{||\Delta\mathbf{r}+\mathbf{r}_r||^3}(\Delta\mathbf{r} + \mathbf{r}_r) + \frac{\mu}{||\mathbf{r}_r||^3}\mathbf{r}_r + {}^{I}\mathbf{f}(\Delta\mathbf{r} + \mathbf{r}_r, \Delta\mathbf{v} + \mathbf{v}_r) - {}^{I}\mathbf{f}_r(\mathbf{r}_r, \mathbf{v}_r) \end{bmatrix} + \mathbf{B}{}^{I}\mathbf{f}_c. \tag{4.5} $$

The dynamic model for the error between the real and the reference satellite is given by (4.5). Notice that this model is nonlinear and, therefore, to implement an LQR controller based on this system dynamics, a linearization process must be carried out.

4.2.2 Linearization

As referred to in Section 4.2.1, the system dynamics modelled by (4.5) is nonlinear, since it is not possible to write it in the form $\dot{\boldsymbol{\epsilon}} = \mathbf{A}_\epsilon\boldsymbol{\epsilon} + \mathbf{B}_\epsilon{}^{I}\mathbf{f}_c$, where $\mathbf{A}_\epsilon$ and $\mathbf{B}_\epsilon$ are independent of the system state, $\boldsymbol{\epsilon}$. Therefore, in order to apply the LQR control methodology, a linearization process is performed. This method consists in finding the linear approximation of a nonlinear function at a given equilibrium point, which is a constant state solution of the system in the sense that the dynamics imposed by the equation keep the state constant. The linear approximation of a function is obtained from the first-order term of the Taylor expansion around the operating point and is valid in a small region around this point. Operations near the equilibrium point take the form of small perturbations, which are sufficiently small variations about the equilibrium point such that the state evolves back to the rest point [52]. Using this methodology, it is possible to obtain the linearized dynamics of (4.5) to be used in the implementation of the LQR controller. Notice that the first row of (4.5) is already linear.

Starting by defining an equilibrium point given by $\Delta\mathbf{r}_0 = \Delta\mathbf{v}_0 = [0\ 0\ 0]^T$ and ${}^{I}\mathbf{f}_{c_0} = [0\ 0\ 0]^T$, which, by the definition of equilibrium point, provides $\dot{\boldsymbol{\epsilon}}_0 = [0\ 0\ 0\ 0\ 0\ 0]^T$, the small perturbation model for operations near this equilibrium point is given by

$$
\begin{cases}
\Delta r_1 = \Delta r_{1_0} + \delta\Delta r_1 \\
\Delta r_2 = \Delta r_{2_0} + \delta\Delta r_2 \\
\Delta r_3 = \Delta r_{3_0} + \delta\Delta r_3 \\
\Delta v_1 = \Delta v_{1_0} + \delta\Delta v_1 \\
\Delta v_2 = \Delta v_{2_0} + \delta\Delta v_2 \\
\Delta v_3 = \Delta v_{3_0} + \delta\Delta v_3 \\
{}^I\mathbf{f}_c = {}^I\mathbf{f}_{c_0} + \delta{}^I\mathbf{f}_c
\end{cases} . \tag{4.6}
$$

Note that $\Delta\mathbf{r} = [\Delta r_1\ \Delta r_2\ \Delta r_3]^T$, $\Delta\mathbf{v} = [\Delta v_1\ \Delta v_2\ \Delta v_3]^T$, and $\mathbf{r}_r = [r_{r_1}\ r_{r_2}\ r_{r_3}]^T$, which are expressed in the ToD reference frame. The referred equilibrium point was chosen based on the control objective of driving the error between the real and the reference satellite to zero. Therefore, it was decided to linearize (4.5) about the equilibrium point where the error is zero, given by $\boldsymbol{\epsilon} = [0\,0\,0\,0\,0\,0]^T \Rightarrow \Delta\mathbf{r} = \Delta\mathbf{v} = [0\,0\,0]^T$. Remembering that $\boldsymbol{\epsilon} = [\Delta\mathbf{r}^T\ \Delta\mathbf{v}^T]^T$ and defining the nonlinear row (second row) of (4.5) as

$$
g(\boldsymbol{\epsilon}) = -\frac{\mu}{||\Delta\mathbf{r} + \mathbf{r}_r||^3}(\Delta\mathbf{r} + \mathbf{r}_r) + \frac{\mu}{||\mathbf{r}_r||^3}\mathbf{r}_r + {}^I\mathbf{f}(\Delta\mathbf{r} + \mathbf{r}_r, \Delta\mathbf{v} + \mathbf{v}_r) - {}^I\mathbf{f}_r(\mathbf{r}_r, \mathbf{v}_r),
$$

it is possible to write $g(\boldsymbol{\epsilon})$ as the Taylor series expansion

$$
\begin{aligned}
g(\boldsymbol{\epsilon}) = \cancelto{0}{g(\boldsymbol{\epsilon}_{I_0})} &+ \frac{\partial g(\boldsymbol{\epsilon})}{\partial\Delta r_1}\Big|_{\boldsymbol{\epsilon}=0}\delta\Delta r_1 + \frac{\partial g(\boldsymbol{\epsilon})}{\partial\Delta r_2}\Big|_{\boldsymbol{\epsilon}=0}\delta\Delta r_2 + \frac{\partial g(\boldsymbol{\epsilon})}{\partial\Delta r_3}\Big|_{\boldsymbol{\epsilon}=0}\delta\Delta r_3 + \\
&\frac{\partial g(\boldsymbol{\epsilon})}{\partial\Delta v_1}\Big|_{\boldsymbol{\epsilon}=0}\delta\Delta v_1 + \frac{\partial g(\boldsymbol{\epsilon})}{\partial\Delta v_2}\Big|_{\boldsymbol{\epsilon}=0}\delta\Delta v_2 + \frac{\partial g(\boldsymbol{\epsilon})}{\partial\Delta v_3}\Big|_{\boldsymbol{\epsilon}=0}\delta\Delta v_3 + h.o.t.
\end{aligned} \tag{4.7}
$$

Since the magnitude of the perturbative acceleration caused by the J_2 Earth gravity component is 10^3 times higher than the magnitude of other perturbative accelerations that affect the real orbit, for the sake of simplicity, it was decided to only consider the J_2 term influence in the system. Neglecting higher-order terms, the partial derivatives of (4.7) evaluated at $\boldsymbol{\epsilon} = \mathbf{0}$ are given by

$$
\begin{aligned}
\frac{\partial g(\boldsymbol{\epsilon})}{\partial\Delta r_1}\Big|_{\boldsymbol{\epsilon}=0} = \frac{3\mu r_{r_1}}{||\mathbf{r}_r||^5}\mathbf{r}_r - \frac{\mu}{||\mathbf{r}_r||^3}\begin{bmatrix}1\\0\\0\end{bmatrix} + \\
J_2\mu R_\oplus^2\begin{bmatrix}
-\frac{3\left(1-\frac{5r_{r_3}^2}{||\mathbf{r}_r||^2}\right)}{2||\mathbf{r}_r||^5} + \frac{15r_{r_1}^2\left(1-\frac{5r_{r_3}^2}{||\mathbf{r}_r||^2}\right)}{2||\mathbf{r}_r||^7} - \frac{15r_{r_3}^2 r_{r_1}^2}{||\mathbf{r}_r||^9} \\
\frac{15r_{r_1}r_{r_2}\left(-6r_{r_3}^2 + r_{r_2}^2 + r_{r_1}^2\right)}{2||\mathbf{r}_r||^9} \\
\frac{15r_{r_3}r_{r_1}\left(-4r_{r_3}^2 + 3r_{r_2}^2 + 3r_{r_1}^2\right)}{2||\mathbf{r}_r||^9}
\end{bmatrix},
\end{aligned}
$$

$$\frac{\partial g(\boldsymbol{\epsilon})}{\partial \Delta r_2}\Big|_{\boldsymbol{\epsilon}=0} = \frac{3\mu r_{r_2}}{||\mathbf{r}_r||^5}\mathbf{r}_r - \frac{\mu}{||\mathbf{r}_r||^3}\begin{bmatrix}0\\1\\0\end{bmatrix} + J_2\mu R_\oplus^2 \begin{bmatrix} \dfrac{15r_{r_1}r_{r_2}\left(-6r_{r_3}^2 + r_{r_2}^2 + r_{r_1}^2\right)}{2||\mathbf{r}_r||^9} \\ -\dfrac{3\left(1-\frac{5r_{r_3}^2}{||\mathbf{r}_r||^2}\right)}{2||\mathbf{r}_r||^5} + \dfrac{15r_{r_2}^2\left(1-\frac{5r_{r_3}^2}{||\mathbf{r}_r||^2}\right)}{2||\mathbf{r}_r||^7} - \dfrac{15r_{r_3}^2 r_{r_2}^2}{||\mathbf{r}_r||^9} \\ \dfrac{15r_{r_3}r_{r_2}\left(-4r_{r_3}^2 + 3r_{r_2}^2 + 3r_{r_1}^2\right)}{2||\mathbf{r}_r||^9} \end{bmatrix},$$

$$\frac{\partial g(\boldsymbol{\epsilon})}{\partial \Delta r_3}\Big|_{\boldsymbol{\epsilon}=0} = \frac{3\mu r_{r_3}}{||\mathbf{r}_r||^5}\mathbf{r}_r - \frac{\mu}{||\mathbf{r}_r||^3}\begin{bmatrix}0\\0\\1\end{bmatrix} + J_2\mu R_\oplus^2 \begin{bmatrix} -\dfrac{15r_{r_3}r_{r_1}\left(-4r_{r_3}^2 + 3r_{r_2}^2 + 3r_{r_1}^2\right)}{2\left(r_{r_3}^2 + r_{r_2}^2 + r_{r_1}^2\right)||\mathbf{r}_r||^7} \\ -\dfrac{15r_{r_3}r_{r_2}\left(-4r_{r_3}^2 + 3r_{r_2}^2 + 3r_{r_1}^2\right)}{2\left(r_{r_3}^2 + r_{r_2}^2 + r_{r_1}^2\right)||\mathbf{r}_r||^7} \\ -\dfrac{3\left(3-\frac{5r_{Ir_3}^2}{||\mathbf{r}_r||^2}\right)}{2||\mathbf{r}_r||^5} + \dfrac{15r_{r_3}^2\left(3-\frac{5r_{r_3}^2}{||\mathbf{r}_r||^2}\right)}{2||\mathbf{r}_r||^7} - \dfrac{3r_{r_3}\left(\frac{10r_{Ir_3}^3}{||\mathbf{r}_r||^4} - \frac{10r_{r_3}}{||\mathbf{r}_{Ir}||^2}\right)}{2||\mathbf{r}_r||^5} \end{bmatrix},$$

$$\frac{\partial g(\boldsymbol{\epsilon})}{\partial \Delta v_1}\Big|_{\boldsymbol{\epsilon}=0} = \frac{\partial g(\boldsymbol{\epsilon})}{\partial \Delta v_2}\Big|_{\boldsymbol{\epsilon}=0} = \frac{\partial g(\boldsymbol{\epsilon})}{\partial \Delta v_3}\Big|_{\boldsymbol{\epsilon}=0} = 0.$$

The Taylor series expansion (4.7) provides a linear form of $g(\boldsymbol{\epsilon})$. With that in mind, and using the small perturbation model given by (4.6), it is possible to linearize the error dynamics (4.5), as given by

$$\delta\dot{\boldsymbol{\epsilon}} = \mathbf{A}_\epsilon \delta\boldsymbol{\epsilon} + \mathbf{B}_\epsilon \delta^I \mathbf{f}_c, \tag{4.8}$$

where

$$\mathbf{A}_\epsilon \delta\boldsymbol{\epsilon} = \begin{bmatrix} \delta\Delta\mathbf{v} \\ \frac{\partial g(\boldsymbol{\epsilon})}{\partial \Delta r_1}\Big|_{\boldsymbol{\epsilon}=0}\delta\Delta r_1 + \frac{\partial g(\boldsymbol{\epsilon})}{\partial \Delta r_2}\Big|_{\boldsymbol{\epsilon}=0}\delta\Delta r_2 + \frac{\partial g(\boldsymbol{\epsilon})}{\partial \Delta r_3}\Big|_{\boldsymbol{\epsilon}=0}\delta\Delta r_3 \end{bmatrix}$$

and

$$\mathbf{B}_\epsilon = \begin{bmatrix} 0 & 0 & 0 \\ 0 & 0 & 0 \\ 0 & 0 & 0 \\ 1 & 0 & 0 \\ 0 & 1 & 0 \\ 0 & 0 & 1 \end{bmatrix}.$$

The linearized dynamics for the error between the real and the reference satellite given by (4.8) operates around the equilibrium point where the error is zero and uses the deviations from this equilibrium,

$\delta\boldsymbol{\epsilon} = [\delta\Delta\mathbf{r}^T \ \delta\Delta\mathbf{v}^T]^T$, as the system state. For operating points far from zero, the linearized model is no longer valid. However, for operations near the equilibrium point, these linearized dynamics can be used for the implementation of the LQR controller.

4.2.3 LQR Synthesis

In order to assess the LQR performance, a MATLAB script was developed using the propagation model validated in Section 2.4. It is intended to evaluate the effect that the control input computed by the controller has on the system and assess its performance in driving the error between the real satellite and the reference to zero. A schematic representation of the MATLAB script is presented in Fig. 4.1. As presented, two satellites with the same physical characteristics as the TerraSAR-X spacecraft are defined:

- Reference satellite - This satellite has initial orbital parameters in accordance with the mission requirements and is only affected by the orbital perturbation caused by the Earth gravity field;
- Real satellite - It is possible to define an initial orbital error for this satellite in any of its orbital elements. Furthermore, this satellite orbit is affected by the orbital perturbations caused by the Earth gravity field, the solar radiation pressure, the atmospheric drag, the third-body gravitational attraction, and by the control action computed by the controller.

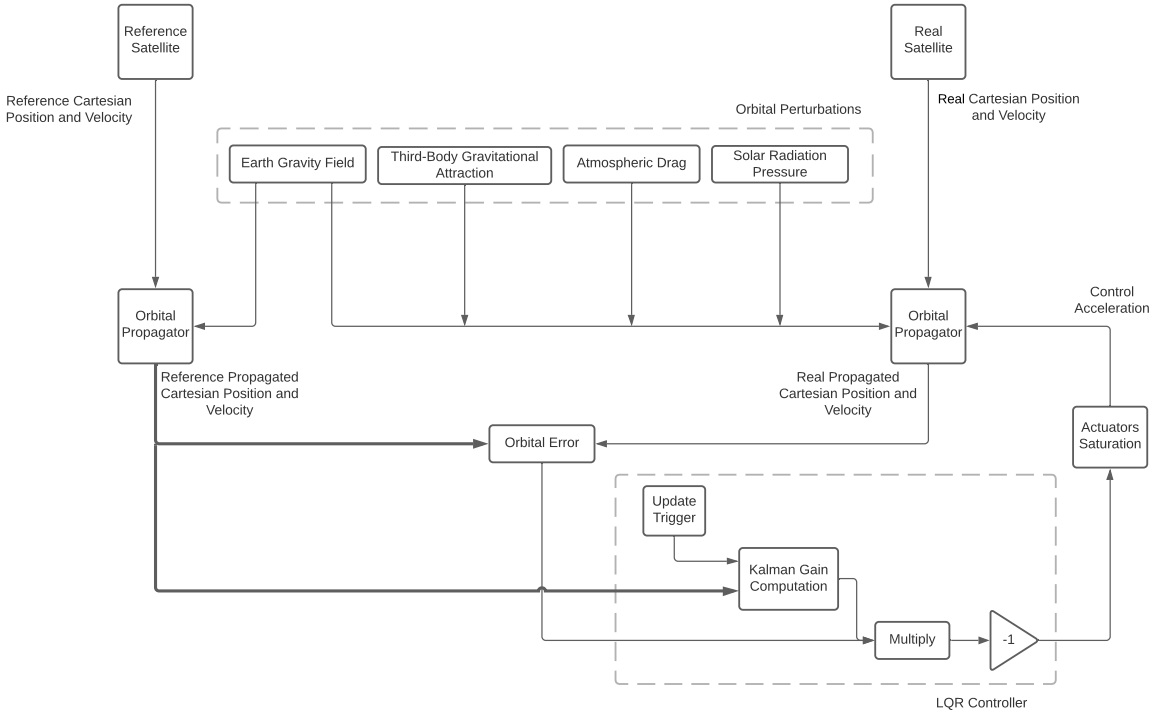

Figure 4.1: LQR implementation scheme.

The control input computed by the LQR controller takes the form of an acceleration $\delta^I\mathbf{f}_c$ that affects the orbit of the real satellite, aiming to drive the error between the real satellite and the reference to zero.

This control acceleration is limited by the actuators saturation, which depends on the selected thruster. This acceleration is calculated every simulation step and is obtained by the optimal linear control law for the linearized version of the system

$$\delta^I \mathbf{f}_c = -\mathbf{K}\, \delta\boldsymbol{\epsilon},$$

where the Kalman gain **K** is calculated using the MATLAB command

$$\mathbf{K} = \text{lqr}(\mathbf{A}_\epsilon, \mathbf{B}_\epsilon, \mathbf{Q}, \mathbf{R}).$$

Matrices $\mathbf{A}_\epsilon$ and $\mathbf{B}_\epsilon$ are defined using the linearized dynamics for the error between the real satellite and the reference (4.8). Notice that $\mathbf{A}_\epsilon$ is dependent on the reference satellite Cartesian position on the ToD reference frame, which is updated every simulation step. However, to avoid an excessive computational effort, the Kalman gain might have a different update rate from the simulation step, since the most significant terms of the matrix **K** present a small variation over time and, therefore, it is not necessary to update this matrix every simulation step. The calibration of matrices **Q** and **R** is done using a trial-and-error method and had, as a starting point, the Bryson's method to reduce the level of arbitrariness (see [53]). In this method, **Q** and **R** are diagonal matrices, where each of the diagonal terms is the square of the inverse of the maximum value expected for each of the state variables error and the input control variables during the control manoeuvre respectively, that is

$$\mathbf{Q} = \text{diag}(Q_i), \qquad \mathbf{R} = \text{diag}(R_j),$$

where

$$Q_i = \frac{1}{\delta\epsilon_{i,max}^2}, \qquad R_j = \frac{1}{\delta^I \mathrm{f}_{c_{j,max}}^2},$$

with $i \in \{1,2,3,4,5,6\}$ and $j \in \{1,2,3\}$ [53]. The method of Bryson is used to compute the initial values of matrices **Q** and **R**. However, empirical fine-tuning is still necessary in order to improve the performance of the controller.

4.3 MPC Design

4.3.1 Comparison between Keplerian Elements and Cartesian Coordinates

Similarly to the LQR, to design an MPC, it is necessary to define a state function that is used during the optimisation process to predict the system behaviour over the prediction horizon. To reduce the computational effort, one possibility is to use the Cartesian coordinates representation as the state function given the simplicity of this model when compared to the Keplerian elements representation. However, the implementation of this model lead to a difficult tuning of the MPC controller due to the large variation with time of the position and the velocity of the satellite expressed in Cartesian coordinates representation.

It is considered that the most effective strategy is to use the Keplerian elements representation for the orbital motion laws (see Section 2.2.2) as a state function. This set of equations provide immediate insight into the orientation and geometry of the orbit. Moreover, this representation allows for a simpler controller tuning given that the orbital elements do not present significant variations over time when compared to the Cartesian coordinates representation. On the other hand, the state dynamics based on Keplerian elements is not used as the dynamic model for the LQR since it leads to a more complex linearization process and result. For the MPC, it is not necessary to linearize the system since this control strategy allows to use nonlinear system dynamics as the state function.

4.3.2 State Function

GVEs adapted for near-circular orbits (see Section 2.2.2) provide a convenient model to fully characterise the orbit and location of the satellite, using the set of Keplerian elements ${}^{I}\mathbf{x}_k = [a\ e_x\ e_y\ i\ \Omega\ u]^T$ as the system state, which is then compared with the reference satellite set of Keplerian elements to correct the real satellite orbital position and velocity. Although TerraSAR-X initial orbit can be modeled as near-circular, (2.4) is not used in this model since, during the orbit correction maneuvers, the orbit eccentricity presents values that are not characteristic of a near-circular orbit. Therefore, an adaptation of the near-circular orbit system dynamics is used as the MPC state function, given by

$$\begin{cases} \dot{a} & = 2\frac{a^2}{\sqrt{\mu p}}\left[{}^{O}f_3 e \sin\theta + {}^{O}f_3 \frac{p}{||\mathbf{r}||}\right] \\ \dot{e}_x & = \sqrt{\frac{p}{\mu}}\left[{}^{O}f_3 \sin\theta + {}^{O}f_3(\cos E + \cos\theta)\right] \\ \dot{e}_y & = \sqrt{\frac{p}{\mu}}\left[-{}^{O}f_3 \cos\theta + {}^{O}f_3(\sin E + \sin\theta)\right] \\ \dot{i} & = {}^{O}f_3 \frac{||\mathbf{r}||}{\sqrt{\mu p}} \cos u \\ \dot{\Omega} & = {}^{O}f_3 \frac{||\mathbf{r}||}{\sqrt{\mu p}\sin i} \sin u \\ \dot{u} & \simeq \dot{\omega} + \dot{M}_0 = n + {}^{O}f_1\left[\frac{1}{e}\sqrt{\frac{p}{\mu}} - \frac{1-e^2}{e}\sqrt{\frac{a}{\mu}}\right]\sin\theta\left[1 + \frac{||\mathbf{r}||}{p}\right] - {}^{O}f_2\frac{||\mathbf{r}||}{\sqrt{p\mu}}\cot i \sin u - \\ & \quad {}^{O}f_3\left[\frac{2||\mathbf{r}||}{\sqrt{\mu a}} + \left(\frac{1}{e}\sqrt{\frac{p}{\mu}} - \frac{1-e^2}{e}\sqrt{\frac{a}{\mu}}\right)\cos\theta\right] \end{cases}, \tag{4.9}$$

where $[{}^{O}f_1\ {}^{O}f_2\ {}^{O}f_3]^T = {}^{O}\mathbf{f}$ and ${}^{O}\mathbf{f} = {}^{O}\mathbf{f}_c + {}^{O}\mathbf{f}_{J_2}$, where ${}^{O}\mathbf{f}_c$ is the control acceleration vector expressed in the Local Orbit frame centered in the real spacecraft and ${}^{O}\mathbf{f}_{J_2}$ is the acceleration caused by the J_2 Earth gravity component, expressed in the same reference frame. Notice that, to reduce the computational effort during the optimisation process, only the J_2 Earth gravity component was considered given that the magnitude of this acceleration is 10^3 times higher than the magnitude of other perturbative accelerations that affect the real orbit [19].

4.3.3 MPC Synthesis

A MATLAB script was developed that implements the MPC and allows to assess its performance in driving the error between the real satellite and the reference to zero. Recalling Section 2.5.2, the MPC

computes the next control action as a result of an optimisation process that uses a prediction of the system behaviour during the prediction horizon. Notice that the state function defined in Section 4.3.2 is nonlinear. Thus, nonlinear MPC will be used as the control strategy. This state function is used to obtain the system evolution during the prediction horizon. However, the MPC uses a discrete-time model for this prediction and, therefore, it is good practice to provide the controller with a discrete-time state function. Otherwise, MATLAB automatically discretizes the model using the implicit trapezoidal rule, increasing the computational effort. To hasten the optimisation process, the Forward Euler's method was used to discretize the state function (4.9) since good propagation accuracy was achieved using this method without the need for excessive computational effort, as depicted in Section 2.4.

An output function to compute the system output that will be compared with the reference need to be defined. Since the spacecraft will be equipped with sensors providing position and velocity and the state ${}^{I}\mathbf{x}_k$ can be directly obtained from these measurements, the system output is the state itself. Therefore, the output function is simply given by

$$ {}^{I}\mathbf{y} = \mathbf{I}_6 {}^{I}\mathbf{x}_k, $$

where $\mathbf{I}_6$ is the 6×6 identity matrix. The system output is used to compute the reference tracking term of the cost function (2.11). The cost associated with the control action is also considered by the manipulated variable cost term (2.12). To achieve good results, it is crucial to fine-tune the weight of these terms. The strategy implemented uses an empirical method that considers the magnitude of each of the terms evaluated by the cost function to find initial values for the tuning process. Contrasting with the LQR implementation, the MPC allows to define constraints on the control acceleration, so that the optimisation process only considers control actions that are within the saturation limits of the actuators.

It is also necessary to select three design parameters, namely the prediction horizon, p_h, the control horizon, m, and the sample time, T_s. The selection of these parameters requires a good understanding of the system since they determine how far the controller looks into the future to predict the system behaviour, the number of control actions computed, and the time interval between each prediction step, respectively. The prediction time window should be large enough so that the optimisation process computes the best solution for the orbit control problem. Recalling that the prediction time is equal to the product between the prediction horizon and the sample time, a compromise must be achieved between computational effort and propagation accuracy, since the sample time must be small enough to achieve an accurate propagation of the prediction model, but large enough to achieve an acceptable prediction time window, for a given prediction horizon. Notice that a large prediction horizon means that more steps will be considered in the optimisation process, which leads to an increase in computational effort. It is good practice to choose the prediction horizon such that $p_h T_s$ is equal to the closed-loop response time and then adjust from that point until further increases on p_h have a minor impact on performance [54]. For this problem, the tuning strategy is to initially set the control horizon with the same dimension as the prediction horizon (given the complexity of the system and the effect of perturbative accelerations) and then, iteratively decrease this parameter as long as the controller performance is not affected.

The MPC controller performance can be assessed in order to evaluate the effect that the control input, computed by the controller, has on the system. A similar strategy to the one used to implement the LQR (Section 4.2.3) is proposed. The properties of the reference and the real satellites are as described in Section 4.2.3. Contrasting with the LQR implementation, in which case the system state is the error between the real satellite and the reference one, the MPC uses the set of Keplerian elements for near-circular orbits of the real satellite, expressed in the ToD reference frame, as the system state. The system output is compared with the reference satellite set of Keplerian elements, expressed in the same reference frame. However, given that the optimisation process compares these orbital elements in a certain time window and the reference satellite position and velocity vary with time, a vector with the dimension of the prediction horizon, containing the Keplerian elements of the reference satellite at every prediction step, must be provided to the controller. This vector must be updated every simulation step so that the first element of the vector corresponds to the Keplerian elements of the reference at time $k+1$, where k is the current simulation step. A schematic representation of the MATLAB script is presented in Fig. 4.2.

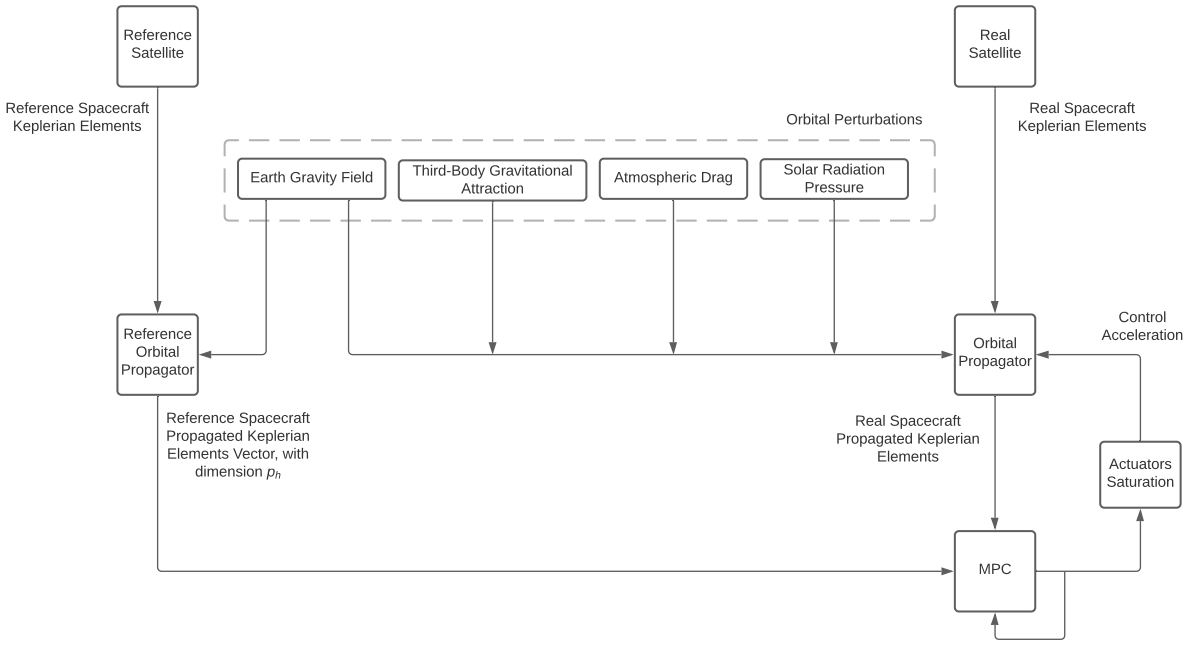

Figure 4.2: MPC implementation scheme.

The control acceleration is computed using the MATLAB command

$$[\mathbf{mv}, \mathbf{opt}] = \text{nlmpcmove}(\mathbf{nlmpcobj}, {}^{I}\mathbf{x}_k, \mathbf{lastmv}, \mathbf{Ref}),$$

where **mv** is the next control acceleration to be used in the system, **nlmpcobj** is a MATLAB object containing the MPC design properties, ${}^{I}\mathbf{x}_k$ is the current system state, **lastmv** is a 3×1 vector containing the last control action used, and **Ref** is a $p_h \times 6$ matrix containing the Keplerian elements of the reference satellite during the prediction horizon. The MATLAB object **opt** contains initial guesses for the state and

manipulated variable (control action) trajectories to be used in the next control intervals, until the end of the prediction horizon [55]. It is possible to use several of these guesses for the next control actions in order to avoid running the optimisation process at every simulation step and, in this way, reduce the computational effort. It is good practice to use this strategy when the orbital error is large, given that, in this situation, the variations of the control acceleration, from one simulation step to the other, are not very significant when compared to a situation characterised by an orbital error closer to zero.

4.4 Control Solution

To achieve good performance for different magnitudes of position error, four different controllers were implemented – MPC 1, MPC 2, LQR 1, and LQR 2 – that drive and maintain at zero the orbital error between the real satellite and the reference. The two LQR controllers are used to correct small orbital errors given that the LQR is able to correct errors close to zero with less computational effort than the MPC. LQR 1 is designed to correct small errors between the real satellite and the reference. LQR 2, on the other hand, is optimised to reduce the error in steady-state. Its purpose is to counter perturbative accelerations that affect the real orbit and handle sensors and actuators noise, in order to maintain the orbital error within the required values. The difference in the implementation of these two controllers is in the definition of matrices **Q** and **R**. The two MPC controllers are used to correct orbital errors far from zero since, in this case, the linearized model is no longer valid. Moreover, for large orbital errors, the control acceleration computed is saturated by the actuators. Therefore, the MPC provides better results since it accounts for actuators saturation in the optimisation process. MPC 1 is designed to correct larger orbital errors than the MPC 2 and these two controllers differ in the following design parameters:

- Sample time, T_s - a higher sample time is used for MPC 1 (high orbital errors), given that a smaller propagation accuracy is required in this case;
- Prediction horizon, p_h - a higher prediction horizon is used for MPC 1 (high orbital errors), given that the response time is higher in this case;
- Weights - tuning of the weights to use in the cost function is also needed for each of the MPC controllers.

A schematic representation of the MATLAB script for the complete control solution is presented in Fig. 4.3. Notice the need to convert the Cartesian position and velocity to the corresponding Keplerian elements that are used by the two MPC controllers. Also, the MPC computes the control actions vector in the Local Orbit reference frame, centered at the real spacecraft, which needs to be converted to the ToD reference frame to be used in the Cartesian orbital propagator.

The orbital position error between the real satellite and the reference, at the current simulation step, is used to select the controller that will compute the next control acceleration. Therefore, at every simulation step, the orbital position error is evaluated to decide which controller is the best to use. For orbital position errors below a given threshold, a different controller is selected. However, if the orbital position error

returns to a value above that threshold, the controller in use remains the same, except in the transition from LQR 2 to LQR 1. In this case, the controller in use returns to LQR 1 since LQR 2 is designed for steady-state.

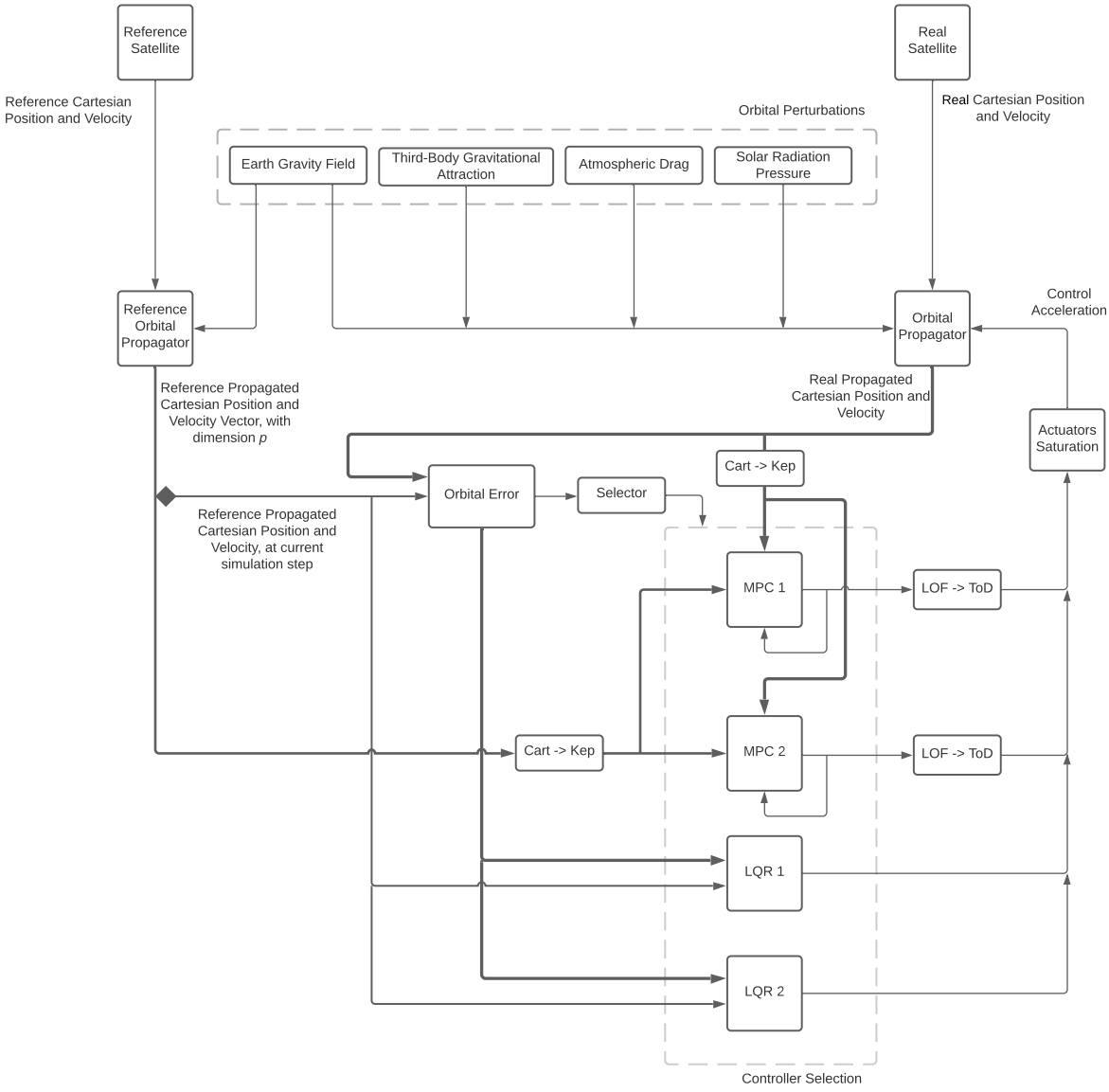

Figure 4.3: Implementation scheme of the complete control solution.

Chapter 5

Simulation Setup

In this chapter, the parameters used in the MATLAB script to characterise the TerraSAR-X spacecraft, orbit properties, and simulation environment are defined and justified. The controller parameters and the implementation strategy are also discussed in order to provide better insight and analysis of the results obtained.

5.1 TerraSAR-X Properties

The spacecraft physical characteristics of TerraSAR-X, used in the simulations, are as described in Table 3.1. The spacecraft wet mass (total mass including propellant) is 1230 kg. Since the spacecraft is affected by the drag acceleration caused by the atmosphere, the cross-sectional area of the spacecraft projected along the direction of motion, S, has to be defined in order to compute the drag acceleration using (2.5). The spacecraft has a cylindrical shape with dimensions 5 m height $\times$ 2.4 m diameter. Thus, to evaluate the controller performance in the worst-case scenario, it is considered that the cylinder circular base is parallel to the direction of the satellite motion. In this case, the cross-sectional area is a 5 m $\times$ 2.4 m rectangle and, therefore, $S = 12$ m^2. Moreover, the drag coefficient, C_D, also needs to be known. According to [56], a drag coefficient value of 2.2 is an approximation for the physical drag coefficient of satellites with compact shapes that is widely used for the computation of the drag acceleration. The spacecraft's coefficient of reflectivity, C_R, is required to compute the solar radiation pressure acceleration (2.6). A value of C_R of zero means the spacecraft is translucent to incoming radiation, a value of 1 indicates all radiation is absorbed and all the force is transmitted to the spacecraft, and a value of 2 indicates all radiation is reflected and twice the force is transmitted to the spacecraft [57]. Once more, to simulate the worst-case scenario, it is considered that $C_R = 2$. To calculate the solar radiation pressure acceleration, the cross-sectional area of the spacecraft exposed to the radiation, A_S, must be defined. Given that the worst-case scenario is considered, it is assumed that the cylinder circular base is parallel to the direction of the unit vector from the spacecraft to the Sun. In this case, the cross-sectional area is a 5 m $\times$ 2.4 m rectangle and, therefore, equal to $A_S = 12$ m^2. Table 5.1 summarises the physical properties of TerraSAR-X.

Table 5.1: Spacecraft physical characteristics of the TerraSAR-X mission.

TerraSAR-X physical characteristics	
Wet mass	1230 kg [10]
S	12 m^2 (based on [10])
A_S	12 m^2 (based on [10])
C_D	2.2
C_R	2

The orbit of TerraSAR-X is LEO, sun-synchronous, and near-circular. Therefore, using the data from Table 3.1 and the set of Keplerian elements for near-circular orbits described in Section 4.3.2 (${}^I\mathbf{x}_k = [a\ e_x\ e_y\ i\ \Omega\ u]^T$), the orbit properties are as described in Table 5.2. The scalar eccentricity of TerraSAR-X orbit is 0.0014252 [10]. However, no information is provided regarding the direction of the eccentricity vector and, therefore, an arbitrary direction is chosen, yielding $\mathbf{e} = [0.0014252\ 0]$. According to the mission requirements, the LTAN should maintain a value of $18:00$ hrs ($\pm\ 0.25$ hrs). From this value and the launch date of June 15, 2007, $02:14:00$ UTC, it is possible to obtain a value of the right ascension of the ascending node of $\Omega = 172.993$ deg using a MATLAB function that performs the conversion between LTAN and Ω [58]. No information is provided regarding the value of the argument of latitude, so an arbitrary value of $u = 0$ deg is considered.

Table 5.2: Orbit properties of the TerraSAR-X, launched on June 15, 2007, $02:14:00$ UTC [10].

TerraSAR-X Keplerian elements	
a	6892.944 km
e_x	0.0014252
e_y	0
i	97.4401 deg
Ω	172.993 deg
u	0 deg

To measure the satellite orbital position and velocity, a commercial GNSS receiver was selected from Table 2.3. Due to the instability of the nonlinear system, the NavSBR GPS receiver is used for accurate navigation data measurements. The NavSBR has a 3σ position and velocity accuracy of 1 m and 0.02 m/s, respectively. This accuracy was modeled by adding Gaussian noise, with zero mean and 3σ equal to the receiver position and velocity accuracy, to the system output. Table 5.3 summarises the NavSBR GPS properties.

As mentioned in Section 2.6.2, electric propulsion systems present several advantages when compared to chemical propulsion, namely a higher specific impulse, the capability of operating high variations of thrust, and also provide better actuation accuracy [38]. On the other hand, the amount of thrust produced by electric engines is very small, which may lengthen the correction of large orbital errors, such as

Table 5.3: NavSBR GPS receiver properties [35].

NavSBR GPS receiver	
Pos. accuracy ($\pm 3\sigma$)	1 m
Vel. accuracy ($\pm 3\sigma$)	0.02 m/s

the ones resulting from the launcher orbital injection. Therefore, this type of propulsion is more suitable for low-thrust and long-duration applications, such as orbit maintenance maneuvers. However, most missions cannot afford embarking two different types of thrusters. Therefore, in this thesis, it was decided to equip the spacecraft solely with electrical propulsion, which is the system that offers better prospects of reducing the orbit maintenance errors.

TerraSAR-X has a total wet mass of 1230 kg, meaning that significant thrust values are required to correct large orbital errors. A feasible strategy must be devised based on the electric thrusters presented in Table 2.6. BUSEK BHT-8000 Hall thruster provides the highest nominal thrust, which means that it is the most suitable actuator for the control objectives. Nevertheless, one single thruster does not provide sufficient thrust to correct considerable orbital errors of a large satellite such as TerraSAR-X. Therefore, the strategy adopted uses $9 \times$ BUSEK BHT-8000 thrusters, three in each of the corresponding actuation axis. Table 5.4 summarises BUSEK BHT-8000 properties.

Table 5.4: BUSEK BHT-8000 thruster properties [49].

BUSEK BHT-8000	
Nominal thrust (max.)	450 mN
I_{sp}	2210 s
Power	8 kW
Thrust error (2σ)	1%
Qty.	9

Since chemical propulsion systems for this class of spacecraft can weigh more than 100 kg and electrical propulsion is nowadays the subject of intensive research and its thrust-to-mass ratio is expected to improve in the coming years, it was decided to maintain the original TerraSAR-X wet mass. Nevertheless, the relatively small thrust-to-mass ratio is one drawback in the use of electric propulsion, given that a large number of actuators may be required to correct large orbital errors. Since no information is provided on the data-sheet of BUSEK BHT-8000 about thrust accuracy, a general example of a mission that uses electric thrusters is used to estimate this parameter. According to [59], the difference between thrust demand and actual thrust for the QinetiQ T5 ion thrusters used in the ESA GOCE mission occurs within ± 1% of the thrust demand. Therefore, a similar thrust error is assumed for the BUSEK BHT-8000. This error is modeled by adding Gaussian noise, with zero mean and 2σ equal to 1% of the thrust demand, to the actuator's output.

5.2 Simulation Environment

As referred to in Section 4.2.3, the reference satellite orbit is only affected by the orbital perturbation caused by the Earth gravity field, so that the orbital precession due to the oblateness of the Earth can be leveraged to keep the LTAN constant. On the other hand, the real satellite orbit is affected by the orbital perturbations caused by the Earth gravity field, the solar radiation pressure, the atmospheric drag, and the third-body gravitational attraction. The NRLMSISE-00 atmospheric model, described in Section 2.3.1, is used to calculate the local atmospheric density, which is required to calculate the atmospheric drag acceleration.

Table 5.5: Perturbation forces that affect the real and the reference satellite.

Perturbative force	Reference Satellite	Real Satellite
Atmospheric drag		X
Solar radiation pressure		X
Third-body gravitational attraction		X
Earth gravity field	X	X

The Forward Euler method, with a time step of 1 s, is used for the propagation of the real and the reference satellite since good propagation accuracy was achieved using this method without the need for excessive computational effort, as depicted in Section 2.4.

Table 5.6: Propagation method and simulation time step used in the simulations.

Propagation method	Simulation time step
Forward Euler	1 s

5.3 Controller Definition

Four different controllers are implemented to perform orbit correction activities depending on the error magnitude, as described in Section 4.4. Therefore, three threshold values, that are compared with the orbital position error between the real satellite and the reference, need to be defined to decide which controller will compute the next control acceleration. MPC 1 is designed to correct large orbital errors, so, this controller, is used for orbital position errors larger than 100 km. MPC 2 is used for orbital position errors smaller than 100 km. A variable threshold determines the transition from MPC 2 to LQR 1. The value of this threshold is empirically adapted to the simulation to perform, in order to improve the performance. The transition from LQR 1 to LQR 2 occurs when the orbital position error is smaller than 0.5 km. When the orbital error reaches this threshold, convergence is assured, as verified in the simulations. The threshold values to determine the transition between each controller are presented in Table 5.7.

Table 5.7: Threshold values to select the controller.

Controller threshold	
MPC 1	≥ 100 km
MPC 2	100 km $\leftrightarrow$ variable
LQR 1	variable $\leftrightarrow 0.5$ km
LQR 2	≤ 0.5 km

To design the two MPC controllers, several control parameters must be selected. The values used are summarised in Table 5.8. A compromise is achieved between computational effort and control performance since it is not feasible to define a prediction time ($p_h\ T_s$) equal to the closed-loop response. Therefore, a prediction horizon of 50 steps is used for both MPC controllers, since that does not require an excessive amount of computational effort. Moreover, a sample time of 10 s is chosen for the MPC 1, given that this value allows extending the prediction time to compute the best sequence of maneuvers, at the cost of reducing the propagation accuracy. For the MPC 2, a smaller value is used. In this case, since the orbital error is closer to zero, the propagation accuracy becomes more important to achieve convergence. Therefore, a sample time of 5 s is chosen for the MPC 2. The control horizon has the same dimension as the prediction horizon for both MPC controllers, since a decrease in the value of this parameter results in a loss of control performance, as observed in the simulations. For the MPC 1, all the control actions of the control vector (with dimension equal to the control horizon) computed by the MPC are used to control the real satellite, before a new control vector is obtained. On the other hand, for the MPC 2, only the first 40 elements of the control vector are used. The tuning of the reference tracking weights, $\mathbf{w^y}$, and manipulated variable cost weights, $\mathbf{w^u}$, to use in the cost function, resulted in the vectors presented in Table 5.8, which are the same for both MPC controllers.

Table 5.8: MPC controllers parameters.

Parameters	MPC 1	MPC 2
T_s	10 s	5 s
p_h	50 steps	50 steps
m	50 steps	50 steps
Control vector usage	50 control actions	40 control actions
$\mathbf{w^y}$	$[0.009\ 11\ 11\ 2\ 2\ 4]^T$	$[0.009\ 11\ 11\ 2\ 2\ 4]^T$
$\mathbf{w^u}$	$[0.1\ 0.1\ 0.1]^T$	$[0.1\ 0.1\ 0.1]^T$

To implement the two LQR controllers, the matrices **Q** and **R** need to be defined using the methodology presented in Section 4.2.3. For LQR 1, these matrices are given by

$$\mathbf{Q}_{LQR1} = \text{diag}\left(\left[\frac{1}{10^{-2}}\ \frac{1}{10^{-2}}\ \frac{1}{10^{-2}}\ \frac{1}{10^{-8}}\ \frac{1}{10^{-8}}\ \frac{1}{10^{-8}}\right]^T\right)$$

and

$$\mathbf{R}_{LQR1} = \text{diag}\left(\left[\frac{1}{1.7183^{-15}} \;\; \frac{1}{1.7183^{-15}} \;\; \frac{1}{1.7183^{-15}}\right]^T\right).$$

For LQR 2, the matrix **R** is adapted to work when the error in the system state is small. Therefore, the cost of the control action is reduced in order to deal with actuator and sensors noise and maintain the orbital error small enough to fulfill the mission requirements, despite the effect of orbital perturbations. Defining $\mathbf{Q}_{LQR2} = \mathbf{Q}_{LQR1}$, the matrix **R**, for LQR 2, is given by

$$\mathbf{R}_{LQR2} = \text{diag}\left(\left[\frac{1}{3.4285^{-14}} \;\; \frac{1}{3.4285^{-14}} \;\; \frac{1}{3.4285^{-14}}\right]^T\right).$$

An update time of 50 s is chosen to update the Kalman gain, for both LQR controllers, since the elements of **K** present small variations over time. This value offers good results while reducing the computational effort and is obtained using a trial-and-error methodology.

Chapter 6

Simulation Results

In this chapter, the controller performance in driving and maintaining the orbital error of the TerraSAR-X at zero is shown and analysed. In order to have a representative example of the type of orbital errors that can occur, the injection accuracy of the Vega-C launch system is used to set the initial errors. The objective is to evaluate the controller performance in correcting different real-case scenario errors that result from the orbital injection process. The injection accuracy (3σ of a Gaussian distribution) of the Vega-C launch system is presented in Table 6.1, based on [60]. In addition, an error in u is simulated in this section to represent the correction of an advance in the orbital position of the real satellite.

Table 6.1: Vega-C launch system injection accuracy (3σ) [60].

Injection accuracy	
a	15 km
e	0.0012
i	0.15 deg
Ω	0.2 deg

6.1 Semi-major axis injection error

Based on Table 6.1, an initial error of -15 km is set for the semi-major axis of the real satellite. Thus, the initial Keplerian elements vector of the real satellite is given by

$$^{I}\mathbf{x}_{k_0} = [6877.944 \;\; 0.0014252 \;\; 0 \;\; 97.4401 \;\; 172.993 \;\; 0]^T.$$

The controller performance is assessed for a simulation with a duration equal to 2 complete orbits of the reference satellite around the Earth (approximately 11380 s). In this simulation, ideal actuators and sensors are considered, in the sense that no noise interference is simulated. Later in this document, the controller performance is evaluated in a simulation with realistic actuators and sensors.

Figure 6.1 illustrates the variation of the Keplerian elements error between the real and the reference satellite. Notice that, since the semi-major axis of the real satellite is smaller than the one of the reference satellite, the mean motion of the real satellite is higher than the mean motion of the reference satellite, which justifies the initial increase in the argument of latitude error. The effect of the control acceleration causes a significant variation on the eccentricity, visible on the variation of the eccentricity vector, which justifies why (2.4) is not used in the state function (4.9). Also, a different value of the semi-major axis for the real and the reference satellite causes a different variation on the longitude of the ascending node due to the effect of the Earth gravity field. This results in the error in the longitude of the ascending node, illustrated in Fig. 6.1.

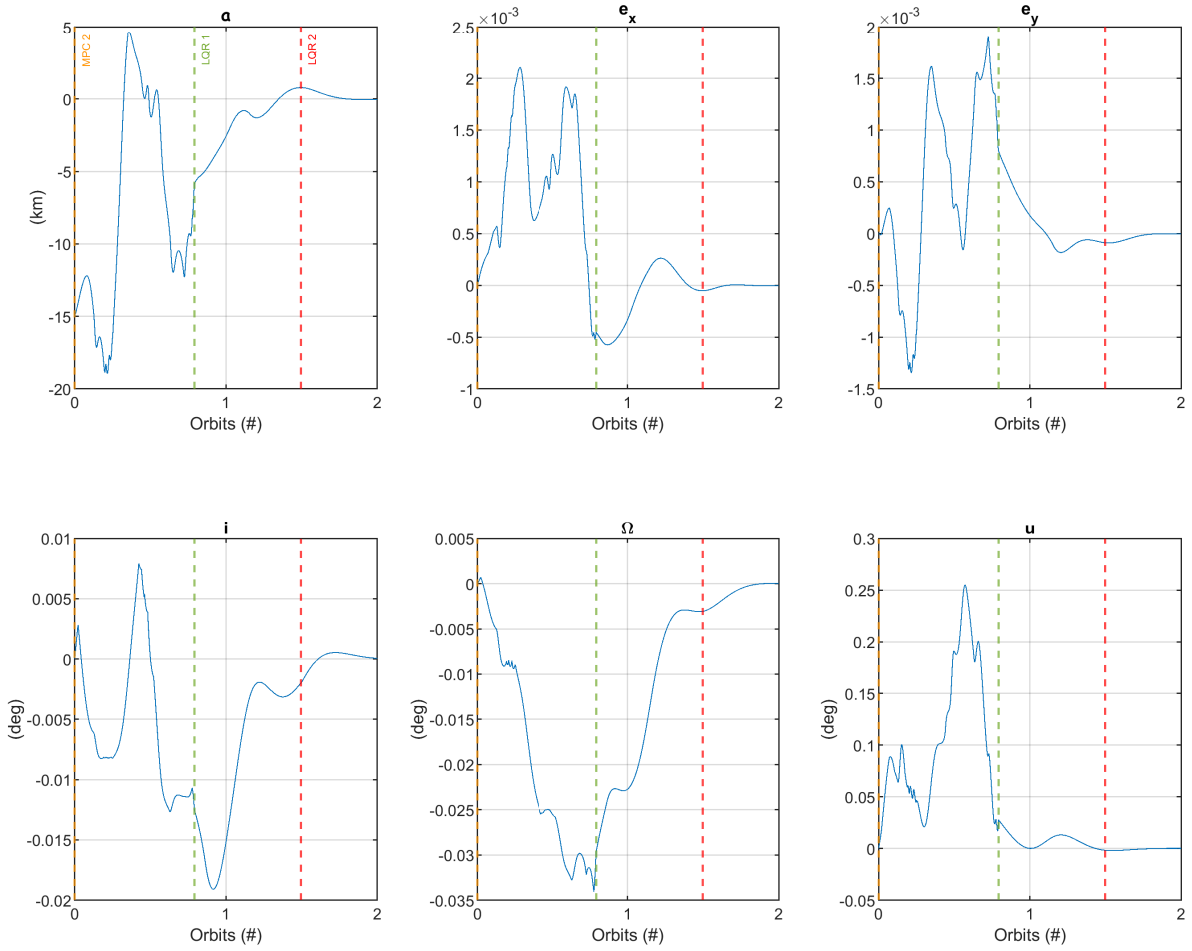

Figure 6.1: Keplerian elements error between the real and the reference satellite for an initial error in the semi-major axis. The transition between the controller in use is marked with a dashed line.

A better perspective on the relative motion between the real and the reference satellite is provided by Fig. 6.2. This figure illustrates the variation of the Cartesian components of the real satellite expressed in a Local Orbit reference frame, centered at the reference satellite center of mass. The initial semi-major axis error is reflected in the radial direction, o_3. Since the altitude of the real satellite orbit is lower,

the mean motion of the satellite is higher and, therefore, the tangential velocity, v_{o_1} is also higher. This causes an advance of the real satellite relative to the reference, reflected in o_1 and u (see Fig. 6.1), due to the actuators saturation, which are not capable of rapidly correct the real satellite orbital error. The controller acts on the real satellite increasing its altitude, so it is higher than the reference satellite altitude as reflected in o_3, in order to reduce its mean motion and, consequently, reduce v_{o_1} to correct the initial orbital advance. Notice that the described motion happens during the MPC actuation regime, which is able to predict the best long-term strategy to correct the orbital error.

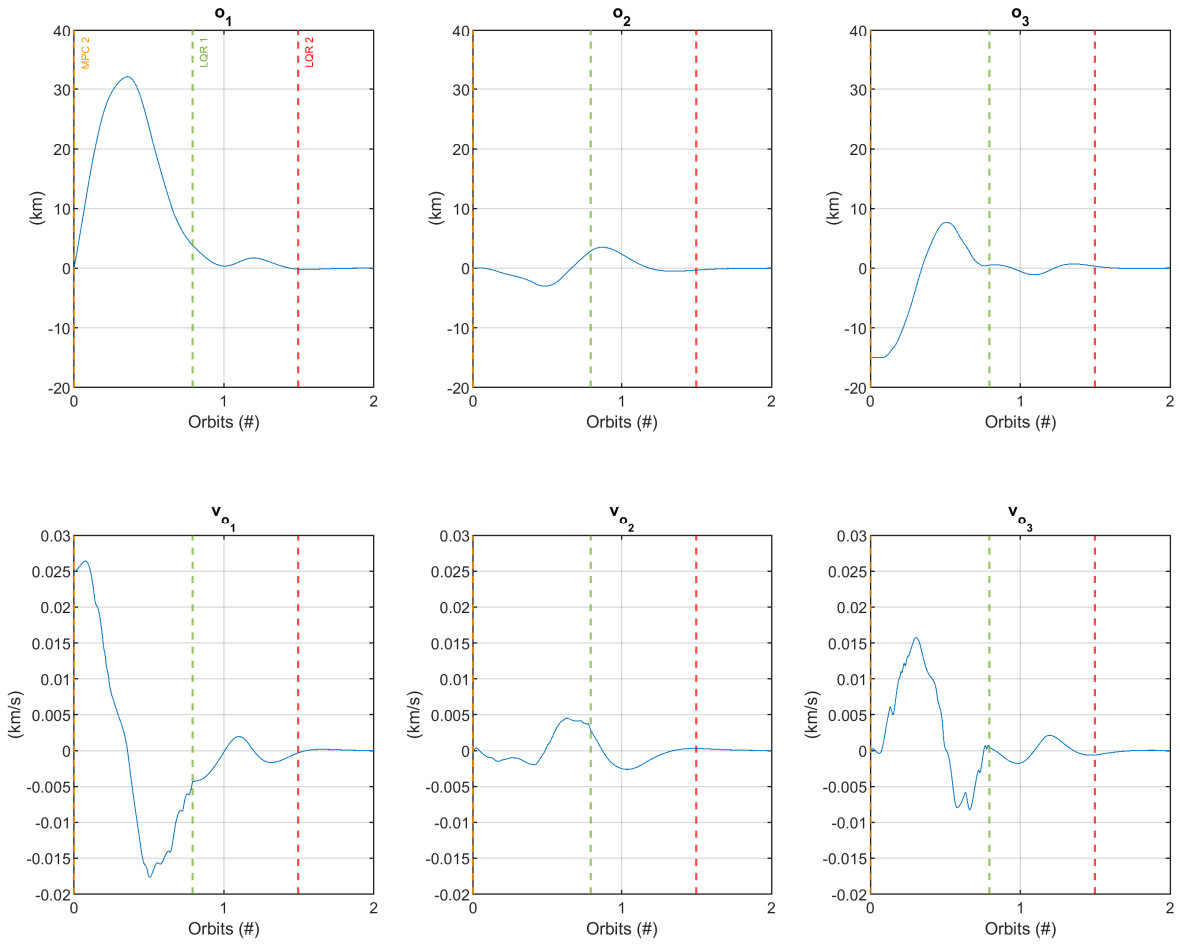

Figure 6.2: Variation of the Cartesian components of the real satellite expressed in a Local Orbit reference frame, centered at the reference satellite center of mass, for an initial error in the semi-major axis.

Figure 6.3 illustrates the control acceleration described in a Local Orbit reference frame, centered at the real satellite center of mass. From this figure, it is noticeable that the control acceleration magnitude has a maximum limit due to the actuators saturation.

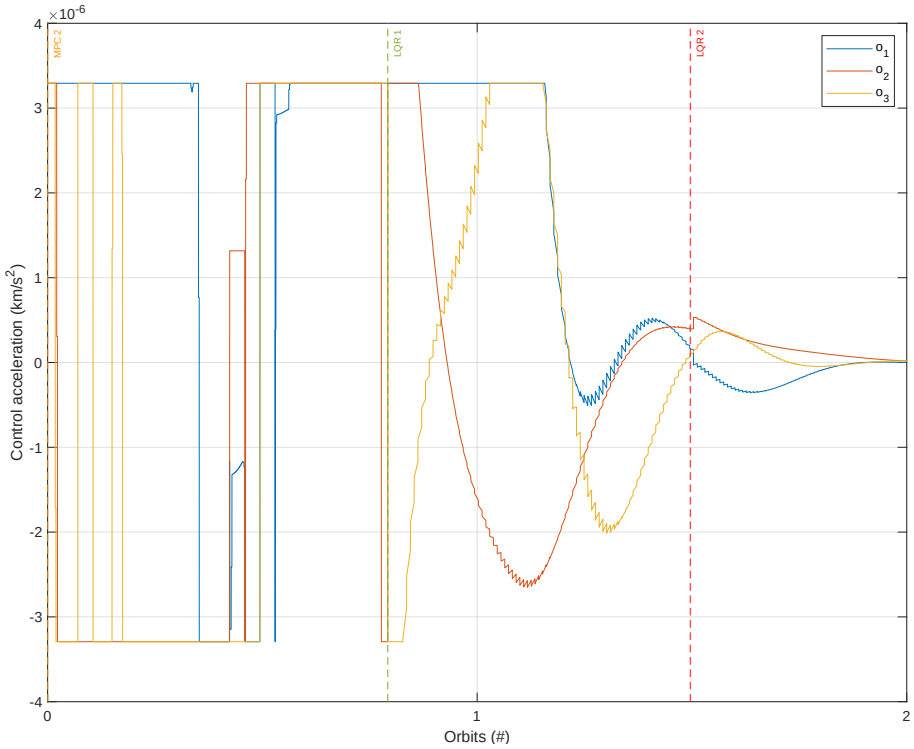

Figure 6.3: Control acceleration described in a Local Orbit reference frame, centered at the real satellite center of mass, for an initial error in the semi-major axis.

Figure 6.4 and Fig. 6.5 illustrate the magnitude of the position and the velocity error, respectively, throughout the simulation. Notice the oscillations that are present, mainly, in the magnitude of the velocity error since the control acceleration has a more direct impact on the velocity than on the position of the satellite. The initial increase in the magnitude of the position error is related to the initial advance of the real satellite, relative to the reference. The transition between controllers, marked with dashed lines, is also illustrated in the figures. For this simulation, the transition from MPC 2 to LQR 1 occurs at a position error magnitude of 4.8 km. This value is obtained using a trial-and-error methodology.

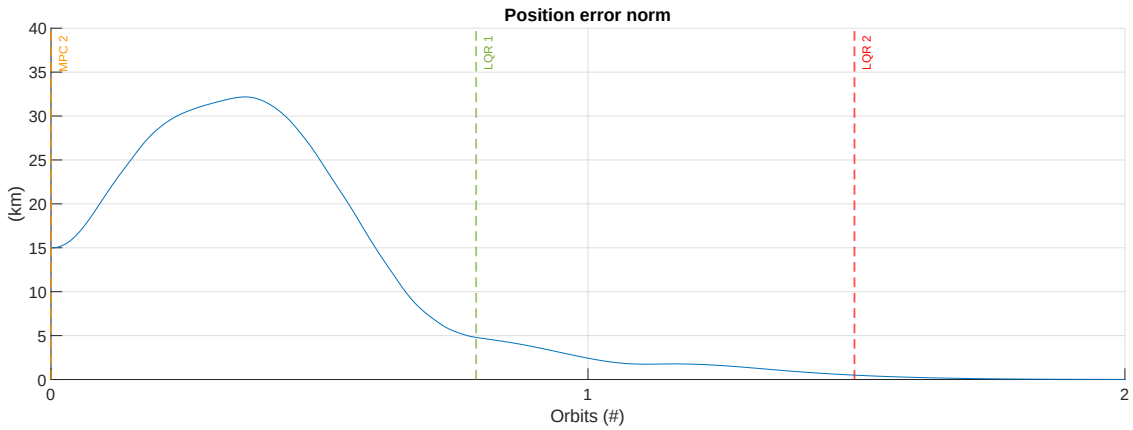

Figure 6.4: Magnitude of the position error for an initial error in the semi-major axis.

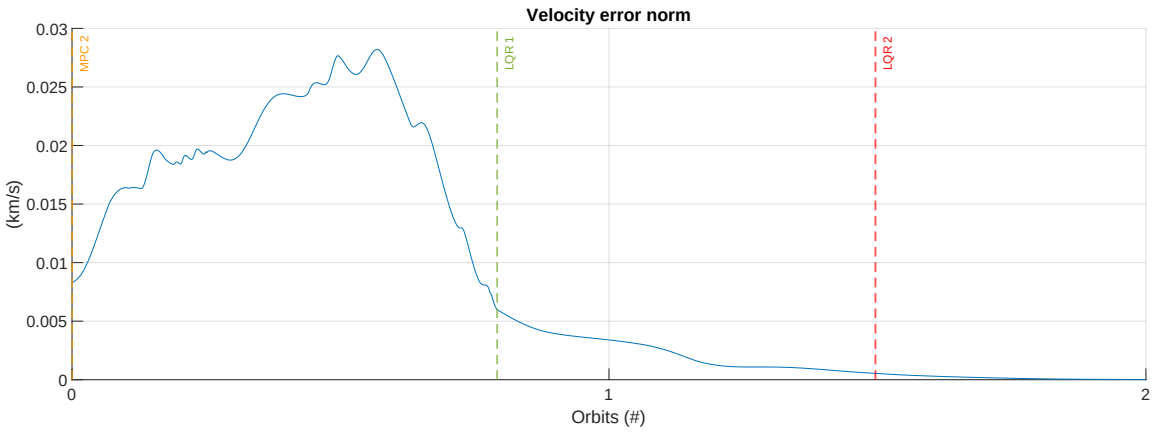

Figure 6.5: Magnitude of the velocity error for an initial error in the semi-major axis.

The response time of the system is evaluated in the transition from LQR 1 to LQR 2. In this case, a response time of 8514 s (approximately 1.5 complete orbits of the reference satellite) is obtained. On that occasion, the ground track repeatability error is below 500 m, fulfilling the mission requirements, as illustrated in Fig. 6.6.

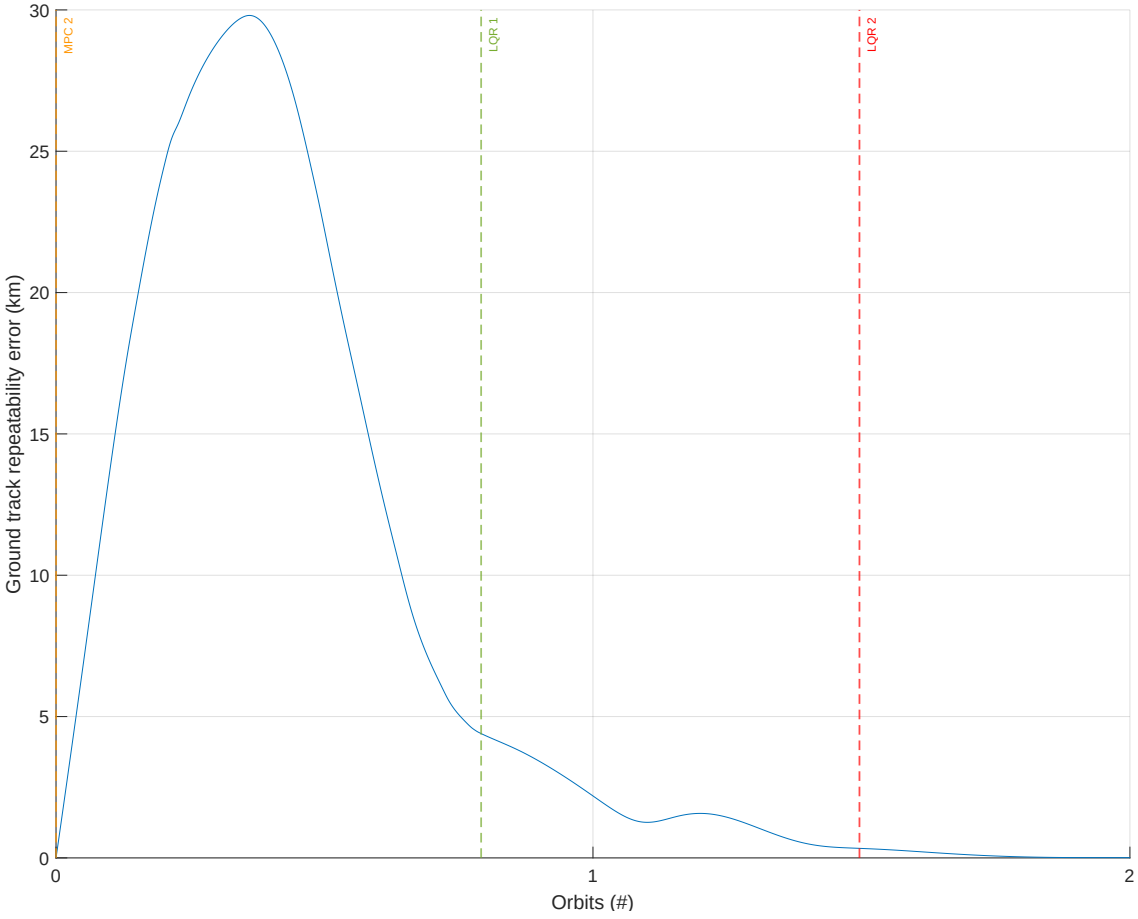

Figure 6.6: Ground track repeatability error for an initial error in the semi-major axis.

6.2 Inclination injection error

Based on Table 6.1, an initial error of $+0.15$ deg is set for the orbital inclination of the real satellite. In this case, the Keplerian elements vector of the real satellite is given by

$$^{I}\mathbf{x}_{k_0} = [6892.944 \;\; 0.0014252 \;\; 0 \;\; 97.5901 \;\; 172.993 \;\; 0]^T.$$

A simulation with a duration equal to 3 complete orbits of the reference satellite (approximately 17070 s) is used to assess the controller performance. In this simulation, ideal actuators and sensors are considered, in the sense that no noise interference is present.

Figure 6.7 illustrates the variation of the Keplerian elements error between the real and the reference satellite. The initial error in the orbital inclination converges to zero, causing the error in the other orbital elements, mainly in the semi-major axis and in the longitude of the ascending node, to present slight variations that are also corrected.

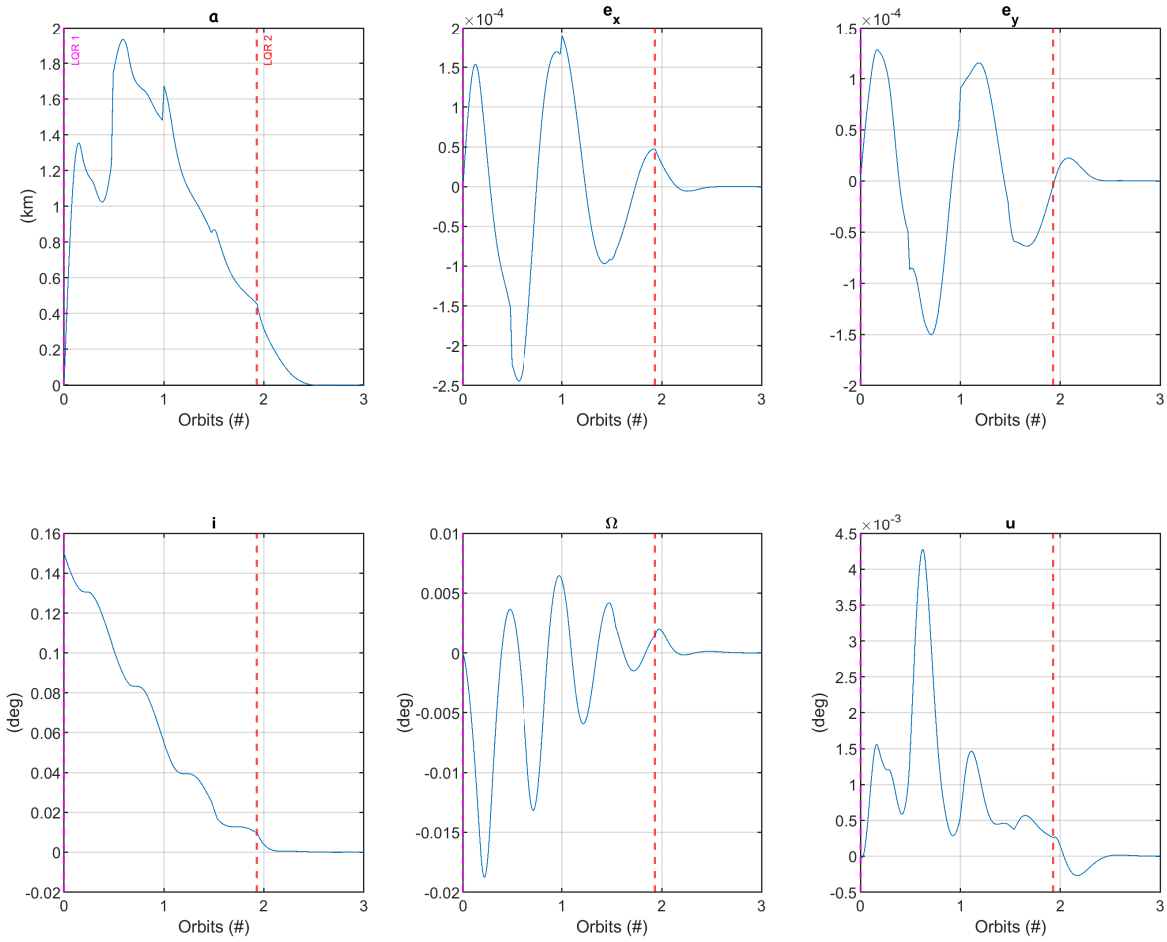

Figure 6.7: Keplerian elements error between the real and the reference satellite for an initial error in the orbital inclination.

A better perspective on the relative motion between the real and the reference satellite is provided by Fig. 6.8. This figure illustrates the variation of the Cartesian components of the real satellite expressed in

a Local Orbit reference frame, centered at the reference satellite center of mass. The orbital inclination error of $+0.15$ deg causes an initial error in the normal direction, o_2. The transition from positive to negative values, observable in this direction, occurs at the point where the orbit of the real and the reference satellite cross, due to the different orbital inclination. However, this value is converging to zero as a consequence of the control actuation.

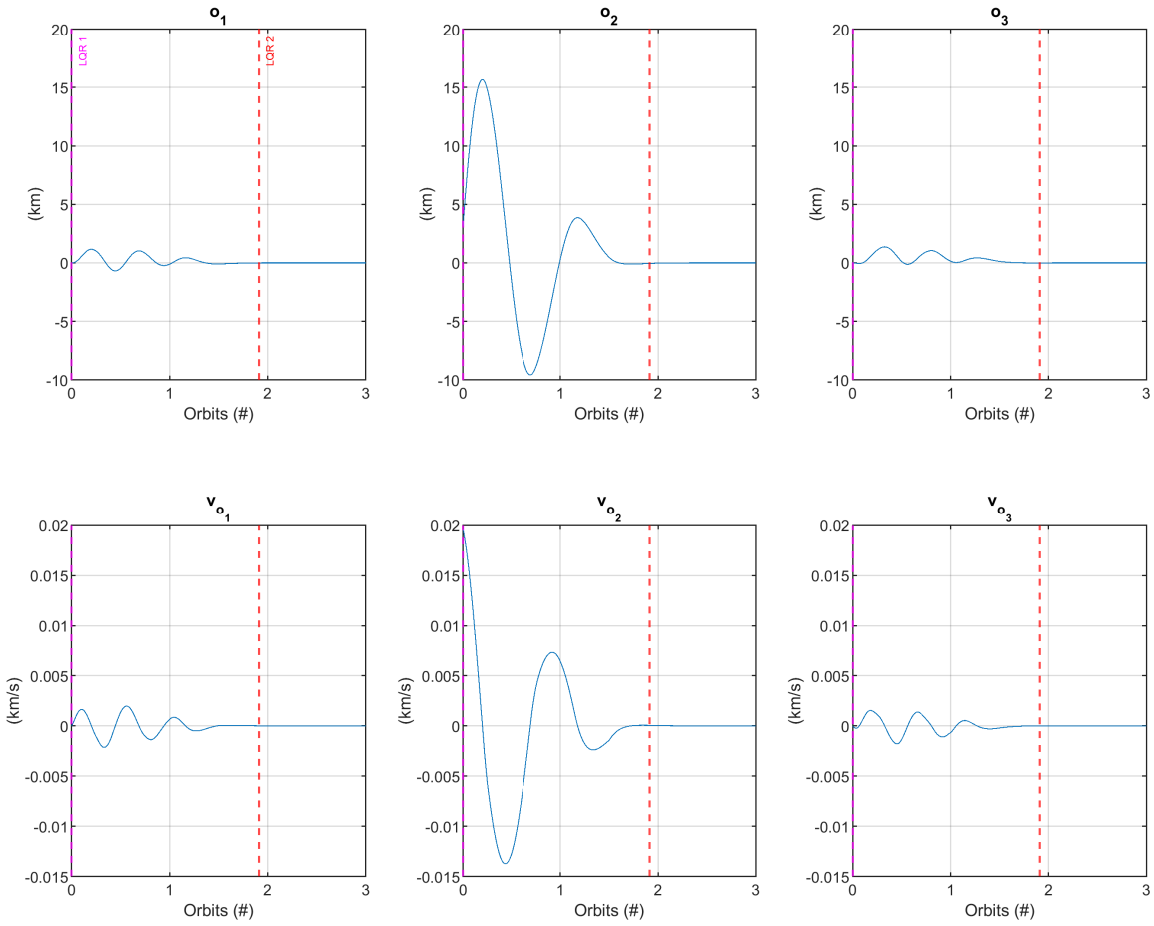

Figure 6.8: Variation of the Cartesian components of the real satellite described in a Local Orbit reference frame, centered at the reference satellite center of mass, for an initial error in the orbital inclination.

Figure 6.9 illustrates the control acceleration described in a Local Orbit reference frame, centered at the real satellite center of mass. From this figure, it is noticeable that most of the actuation is done in the o_2 direction.

The position and the velocity error magnitude, throughout the simulation, is illustrated in Fig. 6.10. The oscillations derive from the relative motion of the real and the reference satellite described above. For this simulation, notice that only the two LQR controllers are used, given that this type of controllers are capable of reducing the orbital error with less computational effort. The response time of the system is assessed based on the transition from LQR 1 to LQR 2. In this case, a response time of 10877 s (approximately 2 complete orbits of the reference satellite) is obtained. At this point, the ground track repeatability error is below 500 m, fulfilling the mission requirements, as illustrated in Fig. 6.11.

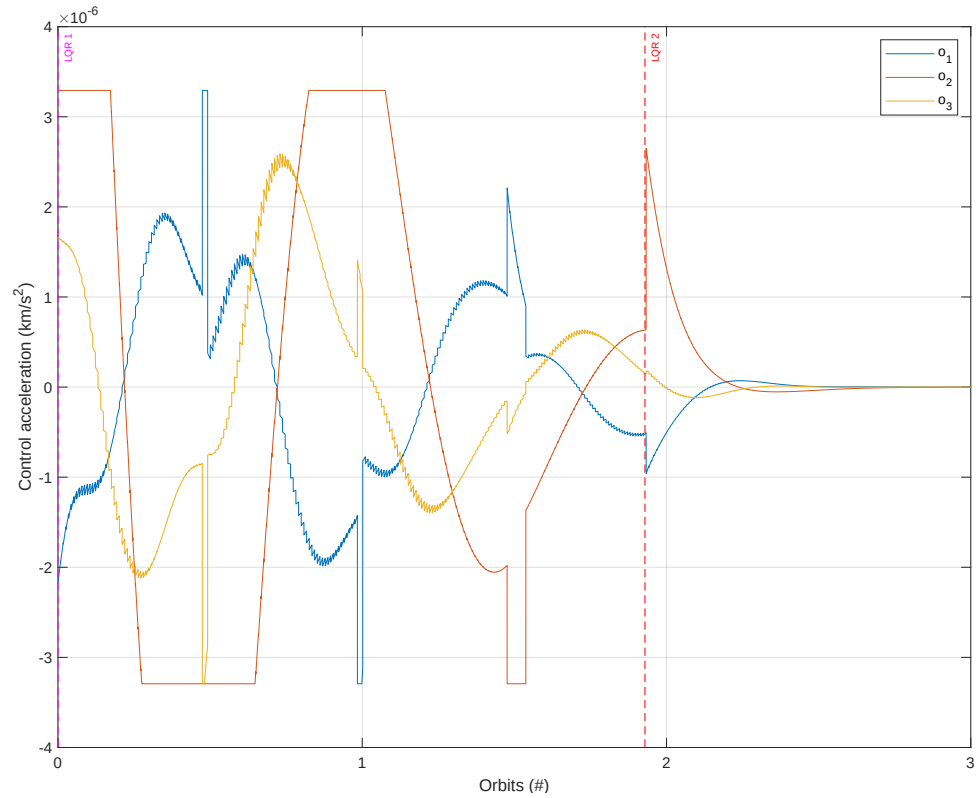

Figure 6.9: Control acceleration described in a Local Orbit reference frame, centered at the real satellite center of mass, for an initial error in the orbital inclination.

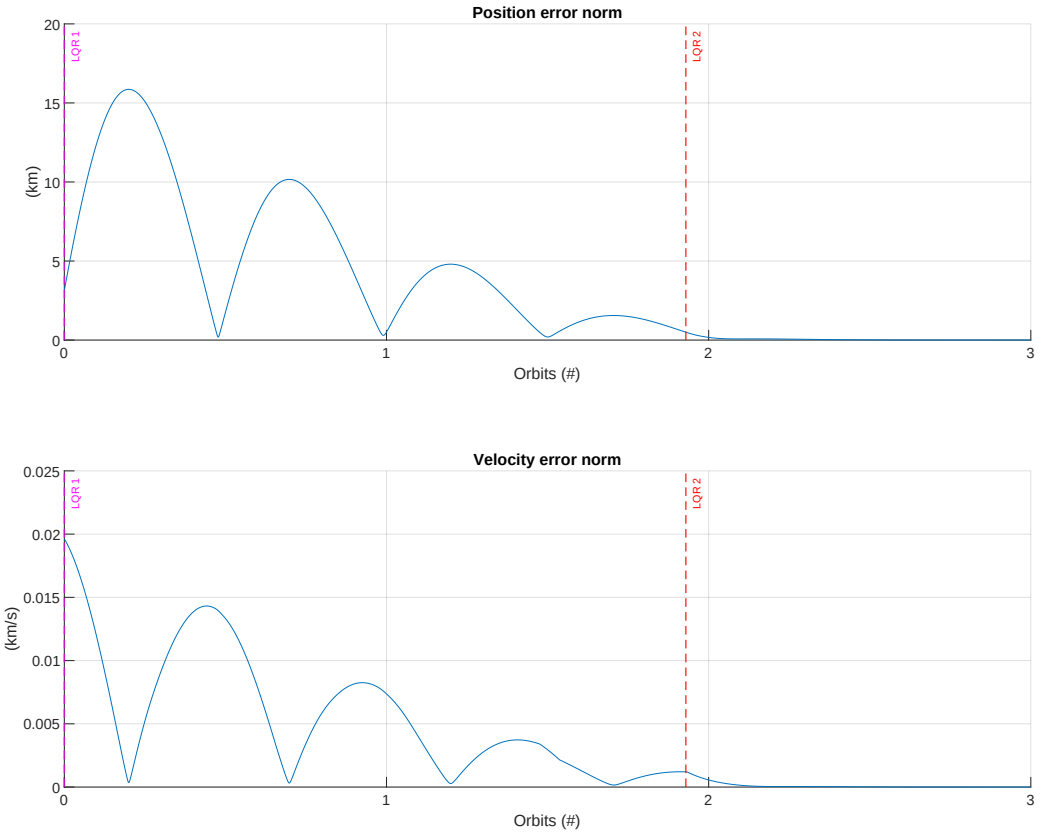

Figure 6.10: Magnitude of the position and the velocity error for an initial error in the orbital inclination.

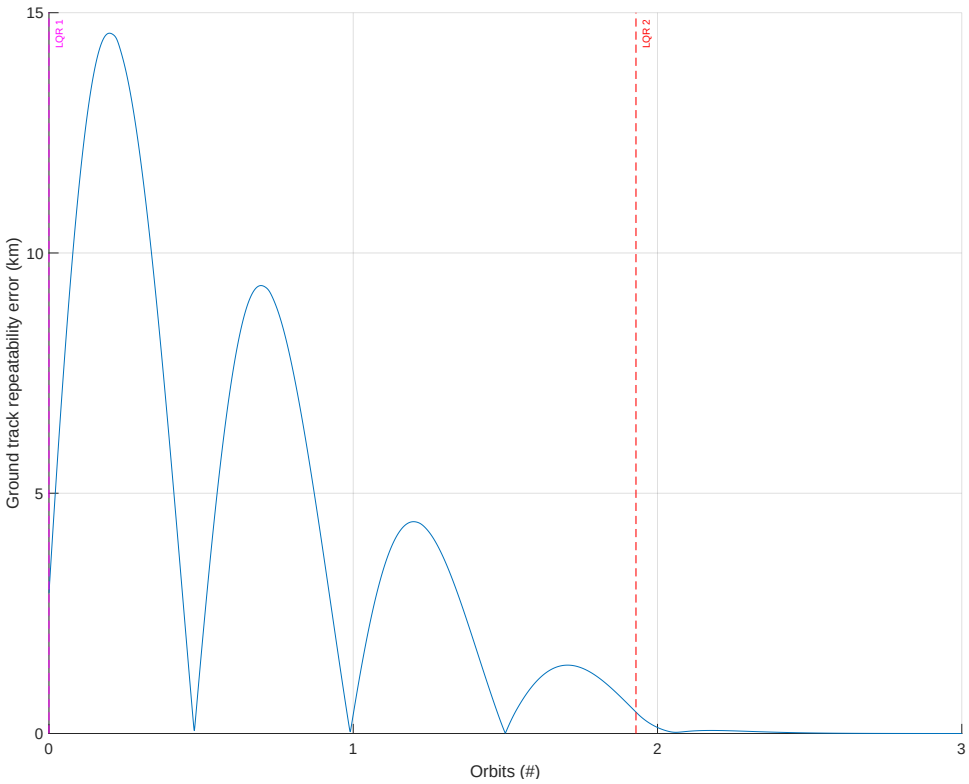

Figure 6.11: Ground track repeatability error between the real and the reference satellite for an initial error in the orbital inclination.

6.3 Argument of latitude injection error

To simulate the correction of an advance in the orbital position of the real satellite, an initial error of $+2$ deg is set for the argument of latitude of this satellite. Thus, the Keplerian elements vector of the real satellite is given by

$$^{I}\mathbf{x}_{k_0} = [6892.944 \;\; 0.0014252 \;\; 0 \;\; 97.4401 \;\; 172.993 \;\; 2]^T.$$

The controller performance is assessed for a simulation with a duration equal to 7 complete orbits of the reference satellite (approximately 39830 s). This simulation is longer than the previous two due to the large magnitude of the error to be corrected. In this simulation, ideal actuators and sensors are considered, in the sense that no noise interference is simulated.

Figure 6.12 illustrates the variation of the Keplerian elements error between the real and the reference satellite. To correct the error in the argument of latitude, the semi-major axis of the real satellite is increased, while maintaining a near-circular orbit, to reduce the mean motion of the real satellite. This causes a delay in the argument of latitude of the real satellite until the initial error in this parameter is corrected. This process is very demanding with significant oscillations of all Keplerian elements due to the complexity of the system to be controlled.

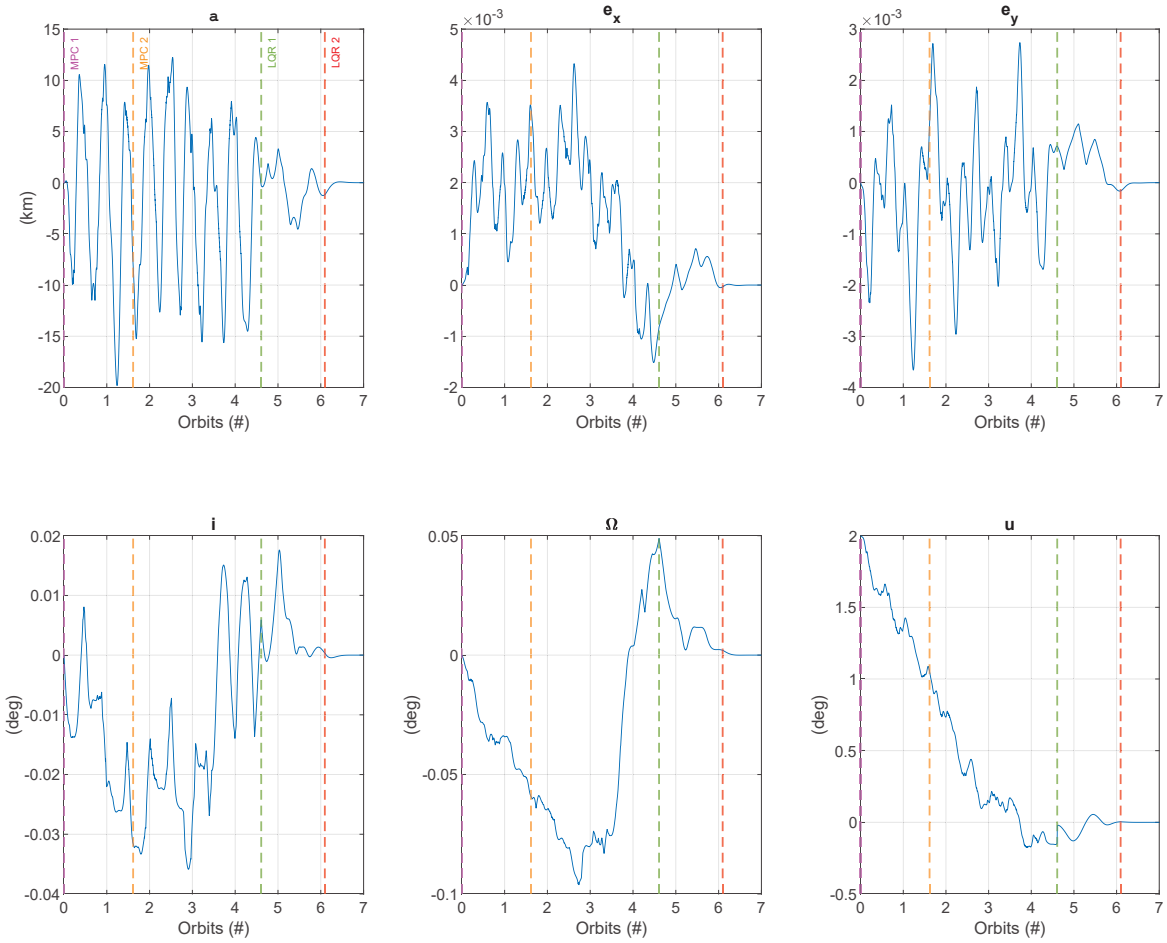

Figure 6.12: Keplerian elements error between the real and the reference satellite for an initial error in the argument of latitude.

Figure 6.13 illustrates the variation of the Cartesian components of the real satellite expressed in a Local Orbit reference frame, centered at the reference satellite center of mass. This figure provides a good perspective on the relative motion between the real and the reference satellite. The error in the argument of latitude is mainly reflected in the tangential direction, o_1. To correct this error, the real satellite altitude is increased, as reflected on o_3, in order to reduce its mean motion. This decrease in the real satellite mean motion is reflected on v_{o_1}, dominated by negative values, which, consequently, correct the orbital advance of this satellite.

Figure 6.14 illustrates the control acceleration described in a Local Orbit reference frame, centered at the real satellite center of mass. From this figure, it is noticeable a large number of variations in the control acceleration direction when compared to Fig. 6.3. This oscillatory response occurs since a large argument of latitude error is defined when compared to the error simulated for the semi-major axis.

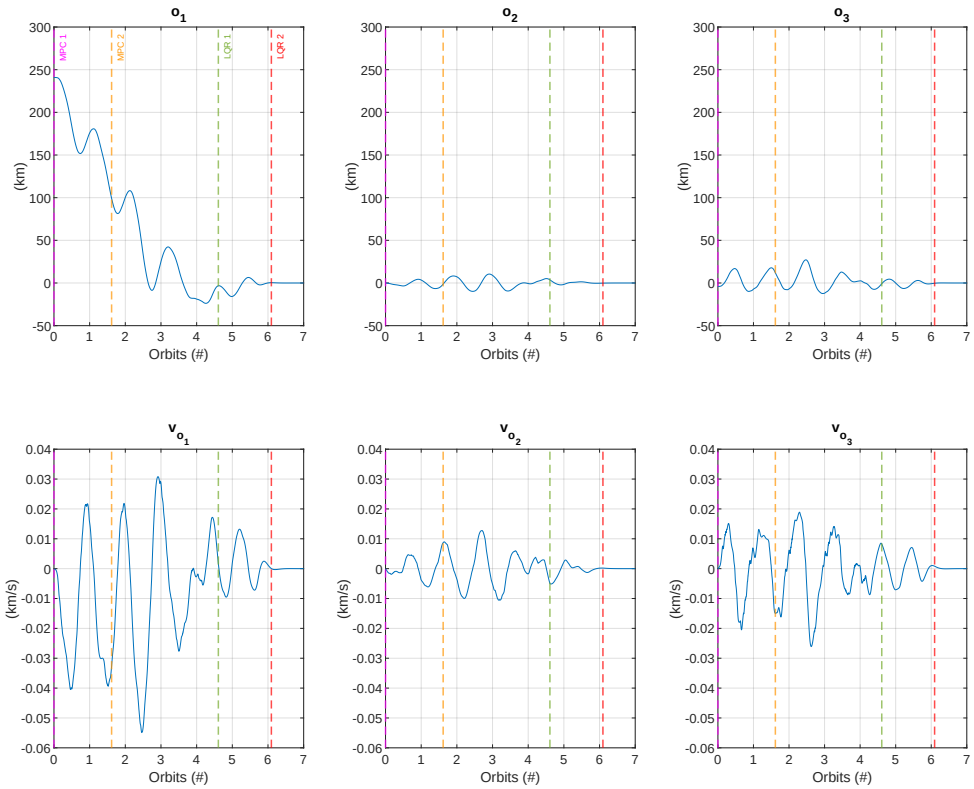

Figure 6.13: Variation of the Cartesian components of the real satellite expressed in a Local Orbit reference frame, centered at the reference satellite center of mass, for an initial error in the argument of latitude.

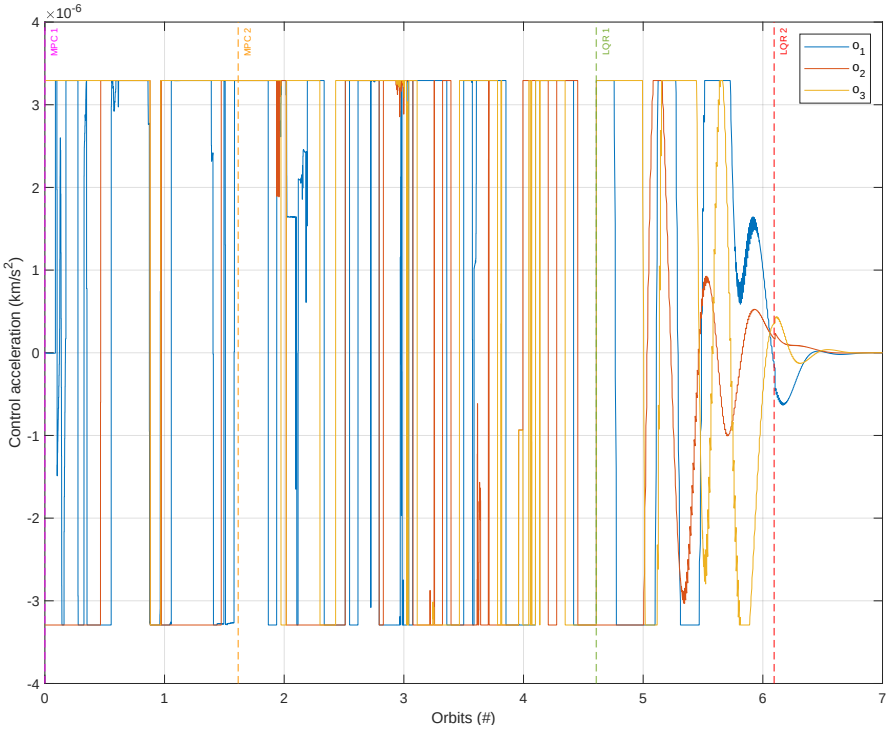

Figure 6.14: Control acceleration described in a Local Orbit reference frame, centered at the real satellite center of mass, for an initial error in the argument of latitude.

The position and velocity error magnitude between the real and the reference satellite, throughout the simulation, is illustrated in Fig. 6.15. Notice the magnitude of the initial position error, which determines the use of MPC 1. For this simulation, the transition from MPC 2 to LQR 1 occurs at a position error magnitude of 5 km. This value is obtained using a trial-and-error methodology.

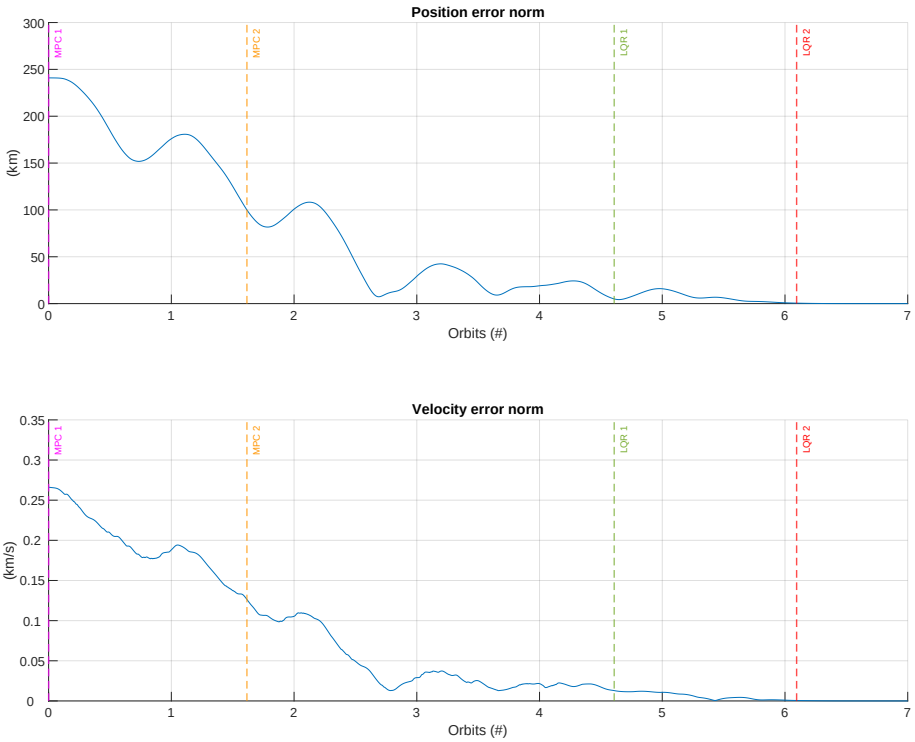

Figure 6.15: Magnitude of the position and the velocity error for an initial error in the argument of latitude.

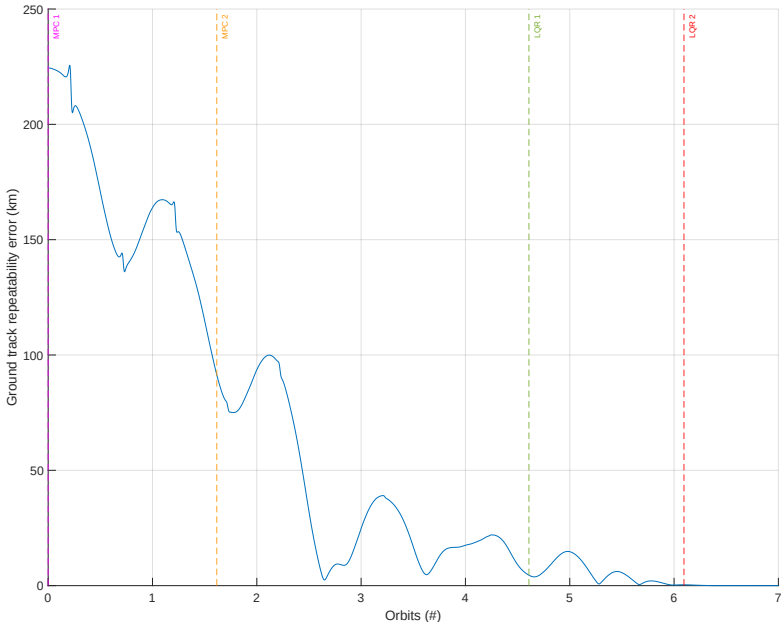

Figure 6.16: Ground track repeatability error between the real and the reference satellite for an initial error in the argument of latitude.

The response time of the system is evaluated in the transition from LQR 1 to LQR 2. In this case, a response time of 34679 s (approximately 6 complete orbits of the reference satellite) is obtained. Notice that the ground track repeatability error is below 500 m when the transition from LQR 1 to LQR 2 occurs, fulfilling the mission requirements, as illustrated in Fig. 6.16.

6.4 Combined injection error

Using a combination of errors in the Keplerian elements between the real and the reference satellite, it is possible to define three different sets of injection errors with different magnitudes. The worst-case scenario error, the one with the highest magnitude, is defined considering the maximum injection error in all Keplerian elements shown in Table 6.1 and an additional error in u. The other two errors are also characterised by a combination of errors in all Keplerian elements, but with a smaller magnitude in each of them. These three orbital errors are defined in Table 6.2.

Table 6.2: Combined injection errors between the real and the reference satellite.

Error	a	e_x	e_y	i	Ω	u
Error a)	-15 km	$+0.0012$	0	$+0.15$ deg	$+0.2$ deg	$+2$ deg
Error b)	$+8$ km	$+0.0006$	0	-0.07 deg	$+0.1$ deg	$+1.2$ deg
Error c)	$+3$ km	-0.0002	0	-0.04 deg	-0.07 deg	-0.5 deg

The controller performance is assessed for a simulation with a duration equal to 7 complete orbits of the reference satellite (approximately 39830 s). In this simulation, ideal actuators and sensors are considered, in the sense that no noise interference is simulated.

Figure 6.17 and Fig. 6.18 illustrate, respectively, the position and the velocity error magnitude, throughout the simulation, for each of the initial errors defined at Table 6.2. Notice that all of them converge to zero, as intended, and that the ground track repeatability error requirement is fulfilled, as illustrated in Fig. 6.19. The use of each of the controllers is processed as described in Table 5.7 and, in this case, the transition from MPC 2 to LQR 1 occurs at a position error magnitude of 8 km. Therefore, MPC 1 is only used to correct error a) and error b), whereas MPC 2, LQR 1 and LQR 2 are used for all three errors.

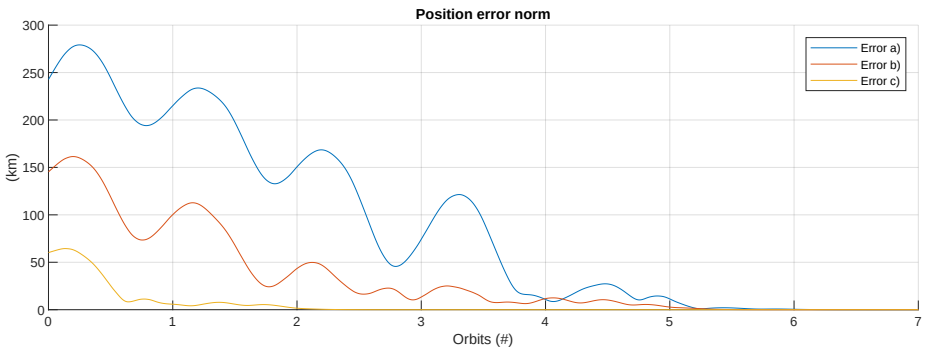

Figure 6.17: Magnitude of the position error for initial errors defined in Table 6.2.

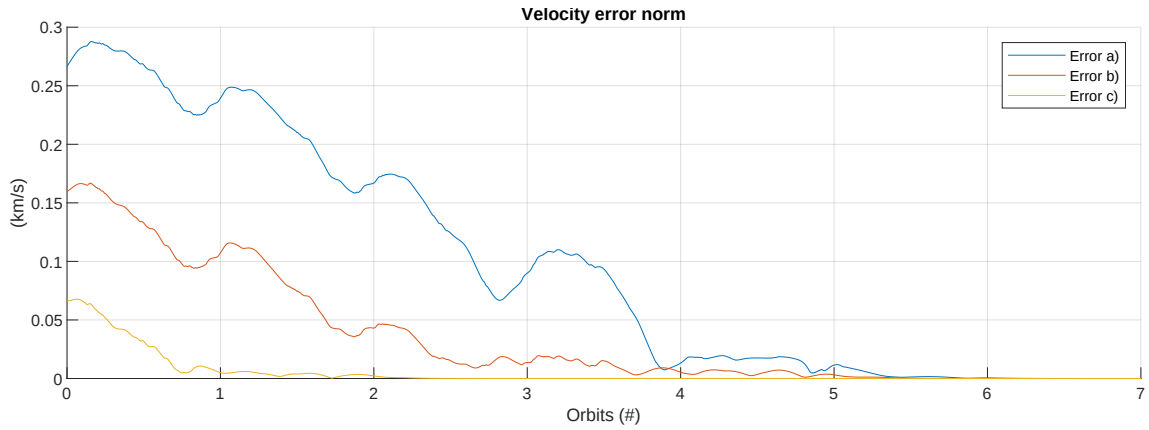

Figure 6.18: Magnitude of the velocity error for initial errors defined in Table 6.2.

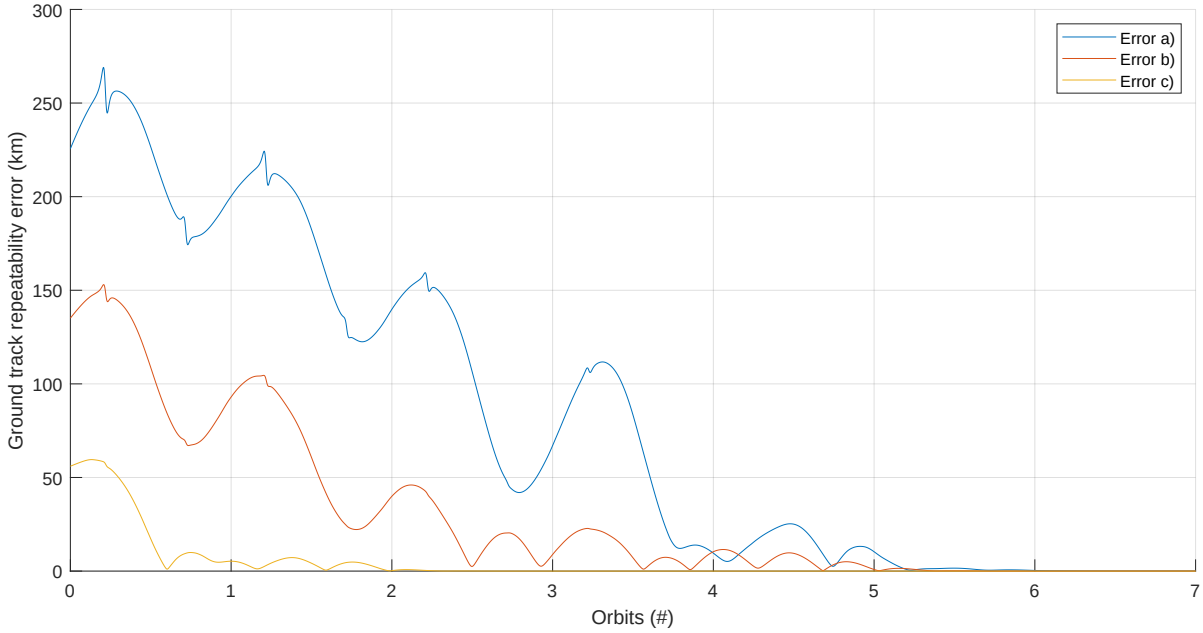

Figure 6.19: Ground track repeatability error for initial errors defined in Table 6.2.

Further analysis is performed for the worst case scenario injection error (error a)). Figure 6.20 illustrates the variation of the Keplerian elements error between the real and the reference satellite, for this initial error. The correction of all Keplerian elements is successfully achieved after approximately 6 complete orbits (34081 s), at the transition from LQR 1 to LQR 2. However, due to the large errors to be corrected, this process is very demanding with significant oscillations in all Keplerian elements, mainly in the semi-major axis and the eccentricity vector. Figure 6.21 illustrates the variation of the Cartesian components of the real satellite, for initial error a), expressed in a Local Orbit reference frame, centered at the reference satellite center of mass. Notice that the highest error is reflected in the o_1 component due to the argument of latitude error that causes an advance in the orbit of the real satellite.

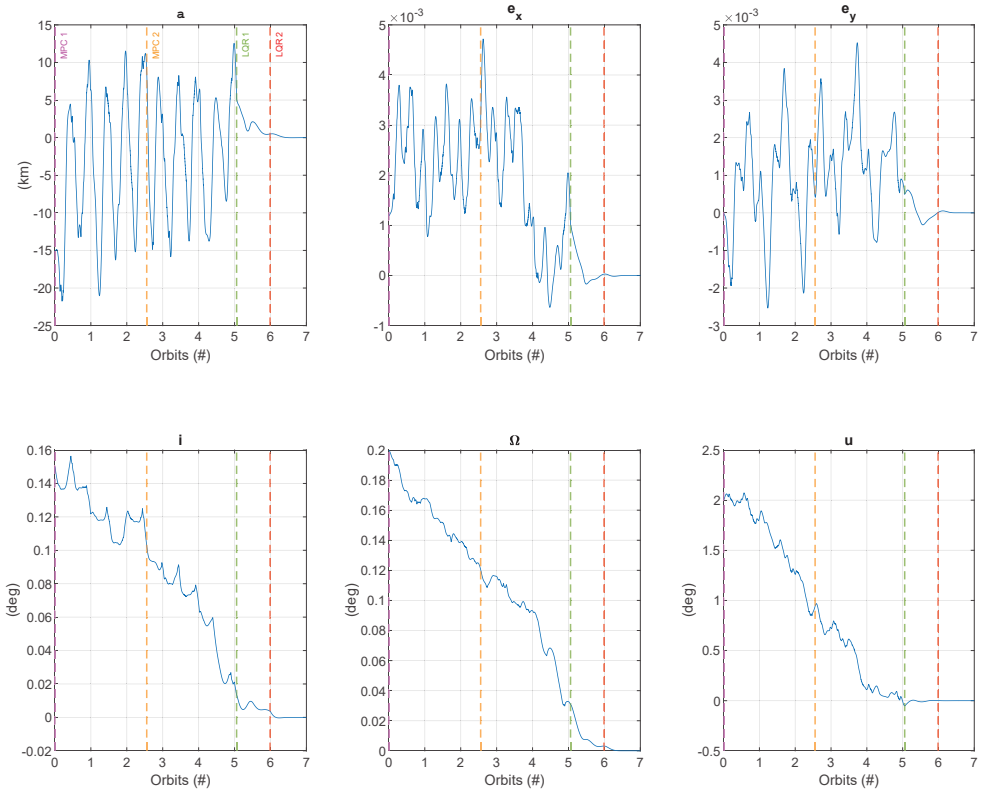

Figure 6.20: Keplerian elements error between the real and the reference satellite for error a). The transition between the controller in use is marked with a dashed line.

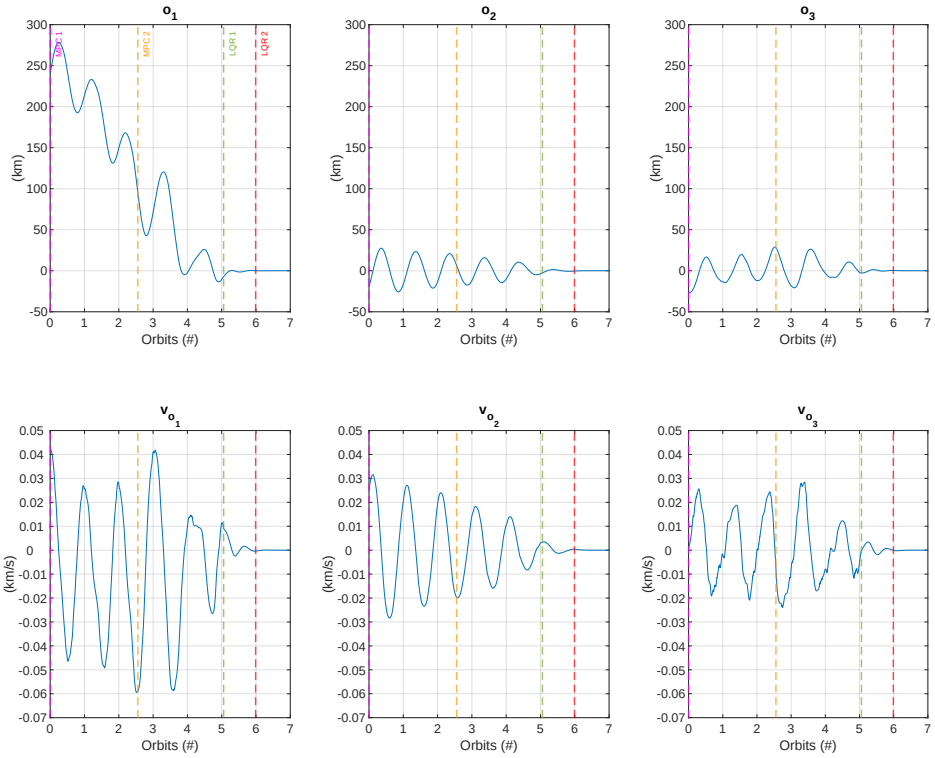

Figure 6.21: Variation of the Cartesian components of the real satellite expressed in a Local Orbit reference frame, centered at the reference satellite center of mass, for error a).

Figure 6.22 illustrates the control acceleration expressed in a Local Orbit reference frame, centered at the real satellite center of mass. The control acceleration magnitude has a maximum limit due to the actuators saturation. This is evident during the period of actuation of the MPC controllers given that the orbital error is larger and a higher control acceleration is needed to correct this error. Notice the variations in direction of each component of the control acceleration to correct the evolution of the system.

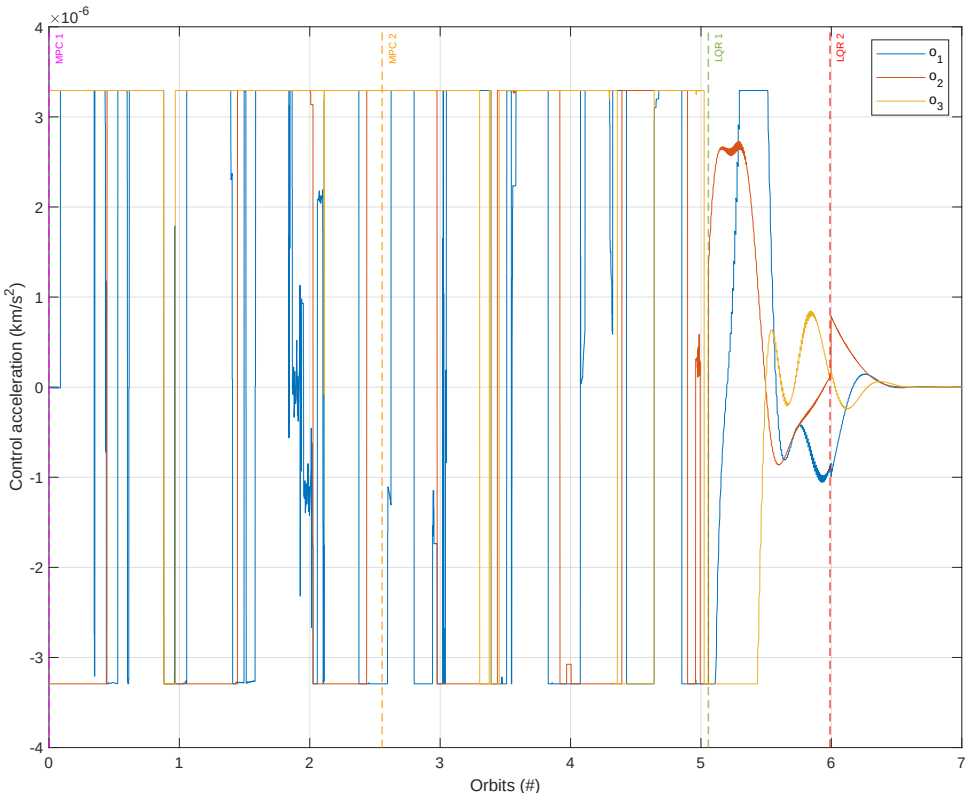

Figure 6.22: Control acceleration expressed in a Local Orbit reference frame, centered at the real satellite center of mass, for error a).

After reaching the steady-state, LQR 2 is used to correct the effect of the orbital perturbations and maintain the error between the real and the reference satellite close to zero. Figure 6.23 shows the evolution of the ground track repeatability error during 3 complete orbits of the reference satellite (approximately 17070 s), after the seventh complete orbit of this satellite. This error oscillates due to the effect of perturbative accelerations having its maximum around 7.5×10^{-6} km. This value completely satisfies the requirement to maintain the ground track repeatability error below 0.5 km.

To understand the behaviour of the ground track repeatability error, it is important to analyse the evolution of the Keplerian elements error between the real and the reference satellite at the steady-state, illustrated in Fig. 6.24. Notice that a oscillates about -7×10^{-5} km, approximately, and u about -4×10^{-8} deg, approximately. This happens due to the effect of atmospheric drag that produces a force in the opposite direction of the real satellite motion and causes a decrease in a and an orbital delay, reflected on the negative value of u. The effect of the solar radiation pressure and third-body gravitational attraction is evident on the oscillations of i about -3.35×10^{-8} deg, approximately, and Ω about -1.3×10^{-8} deg, approximately.

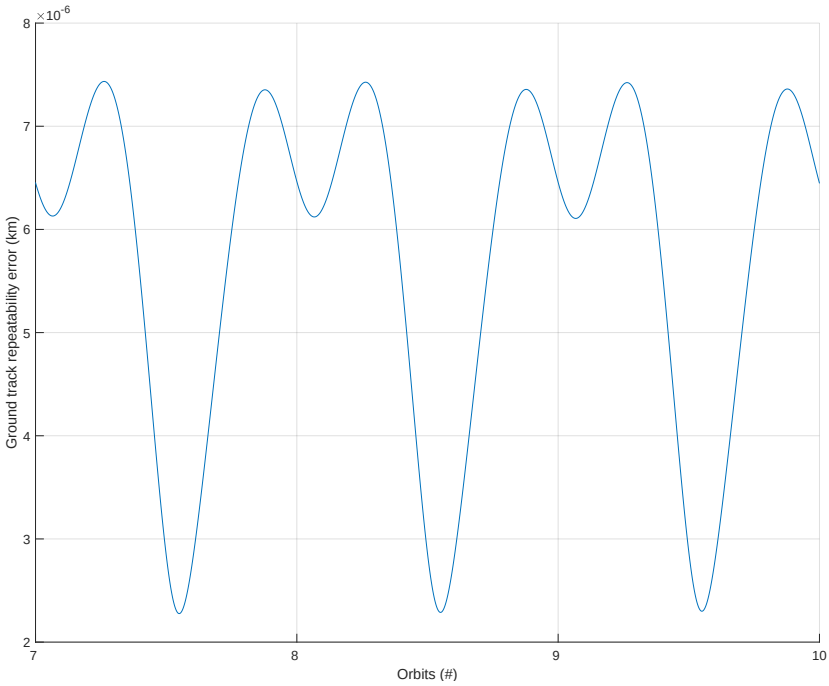

Figure 6.23: Ground track repeatability error between the real and the reference satellite after reaching the steady-state.

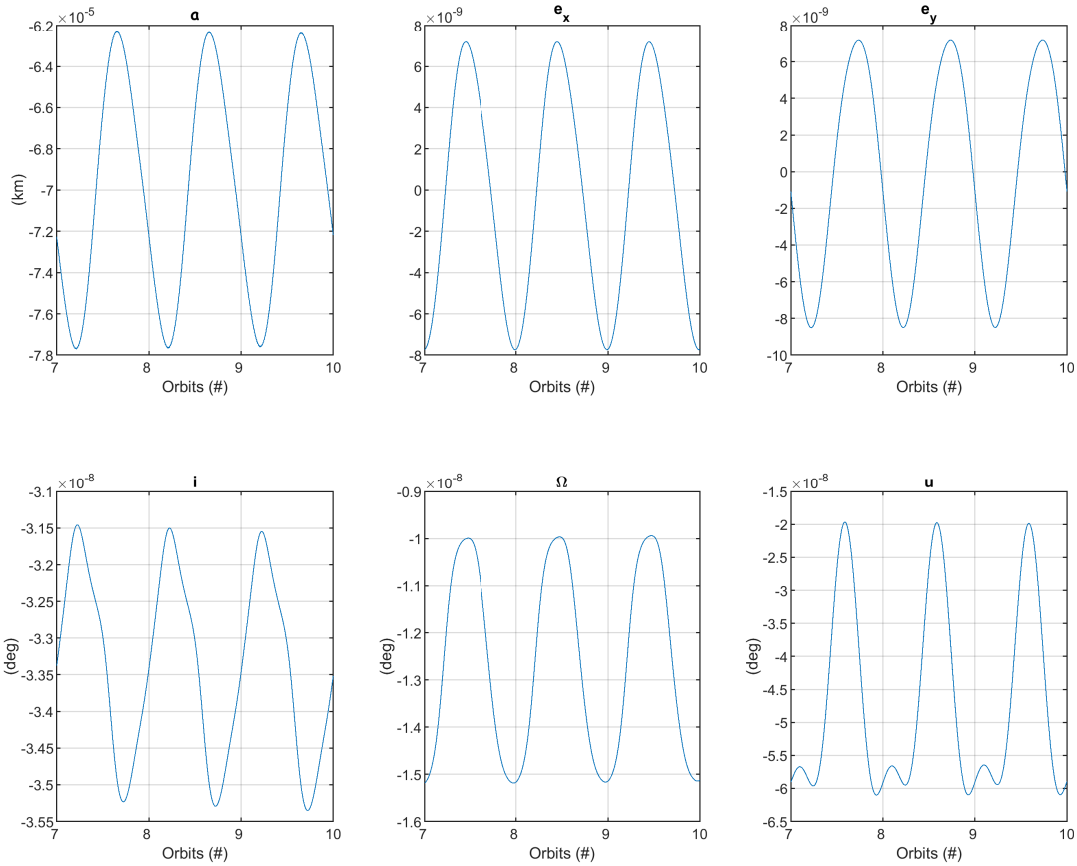

Figure 6.24: Keplerian elements error between the real and the reference satellite after reaching the steady-state.

The variation of the Cartesian components of the real satellite expressed in a Local Orbit reference frame, centered at the reference satellite center of mass, allows for another perspective on the effect of the atmospheric drag, as illustrated in Fig. 6.25. The component o_3 oscillates about -1.75×10^{-5} km since the real satellite is orbiting at a lower altitude, and the component o_1 oscillates about -0.5×10^{-5} km, given that the real satellite has an orbital delay relative to the reference satellite, which correlates with the analysis of the Keplerian elements.

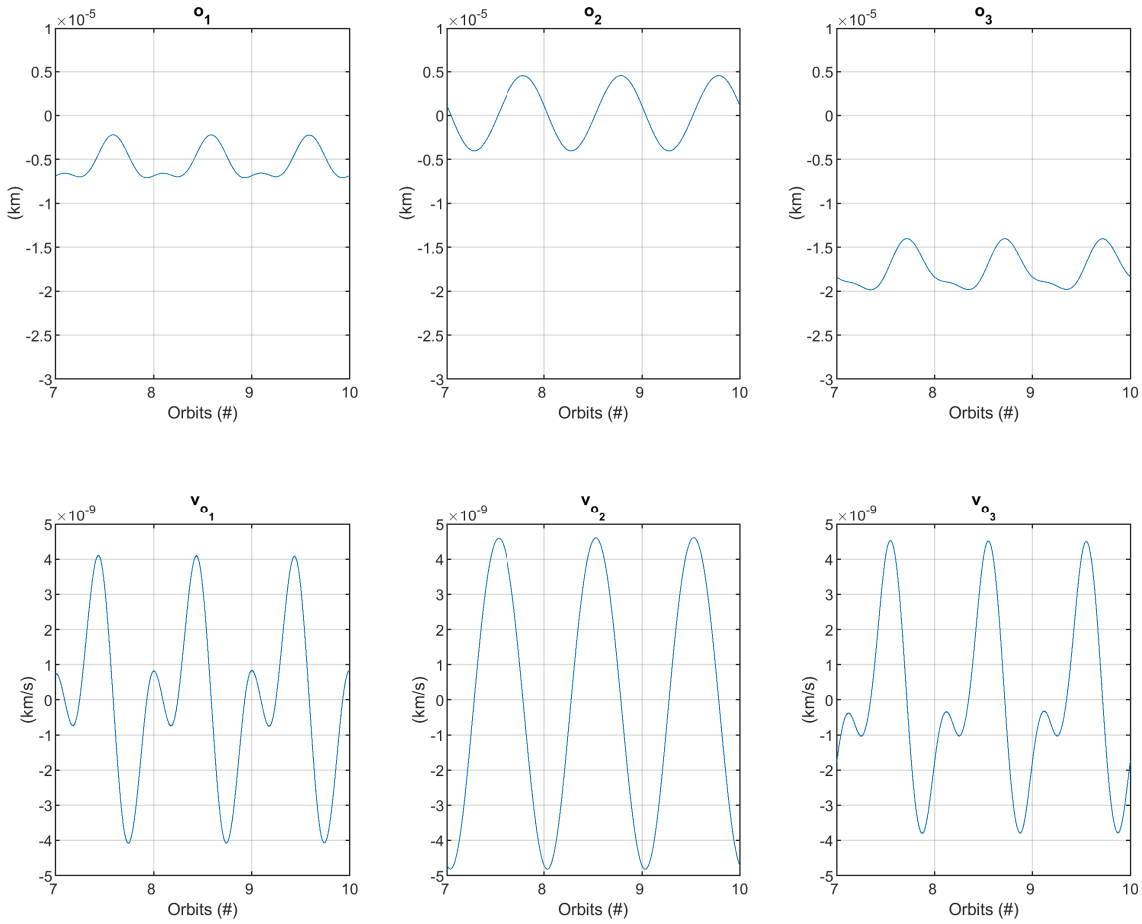

Figure 6.25: Variation of the Cartesian components of the real satellite expressed in a Local Orbit reference frame, centered at the reference satellite center of mass, after reaching the steady-state.

Figure 6.26 illustrates the control acceleration expressed in a Local Orbit reference frame, centered at the real satellite center of mass, after reaching the steady-state. From this figure, it is possible to conclude that most of the actuation is done in the o_1 and o_3 directions to counteract the effect of the atmospheric drag. The actuation in the o_2 direction is mainly directed to correct the error caused in i and Ω, due to the effect of the other orbital perturbations.

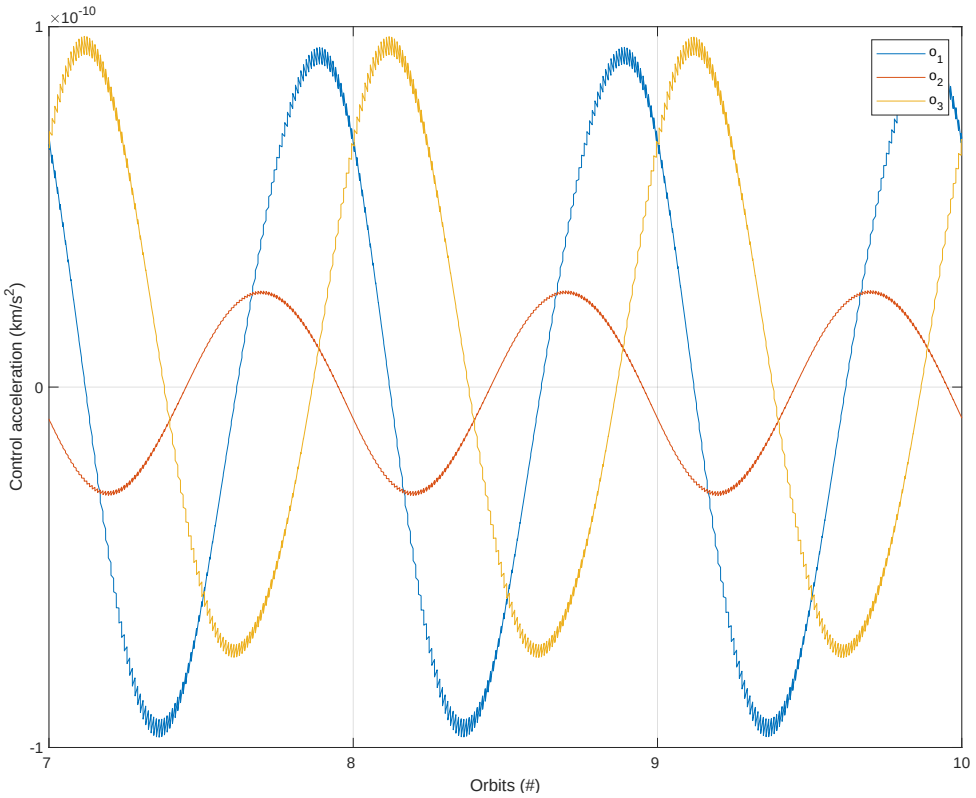

Figure 6.26: Control acceleration expressed in a Local Orbit reference frame, centered at the real satellite center of mass, after reaching the steady-state.

6.5 Combined injection error with realistic sensors and actuators

Error a), defined in Section 6.4, is used to assess the controller performance in a simulation with realistic actuators and sensors, as defined in Table 5.3 and in Table 5.4.

Figure 6.27 illustrates the evolution of the ground track repeatability error for a simulation with a duration equal to 7 complete orbits of the reference satellite (approximately 39830 s). In this case, the transition from MPC 2 to LQR 1 occurs at a position error magnitude of 8 km. As presented, the objective to reduce the value of this error to less than 0.5 km is still achieved after approximately 5.5 complete orbits (30985 s), despite using realistic sensors and actuators that induce noise in the system. Actually, the effect of the non-idealities of the sensors and the actuators is not visible when compared to the magnitude of the initial error, as illustrated in Fig. 6.27.

The effect of using realistic sensors and actuators becomes visible after reaching the steady-state. Figure 6.28 shows the evolution of the ground track repeatability error during 3 complete orbits of the reference satellite (approximately 17070 s), after the seventh complete orbit of this satellite. At this point, the system is in steady-state and LQR 2 is controlling the system. This controller is designed to handle the noise generated by the sensors and actuators and, at the same time, to counteract the effect of orbital perturbations. Notice that the ground track repeatability error presents values up to 0.21 km, high above the values illustrated in Fig. 6.23. However, these error values are well within the requirements for this parameter (0.5 km), which confirms the effectiveness of the control strategy.

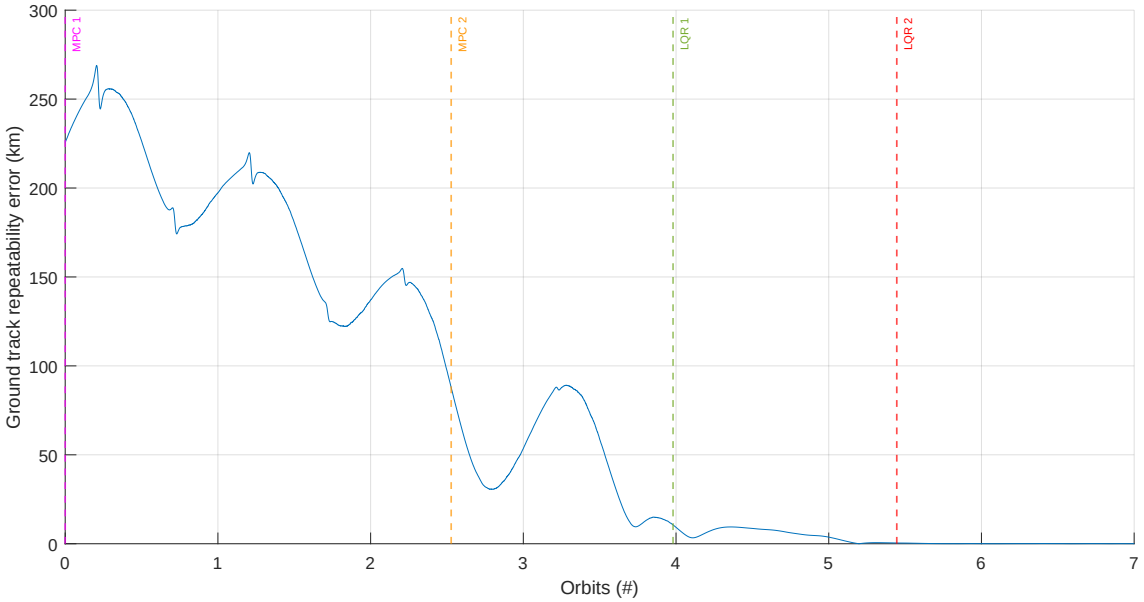

Figure 6.27: Ground track repeatability error between the real and the reference satellite for initial error a), using realistic sensors and actuators.

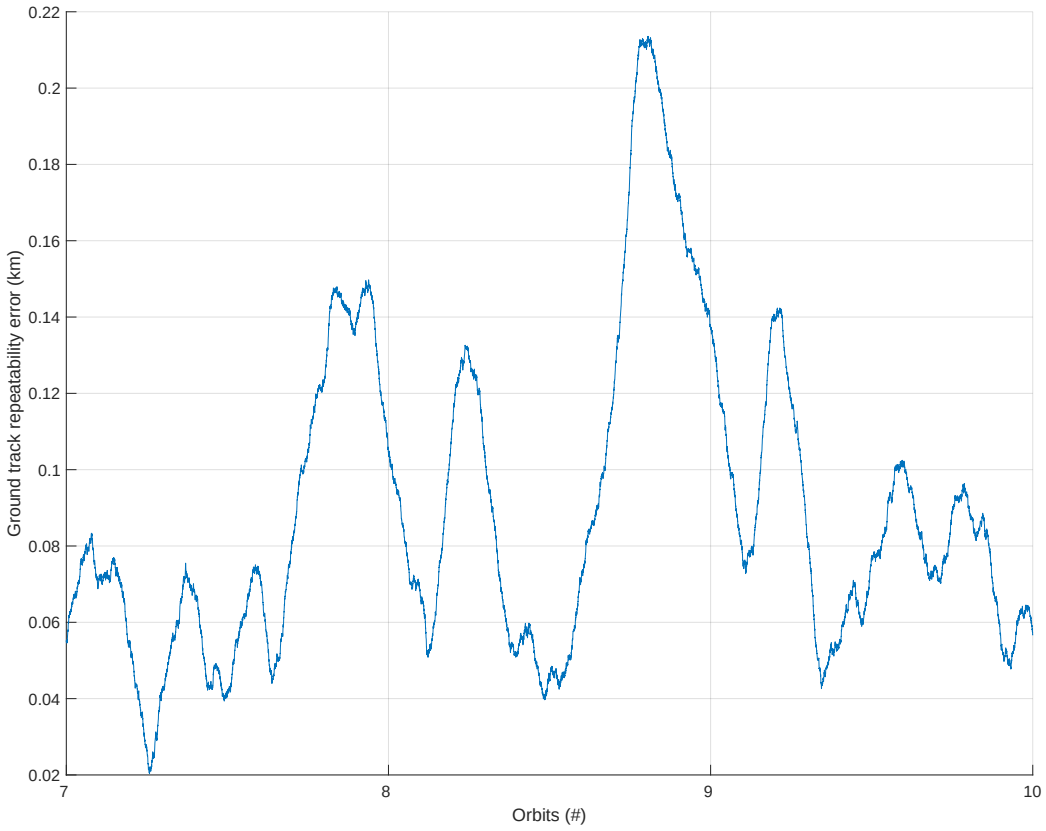

Figure 6.28: Ground track repeatability error between the real and the reference satellite after reaching the steady-state, using realistic sensors and actuators.

A different perspective on the effect of using realist sensors and actuators is provided by Fig. 6.29 and by Fig. 6.30. Figure 6.29 illustrates the control acceleration expressed in a Local Orbit reference frame, centered at the real satellite center of mass, after reaching the steady-state. The noise induced by the realistic actuators, which preclude the maintenance of the orbital error at zero, is visible in this figure. Figure 6.30 illustrates the evolution of the Keplerian elements error between the real and the reference satellite after reaching the steady-state. Notice the noise effect in all Keplerian elements, causing significant variations in the values of these parameters.

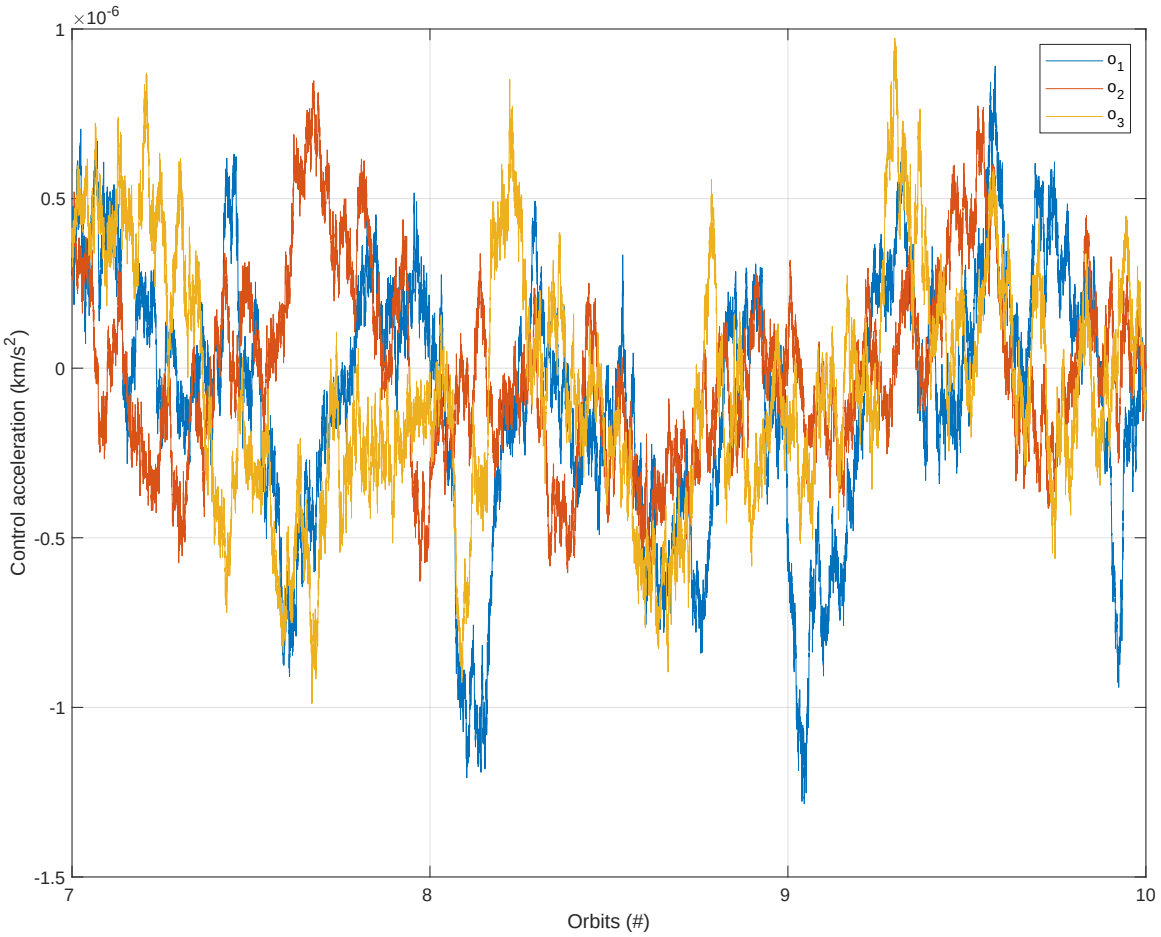

Figure 6.29: Control acceleration expressed in a Local Orbit reference frame, centered at the real satellite center of mass, after reaching the steady-state, using realistic sensors and actuators.

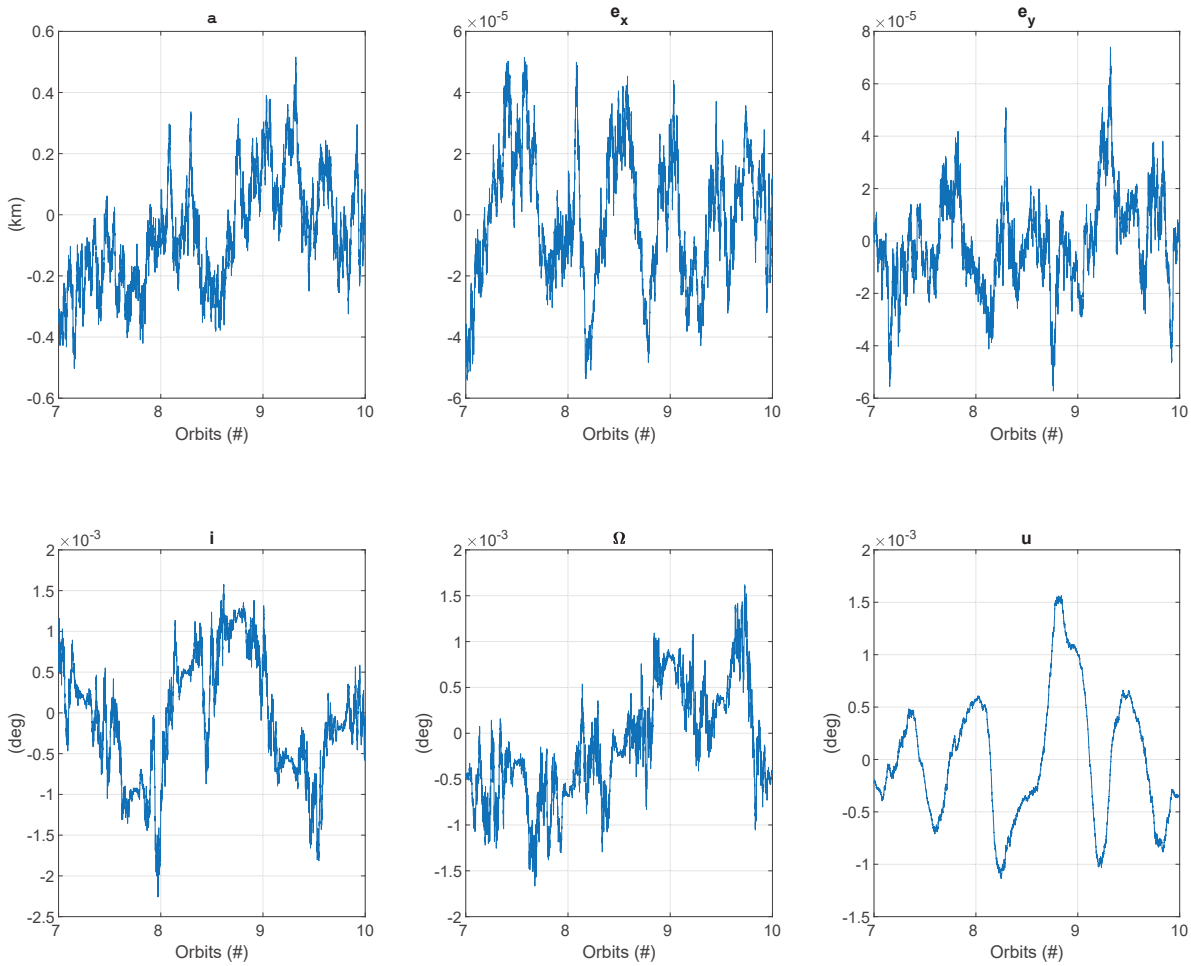

Figure 6.30: Keplerian elements error between the real and the reference satellite after reaching the steady-state, using realistic sensors and actuators.

Chapter 7

Conclusions

7.1 Achievements

The objective of this work was the design of an autonomous orbit control algorithm, capable of correcting large orbit injection errors and counteract the effect of environmental perturbations to maintain the desired orbit parameters. The TerraSAR-X mission was used as the reference mission and provided the spacecraft characteristics and orbit requirements to evaluate the algorithm performance in correcting different types of orbital errors and maintaining the satellite in the required orbit location. The performance analysis was done using an accurate orbital simulator developed in MATLAB and the results obtained were presented and discussed in Chapter 6.

Although good results were obtained, the controller tuning was proven difficult and its performance dependent on the initial orbital state, due to the complexity of the system and the relatively small prediction window used in the design of the MPC. The computational effort required to compute the control actions limited the dimension of the prediction window, decreasing the control performance. A strategy to simplify the system model can be explored to reduce the computational effort and, in that way, enable the increase of the prediction horizon.

The obtained MPC results in correcting large initial orbit errors were interesting to overcome the limitations of the LQR related to the linearization process. Nonetheless, LQR is a computationally efficient strategy and presented good results for orbit maintenance routines, when the orbit error is close to zero.

The AOC strategy developed in this thesis demonstrated effective results in correcting orbit injection errors in different Keplerian elements. Initial errors in the semi-major axis and inclination were successfully driven to zero without significant variations on the control acceleration direction (expressed in a Local Orbit reference frame, centered at the satellite center of mass). However, the correction of the initial error in the argument of latitude led to an oscillatory response of the system before reaching the steady-state. Note that, the argument of latitude error defined is very large when compared to the error simulated for other Keplerian elements. Therefore, the response time for the correction of the argument of latitude error is not near to the prediction time of the MPC. It is expected that a larger prediction horizon will significantly improve the results obtained, at the cost of increased computational effort. Nevertheless, the

TerraSAR-X mission requirements were fulfilled even in the worst-case scenario, when a combination of maximum injection error in all Keplerian elements was used as the initial state.

The AOC algorithm demonstrated good performance for orbit maintenance activities. The controller was capable of counteracting the effect of orbital perturbations, maintaining the orbital error close to zero. Environmental perturbations cause the error to oscillate about a negligible value when compared to the mission requirements. The use of realistic sensors and actuators, which introduced noise in the system, did not impact the initial convergence of the proposed algorithm. In the steady-state, the impact of these non-idealities is more evident and caused the ground track repeatability error to present values up to 0.21 km, widely above the values for a situation of ideal sensors and actuators, but still well within the requirements defined for the TerraSAR-X mission.

The use of electric propulsion was proven effective for orbit maintenance activities. However, the correction of large initial errors required the use of multiple thrusters to achieve sufficient actuation force to correct the orbit of TerraSAR-X, due to its relatively high mass. Future improvements on the electric propulsion topic might overcome this problem with the development of more powerful thrusters. Though, this strategy is interesting and should be explored to control the orbit of smaller satellites. The control strategy based on electric propulsion developed in this thesis should be tested against a chemical propulsion solution to assess the efficiency in terms of propellant and energy costs.

To summarise, the AOC strategy was proven to be effective in achieving the objectives proposed for this thesis. Nevertheless, further improvements to the proposed strategy can increase the performance of the controller and refine the results.

7.2 Future Work

Further steps can be taken in order to improve the control strategy. The design of an MPC to correct orbit errors close to zero and perform orbit maintenance activities should be explored and its performance compared with the LQR solution, considering energy and propellant costs. The optimisation of the MPC controller should also be pursued in order to reduce the computational effort required, allowing the use of a larger prediction time window.

Future work should also compare the use of chemical propulsion with the one proposed in this thesis, which is based on electrical propulsion, taking into consideration convergence time and propellant and energy costs. Moreover, a solution that combines the two types of propulsion mentioned should not be discarded. For instance, an autonomous control strategy that uses chemical thrusters to correct large injection errors and electric thrusters for orbit maintenance activities could be an interesting solution to overcome the lack of thrust provided by the electric systems. This strategy still offers the efficiency associated with electric propulsion systems when working close to the desired orbit, at the cost of the additional complexity of having two propulsion systems on-board.

The performance of the developed AOC algorithm should also be evaluated for a smaller satellite. In this case, the required thrust to perform orbit correction activities is smaller and, therefore, the electric propulsion is best suited.

Bibliography

[1] Union of Concerned Scientists. UCS satellite database. https://ucsusa.org/resources/satellite-database?_ga=2.206523283.1848871521.1598077135-464362950.15980771353, visited on October 10, 2021.

[2] Geospatial World. How many satellites are orbiting the earth in 2021? https://www.geospatialworld.net/blogs/how-many-satellites-are-orbiting-the-earth-in-2021/, visited on October 10, 2021.

[3] World Economic Forum. Who owns our orbit: Just how many satellites are there in space? https://www.weforum.org/agenda/2020/10/visualizing-easrth-satellites-sapce-spacex, visited on October 10, 2021.

[4] François Bonaventure, Vincent Baudry, Thibault Sandre, and Anne-Hélène Gicquel. Autonomous orbit control for routine station-keeping on a LEO mission. *Journal of Guidance, Control, and Dynamics 34(6):1683-1693*, 2011.

[5] Sergio De Florio and Simone D'Amico. Optimal autonomous orbit control of remote sensing spacecraft. *19th AAS/AIAA Space Flight Mechanics Meeting, Savannah, Georgia*, 2014.

[6] M.M. Tavakoli and Nima Assadian. Model predictive orbit control of a low earth orbit satellite using Gauss's variational equations. *Proceedings of the Institution of Mechanical Engineers, Part G, Journal of Aerospace Engineering 228(13):2385-2398*, 2014.

[7] De Florio S, D'Amico S, and Radice G. Flight results of the precise autonomous orbit keeping experiment on the PRISMA mission. *Journal of Spacecraft and Rockets 50(3):662-674*, 2012.

[8] H. J. Rim, B. Schutz, C. Webb, P. Demarest, and A. Herman. Orbit maintenance and characteristics for a SAR satellite. *AIAA/AAS Astrodynamics Specialist Conference and Exhibit, Colorado*, 1998.

[9] Mirko Leomanni, Andrea Garulli, and Antonio Giannitrapani. An adaptive groundtrack maintenance scheme for spacecraft with electric propulsion. *Acta Astronautica*, 2019.

[10] Simone D'Amico, C. Arbinger, and M. Eineder. Precise ground-in-the-loop orbit control for low earth observation satellites. *18th ISSFD Meeting, Munich, Germany*, 2004.

[11] F. Landis Markley and John L. Crassidis. *Fundamentals of Spacecraft Attitude Determination and Control*. Springer, 2014.

[12] D. Pessanha Neves. Control algorithm for ISTsat-1. Master's thesis, Instituto Superior Técnico, 2019.

[13] Aboelmagd Noureldin, Tashfeed B. Karamat, and Jacques Georgy. *Fundamentals of Inertial Navigation, Satellite-based Positioning and their Integration*. Springer, 2013.

[14] Karel F. Wakker. *Fundamentals of Astrodynamics*. Faculty of Aerospace Engineering, Delft University of Technology, 2015.

[15] Oliver Montenbruck and Simone D'Amico. Proximity operations of formation-flying spacecraft using an eccentricity/inclination vector separation. *Journal of Guidance Control and Dynamics, Vol. 29, No. 3*, 2006.

[16] Louis Breger and Jonathan P. How. GVE-based dynamics and control for formation flying spacecraft. *MIT Department of Aeronautics and Astronautics*, 2004.

[17] K. C. Howell, D. J. Grebow, and Z. P. Olikara. Design using Gauss' perturbing equations with applications to lunar south pole coverage. *Journal of Guidance, Control, and Dynamics 32(6):1884-1897*, 2009.

[18] Wolfram MathWorld website. Eccentric anomaly. `https://mathworld.wolfram.com/EccentricAnomaly.html`, visited on June 6, 2021.

[19] Michel Capderou. *Handbook of Satellite Orbits - From Kepler to GPS*. Springer, 2014.

[20] Craig A. Kluever. *Space Flight Dynamics*. Wiley, 2018.

[21] J. M. Picone, A. E. Hedin, and D. P. Drob. NRLMSISE-00 empirical model of the atmosphere: Statistical comparisons and scientific issues. *Journal of Geophysical Research Atmospheres 107(A12)*, 2002.

[22] C. J. Brookes. Evaluation of odd zonal harmonics in the earth's gravitational potential. *The Royal Society, Proceedings: Mathematical and Physical Sciences Vol. 446, No. 1926*, 1994.

[23] Frank L. Lewis, Draguna L. Vrabie, and Vassilis L. Syrmos. *Optimal Control*. John Wiley and Sons, Inc., 2012.

[24] Zhilei Zheng, Zhongjing Wang, Jianshi Zhao, and Hang Zheng. Constrained dictive control algorithm for cascaded irrigation canals. *Journal of Irrigation and Drainage Engineering 145(6):04019009*, 2019.

[25] MathWorks. Optimization problem. `https://www.mathworks.com/ug/optimization-problem.html#bujxvp9-9`, visited on July 12, 2021.

[26] MathWorks. Nonlinear MPC. `https://www.mathworks.com/help/mpc/ug/nonlinear-mpc.html`, visited on August 22, 2021.

[27] James R. Wertz, David F. Everett, and Jeffrey J. Puschell. *Space Mission Engineering: The New SMAD*. Microcosm Press, 2011.

[28] Saika Aida and Michael Kirschner. Accuracy assessment of SGP4 orbit information conversion into osculating elements. *6th European Conference on Space Debris, Darmstadt, Germany*, 2013.

[29] Christopher F. Wildt. Accuracy in orbital propagation: A comparison of predictive software models. Master's thesis, Calhoun Naval Postgraduate School, 2017.

[30] S. D'Amico, E. Gill, and O. Montenbruck. Relative orbit control design for the PRISMA formation flying mission. *AIAA Guidance, Navigation and Control Conference, Colorado*, 2006.

[31] Herbert J. Kramer. TacSat-2 / roadrunner. https://directory.eoportal.org/web/eoportal/satellite-missions/t/tacsat-2, visited on March 25, 2021.

[32] DLR. *Phoenix Spaceborne GPS Receiver*, 2007.

[33] ISISpace Group. *GNSS Active Patch Antenna*, 2020.

[34] NewSpace Systems. *GPS receiver - NGPS-03-422*, 2020.

[35] MOOG, Inc. *Navigation Single Board Receiver NavSBR*, 2015.

[36] RUAG Space. *PODRIX GNSS Receiver*, 2019.

[37] Oliver Montenbruck, Miquel Garcia-Fernandez, and Jacob Williams. Performance comparison of semicodeless GPS receivers for LEO satellites. *GPS Solutions 10*, 2006.

[38] S. Marcuccio, F. Ceccanti, and M. Andrenucci. Control strategies for orbit maintenance of LEO small satellites with feep. *Spacecraft Propulsion, Third International Conference, Cannes, France*, 2000.

[39] ESA website. What is electric propulsion? https://esa.int/EnablingSupport/SpaceEngineering-Technology/WhatisElectricpropulsion, visited on April 21, 2021.

[40] MOOG, Inc. *Cold Gas Thrusters*, 2021.

[41] ArianeGroup website. 1N hydrazine thruster. https://www.space-propulsion.com/spacecraft-propulsion/hydrazine-thrusters/1n-hydrazine-thruster.html, visited on June 11, 2021.

[42] MOOG, Inc. *Monopropellant Thrusters*, 2018.

[43] Dawn Aerospace website. https://www.dawnaerospace.com/position, visited on June 11, 2021.

[44] MOOG, Inc. *Bi-propellant Thrusters*, 2019.

[45] BUSEK, Co. Inc. *BIT-3 RF Ion Thruster*, 2019.

[46] ArianeGroup website. Radio frequency ion propulsion. https://space-propulsion.com/spacecraft-propulsion/propulsion-systems/electric-propulsion/index.html, visited on June 12, 2021.

[47] BUSEK, Co. Inc. *BUSEK Micro Resistojet*, 2013.

[48] BUSEK, Co. Inc. *BUSEK BHT-200 Hall Effect Thruster*, 2019.

[49] BUSEK, Co. Inc. *BUSEK BHT-8000 Hall Effect Thruster*, 2019.

[50] S. Buckreuss, W. Pitz, and R. Werninghaus. Status of the TerraSAR-X mission. *IEEE International Geoscience and Remote Sensing Symposium, Brussels, Belgium*, 2007.

[51] Yuanbo Wu, Mingjun Pu, and Donghong Wang. Multi-objective optimization method for repeat ground-track orbit design considering the orbit injection error. *Journal of Aerospace Technology and Management 10*, 2018.

[52] UC Davis Math. Linearizing equations about rest points: The speed of sound, the speed of light, and the difference between them. 2020.

[53] E. Okyere, A. Bousbaine, G.T. Poyi, A.K. Joseph, and J.M. Andrade. LQR control design for quad-rotor helicopters. *The Journal of Engineering 2019(17)*, 2019.

[54] MathWorks. Choose sample time and horizons. `https://www.mathworks.com/help/mpc/ug/choosing-sample-time-and-horizons.html`, visited on September 2, 2021.

[55] MathWorks. nlmpcmove. `https://www.mathworks.com/help/mpc/ref/nlmpc.nlmpcmove.html#mw_f32e081b-0763-4b1a-8df4-2b4b325ecbc3`, visited on September 4, 2021.

[56] Earl Lawrence, Richard Linares, David Higdon, and Josef Koller. Modeling satellite drag coefficients with response surfaces. *Advances in Space Research Vol.54 (8)*, 2014.

[57] J. B. Silva Neto, Antonio Prado, Diogo Merguizo Sanchez, and Jorge Kennety Silva Formiga. On the use of a variable coefficient of reflectivity associated with an augmented area-to-mass ratio to de-orbit CubeSats. *Journal of Physics Conference Series 911(1):012009*, 2017.

[58] David Eagle. *Mean Local Time of the Ascending Node*. MATLAB Central File Exchange, Retrieved on September 15, 2021.

[59] Neil Wallace, Peter Jameson, Christopher Saunders, Michael Fehringer, Clive Edwards, and Rune Floberghagen. The GOCE ion propulsion assembly – lessons learnt from the first 22 months of flight operations. *32nd International Electric Propulsion Conference, Wiesbaden, Germany*, 2011.

[60] Arianespace Inc. *Vega C User's Manual, Issue 0 Revision 0*, 2018.